Increased Formability and the Effects of the Tool/Sheet Interaction in Electromagnetic Forming of Aluminum Alloy Sheet

by

José Miguel Segundo Imbert Boyd

A thesis
presented to the University of Waterloo
in fulfilment of the
thesis requirement for the degree of
Master of Applied Science
in
Mechanical Engineering

Waterloo, Ontario, Canada, 2005

© José Miguel Segundo Imbert Boyd 2005

I hereby declare that I am the sole author of this thesis. This is a true copy of the thesis, including any required final revisions, as accepted by my examiners.

I understand that my thesis may be made electronically available to the public.

ABSTRACT

This thesis presents the results of experimental and numerical work carried out to determine if electromagnetic forming (EMF) increases the formability of aluminum alloy sheet and, if so, to determine the mechanisms that play a role in the increased formability. To this end, free form (open cavity) and conical in-die samples were produced to isolate high strain rate constitutive and inertial effects from the effects of the interaction between the die and the sheet. Aluminum alloys AA5754 and AA6111 in the form of 1mm sheet were chosen since they are currently used in automotive production and are candidates for lightweight body panels.

The experiments showed significant increases in formability in the conical die samples in areas where significant contact with the tool occurred, with no significant increase recorded for the free-formed samples. This indicates that the tool/sheet interaction is playing the dominant role in the increase in formability observed. Metallographic and fractographic analysis performed on the samples showed evidence of microvoid damage suppression, which may be a contributing factor to the increase in formability.

Numerical modeling was undertaken to analyse the details of the forming operation and to determine the mechanisms behind the increased formability. The numerical calculations were performed with an explicit dynamic finite element structural code, using an analytical electromagnetic pressure distribution. Microvoid damage evolution was predicted using a microvoid damage subroutine based on the Gurson-Tvergaard-Needleman constitutive model. From the models it has been determined that the free forming process is essentially a plane-stress process. In contrast, the tool/sheet interaction produced in cone forming makes the process unique. When the sheet makes contact with the tool, it is subject to forces generated due to the impact, and very rapid bending and straightening. These combine to produce complex non-linear stress and strain histories, which render the process non-plane stress and thus make it significantly different from conventional sheet forming processes. Another characteristic of the process is that the majority of the plastic deformation occurs at impact, leading to strain rates on the order of 10,000 s^{-1}. It is concluded that the rapid impact, bending and straightening that results from the tool/sheet interaction is the main cause of the increased formability observed in EM forming.

ACKNOWLEDGEMENTS

First I would like to thank my supervisor, Professor Michael Worswick for allowing me the opportunity to become part of his research group. His guidance, knowledge, ideas and support made for a great and valuable learning experience. This work was made possible by the cooperation of the Ford Motor Company, and I would like to acknowledge the support given by Dr. Andrew Sherman. I would especially like to thank Dr. Sergey Golovashchenko for sharing his vast knowledge and expertise in EM forming. Also, I gratefully acknowledge the support of the Ontario Research and Development Challenge fund.

Many thanks to Dr. Sooky Winkler, for her tutelage and help in metallography and damage analysis. Thanks to Kevin Moule for keeping all the computers running. Thanks to John Boldt, Brian Whitfield and Yuquan Ding. Completing this work also required navigating the university's red tape maze, which I could not have done without the administrative staff of the Mechanical Engineering Department, especially Sue Spaetzel, Laurie Young and Marlene Dolson, whom I thank for their help and good cheer.

Spending over two years dedicated exclusively to mechanical engineering graduate work would result in irreparable psychological damage. Thus the occasional distraction and the support of my friends were always appreciated. Thanks to Blake who put me in contact with Prof. Worswick and for the years of friendship. To Dino thanks for helping no questions asked and for all the alternatively employed time. Chris I thank his friendship and the occasional use of his office. Thanks Raf for sharing sources, knowledge and the FK9 file. To the rest of the office gang especially the old timers Oleg, Rassin, Alex (G and B), Sooky, Zengtao, Josh and Javad. Many thanks to the "external" Waterloo crew Nestor, Rosie and Duane. I can't thank enough my old friends in DR, Ottawa and Toronto, they know why.

I owe a lot to my family and I will never know a proper way to thank them. To my aunts, uncles and cousins spread all over Canada and the DR, thank you. Thanks to my brother, who has gone from childhood nemesis to indispensable friend. A mi abuela Batty, gracias por querernos tanto. Finally to my mother and my father thank you for letting me be myself, fail and succeed, and for always being there.

To my mother and father

TABLE OF CONTENTS

CHAPTER 1

INTRODUCTION……....1

1.1 THE EM PROCESS……2

1.2 EM FORMING OF AXI-SYMMETRIC WORKPIECES……...3

1.3 EM FORMING OF SHEET METAL……..4

1.4 FACTORS THAT INFLUENCE FORMABILITY IN HIGH VELOCITY FORMING ……..6

1.4.1 Constitutive Effects - High Strain Rate Behaviour of Aluminum Alloys……6

1.4.2 Inertial Effects……13

1.4.3 Tool/Sheet Interaction Effects……14

1.5 EFFECTS OF EM FORMING ON PROPERTIES OF ALUMINUM……..16

1.6 FAILURE OF DUCTILE MATERIALS……...18

1.6.1 The Role of Microvoid Damage……19

1.6.2 Damage Suppression by Hydrostatic Pressure……...21

1.7 SIMPLIFIED ANALYSIS OF EM FORMING PROCESSES……..22

1.7.1 Magnetic Pressure Distribution……..25

1.7.2 Magnetic Pressure Distribution on a Sheet Caused by an Idealized Spiral Coil……26

1.7.3 Skin Effect……..27

1.8 NUMERICAL SIMULATION OF EMF……...28

1.9 PRESENT WORK……..29

CHAPTER 2

EXPERIMENTAL METHODS AND PROCEDURES……31

2.1 MATERIALS AND SAMPLE PREPARATION……..31

2.1.1 Material Properties……31

2.1.2 Sample Preparation……32

2.2 APPARATUS……33

2.2.1 Power Supply and Experimental Set-Up……33

2.2.2 Tooling……...35

2.2.3 Experimental Procedure……38

2.3 STRAIN MEASUREMENTS……38
2.4 METALLOGRAPHY……39
2.5 FRACTOGRAPHY……40
CHAPTER 3
NUMERICAL MODEL……41
3.1 MESH……41
3.1.1 Blank Mesh……42
3.1.2 Tool Meshes……43
3.2 LOADS AND BOUNDARY CONDITIONS……44
3.3 MATERIAL MODEL……47
CHAPTER 4
EXPERIMENTAL RESULTS……50
4.1 DEFORMED GEOMETRY……51
4.2 FORMABILITY DATA……59
4.3 MICROSCOPY AND DAMAGE RESULTS……75
4.4 FRACTOGRAPHY……84
4.5 SUMMARY……90
CHAPTER 5
NUMERICAL RESULTS……92
5.1 DEFORMATION HISTORIES……92
5.2 VALIDATION OF MODEL……94
5.2.1 Predicted Sample Heights……96
5.2.2 Predicted Versus Experimental Strains……96
5.2.3 Predicted Maximum Pressures……104
5.2.4 Summary of Model Validation……107
5.3 PARAMETRIC STUDY FOR DAMAGE PARAMETERS……108
5.4 TOOL/SHEET INTERACTION EFFECTS……113
5.4.1 Stress and Strain Histories……115
5.4.2 Effect of Impact on Damage Evolution and Hydrostatic Stress……122
5.5 STRAIN PATH EFFECTS……128
5.6 EFFECT OF CONE ANGLE ON DAMAGE DISTRIBUTION……131

5.7 FRACTURE AND BUCKLING PREDICTIONS……...132
CHAPTER 6
DISCUSSION……...135
CHAPTER 7
CONCLUSIONS AND FUTURE WORK……...138
7.1 CONCLUSIONS……...138
7.2 FUTURE WORK……139

LIST OF FIGURES

Figure 1: Schematic of EM forming 2
Figure 2: Tube contraction and expansion EM operations [6]. 3
Figure 3: Two types of EMF a) flat sheet forming and b) feature sharpening. 4
Figure 4: Types of flat or pancake coils with approximate resulting pressure distributions along indicated sections [6,]. 5
Figure 5: Formability data for electrohydraulically formed AA 6061 [14,15]. 5
Figure 6: Formability data for AA6111-T4 EM formed into a V-die (taken from Golovashchenko *et al.* [16]). Forming limit curve (FLC) provided by ALCAN International []. 6
Figure 7: Strain rate dependence of several aluminum alloys compiled by Lindholm *et al.* [23]. 7
Figure 8: Mechanical properties versus strain rate for aluminum alloys 5454-O and 6061-T651 [23]. 8
Figure 9: Flow stress at 5% strain vs strain rate for several alloys and temperatures from Tanaka and Nojima [25]. Stress units are kilogram, kg, divided by millimetre, mm, squared. A and B refer to alloys with different heat treatments, giving Vickers hardness of 98 and 34 respectively. 9
Figure 10: Stress versus strain data for AA 5056-O and 5056-ECAE [26]. 10
Figure 11: Flow stress and elongation data for several aluminum alloys presented by Higashi *et al.* [27]. The present author added the horizontal dashed line to illustrate how the strain rate sensitivity can be both negative and positive for the same material at different strain rates. 11
Figure 12: Flow stress at 5% strain for AA 6082-T6 at room temperature, 375 and 515 °C [28]. 12
Figure 13: Ragazzoni *et al.'s* proposed unloading front [31]. In stage 1 the material is deforming plastically throughout. Elastic waves emanate from the defect in stage 2, which eventually lead to localization of the plastic deformation in the defect in stage 3. 13
Figure 14: Inertial force neck retardation effect as proposed by Balanethiram and Daehn [14]. 14

Figure 15: Schematic diagram illustrating the inertial ironing effect [15]. 15
Figure 16: Change in flow stress ($\Delta\sigma$) versus number of magnetic pulses. Figures are, from top to bottom for pure aluminum, copper and brass [38]. 17
Figure 17: Fracture modes for ductile materials: a) plastic collapse, b) ductile failure and c) shear fracture [39]. 18
Figure 18: Simplified view of the two types of void formation; a) de-cohesion of the particle matrix interface and b) particle cracking. 19
Figure 19: The most favourable stress state for the growth of voids is a positive hydrostatic stress state, *i.e.* $\sigma_{11}=\sigma_{22}=\sigma_{33} >>0$ 20
Figure 20: Aluminum-Copper alloy deformed at a) ambient pressure and b) and c) with a hydrostatic pressure of 300 MPa. Images b and c show views of the neck of the same specimen at 90º from each other [49]. 21
Figure 21: a) schematic illustration of an EM forming system, b) simplified EM forming circuit. 22
Figure 22: Current versus time profile given by the solution equation 1-2 [6]. 24
Figure 23: Current versus time profile for an actual EM forming coil [6]. 24
Figure 24: Normalized predicted (solid line) and measured (dashed line and points) magnetic intensity (and pressure) distribution versus radial position for a spiral coil, as reported by Al-Hassani [12]. Ho and Po are the maximum magnetic intensity and pressure, respectively. 27
Figure 25: True stress-strain curves for AA5754 and AA6111 [20]. 32
Figure 26: Schematic of experimental apparatus. 33
Figure 27: Experimental EMF apparatus; a) view of the complete apparatus including coil assembly, power supply and control panel and b) a close up of the coil assembly. 34
Figure 28: Apparatus ready for forming including security cap and bar. 35
Figure 29: Drawing of the free forming die. 36
Figure 30: Conical cavity die design for the 40 and 45º cone angles. Nominal cavity diameter 120.0mm, actual diameter (d*), with fillet, is shown in the table. 37
Figure 31: Tooling configuration for the 34º die. Exact height and d* dimensions are shown in Figure 30. 37
Figure 32: The grid measurement system. 39

Figure 33: Exploded view of a cone (40º) model mesh. The blank elements have been omitted for clarity. 41
Figure 34: Top view of the blank mesh. 42
Figure 35: A close up view of the blank at the centre. 43
Figure 36: The die meshes used in this study meshed using four-node quadrilateral elements. 44
Figure 37: Radial pressure distribution used for blank loading. Taken from Al-Hassani [12]. 45
Figure 38: Pressure versus time profile used to load the nodes in the model. 46
Figure 39: Clamping load application 47
Figure 40: Typical AA5754 free-formed sample (5.8 kV)..... 52
. 52
Figure 41: Free-formed AA5754 failed sample (7.7 kV). 53
Figure 42: Blanking failure mode of free-formed AA 5754 sheet (8.0 kV)..... 53
Figure 43: AA5754 sheet formed with 34º cone (8.0 kV)..... 54
Figure 44: AA5754 sheet formed with the 40º cone (8.0 kV)..... 54
Figure 45: AA5754 sheet formed with the 45º cone (9.0 kV)..... 55
Figure 46: Buckling near the vacuum hole in a AA5754 sheet sample formed into the 45º cone..... 55
Figure 47: AA6111 free-formed sample (5.2 kV)..... 56
Figure 48: AA6111 sheet formed with the 34º cone (7.0 kV)..... 56
Figure 49: AA6111 sheet formed with the 40º cone (9.0 kV)..... 57
Figure 50: AA6111 sheet formed with the 45º cone (10.0 kV)..... 58
Figure 51: Typical tip fracture for AA6111 sheet formed with the 45º cone..... 58
Figure 52: Formability data for free-formed AA5754 samples. The curve is a conventional FLD curve for the material [20]. Open symbols indicated measurements in the neck area. 60
Figure 53: Formability data for free-formed AA6111 samples. The curve is a conventional FLD curve for the material [20]. Open symbols indicated measurements in the neck area. 61
Figure 54: Formability data for the AA5754 conical samples. Open symbols indicated measurements in the neck area. 63

Figure 55: Formability data for the AA6111 conical samples. 64
Figure 56: Photograph illustrating what will be called from now on the radial and hoop directions of the samples. 65
Figure 57: Radial distribution of strains for AA5754 safe (5.8 kV) free-formed samples. Solid symbols represent major strain and open ones represent minor strain. Sample 1=■, sample 2=▲ and Sample 3=♦ 66
Figure 58: Radial distribution of strains for AA5754 necked (6.5 kV) free-formed samples. Solid symbols represent major strain and open ones represent minor strain. Sample 1=■, sample 2=▲ and Sample 3=♦ 67
Figure 59: Radial distribution of strains for AA6111 safe free-formed samples (5.0 kV). Solid symbols represent major strain and open ones represent minor strain. Sample 1=■, sample 2=▲ and Sample 3=♦ 68
Figure 60: Radial distribution of strains for AA 6111failed (5.2 kV) free-formed samples. Solid symbols represent major strain and open ones represent minor strain. Sample 1=■, sample 2=▲ and Sample 3=♦ 69
Figure 61: Radial distribution of strains for AA5754 34º samples. Solid symbols represent major strain and open ones represent minor strain. Sample 1=■, sample 2=▲ and Sample 3=♦. 70
Figure 62: Radial distribution of strains for AA5754 40º samples. Solid symbols represent major strain and open ones represent minor strain. Sample 1=■, sample 2=▲ and Sample 3=♦. 71
Figure 63: Radial distribution of strains for AA5754 45º samples. Solid symbols represent major strain and open ones represent minor strain. Sample 1=■, sample 2=▲ and Sample 3=♦. 72
Figure 64: Radial distribution of strains for AA6111 34º samples. Solid symbols represent major strain and open ones represent minor strain. Sample 1=■, sample 2=▲ and Sample 3=♦. 73
Figure 65: Radial distribution of strains for AA6111 40º samples. Solid symbols represent major strain and open ones represent minor strain. Sample 1=■, sample 2=▲ and Sample 3=♦. 74

Figure 66: Radial distribution of strains for AA6111 45º samples. Measurements could only be taken from the step to the base due to the condition of the sample. Solid symbols represent major strain and open ones represent minor strain. Sample 1=■, sample 2=▲ and Sample 3=♦. 75
Figure 67: Measured porosity area fraction (%) for an AA5754 40º cone..... 77
Figure 68: Measured porosity area fraction (%) for the neck of an AA5754 45º cone. 77
. 78
Figure 69: Measured porosity area fraction (%) for an AA6111 40º cone..... 79
Figure 70: Measured porosity area fraction (%) near the two types of fracture of AA6111 45º cones. 79
Figure 71: Typical damage and second phase particles present in AA5754 samples. Image in this figure comes from the step area of a 34º cone. 80
Figure 72: Typical damage and second phase particles present in AA6111 samples. Image in this figure comes from the step area of a 40º cone specimed. 80
Figure 73: Comparison between a) AA5754 and b) an AA6111 free-formed necks. 81
Figure 74: Comparison of AA5754 and AA6111 steps produced by the different conical dies. 82
Figure 75: Micrographs of a) the neck and b) the tip fracture of an AA5754 specimen formed into a 45º cone. 83
Figure 76: Micrographs of a) the "saw tooth" and b) the tip fractures present in AA6111 samples formed with the 45º die..... 84
Figure 77: Fracture surface an AA5754 quasi-static tensile sample. 85
Figure 78: Fracture surface an AA6111 quasi-static tensile sample. 85
Figure 79: Fracture surface of a free-formed AA5754. 86
Figure 80: Fracture surface of a tip fracture in an AA5754 sample formed into a 45º cone.... 87
Figure 81: Fracture surface of a free-formed AA6111 sample. 88
Figure 82: Fracture surface for the "saw tooth" fracture in an AA6111 formed into a 45º cone. 89
Figure 83: Fracture surface for the tip fracture of AA6111 formed into a 45º cone. 90
Figure 84: Deformation history of free-formed AA5754 sheet. The image is the result of revolving the $1/8^{th}$ model for illustration purposes. A 45º section has been removed to

observe the inside of the sample. Contours are of void volume fraction (not adjusted for nucleated second phase particle fraction). 93
Figure 85: Deformation history for an AA5754 sample formed into a 40º cone. The image is the result of revolving the 1/8th model for illustration purposes. A 45º section has been removed to observe the inside of the sample. Tooling is not shown for clarity. Contours are of void volume fraction (not adjusted for nucleated second phase particle fraction).. 94
Figure 86: Free form deformation history for a free-formed sample predicted by the model compared with published experimental and coupled numerical histories. Current model is shown in A. Experimental data from Takatsu *et al.* [19] is shown in B. Results from fully coupled models are shown in C taken from Fenton and Daehn [37] and D taken from Risch *et al.* [58]. 95
Figure 87: Predicted and measured radial and hoop strains versus radial position for an AA5754 free form sample. Measured radial = ■, measured hoop =▲, predicted radial = ——— and predicted hoop = ——— 97
Figure 88: Predicted and measured radial and hoop strains versus radial position for an AA5754 necked free form sample. Measured radial = ■, measured hoop =▲, predicted radial = ——— and predicted hoop = ——— 98
Figure 89: Predicted and measured radial and hoop strains versus radial position for an AA5754 34º conical sample. Measured radial = ■, measured hoop =▲, predicted radial = ——— and predicted hoop = ——— 98
Figure 90: Predicted and measured radial and hoop strains versus radial position for an AA5754 40º conical sample. Measured radial = ■, measured hoop =▲, predicted radial = ——— and predicted hoop = ——— 99
Figure 91: Predicted and measured radial and hoop strains versus radial position for an AA5754 45º conical sample. Measured radial = ■, measured hoop =▲, predicted radial = ——— and predicted hoop = ——— 99
Figure 92: Predicted and measured radial and hoop strains versus radial position for an AA6111 free-formed sample. Measured radial = ■, measured hoop =▲, predicted radial = ——— and predicted hoop = ——— 100

Figure 93: Predicted and measured radial and hoop strains versus radial position for an AA6111 necked free-formed sample. Measured radial = ■, measured hoop =▲, predicted radial = ——— and predicted hoop = ——— 101
Figure 94: Predicted and measured radial and hoop strains versus radial position for an AA6111 34º conical sample. Measured radial = ■, measured hoop =▲, predicted radial = ——— and predicted hoop = ——— 102
Figure 95: Predicted and measured radial and hoop strains versus radial position for an AA6111 40º conical sample. Measured radial = ■, measured hoop =▲, predicted radial = ——— and predicted hoop = ——— 102
Figure 96: Predicted and measured radial and hoop strains versus radial position for an AA6111 free-formed sample with flow curve scaled by 200%. Measured radial = ■, measured hoop =▲, predicted radial = ——— and predicted hoop = ——— 104
Figure 97: Peak pressure versus time profiles used for the AA5754 models. Note that the safe free form data is nearly identical to the 34º cone data..... 105
Figure 98: Peak pressure versus time profiles used for the AA6111 models..... 106
Figure 99: Experimental charge voltages and numerical peak pressures for AA5754 and AA6111. 107
Figure 100: Effect of nucleation strain on predicted void volume fraction. Solid squares represent measured data for AA5754 40º cone samples. Data is presented from tip (0) to base (1). 109
Figure 101: Effect on void volume fraction predictions of changing void volume fraction required for coalescence. 110
Figure 102: Predicted void volume fraction compared with experimental results for 50% nucleation strain and 1.6% void volume fraction required for coalescence to begin..... 111
Figure 103: Effect of nucleation strain on predicted void volume fraction. Solid squares represent measured data for AA6111 40º cones..... 112
Figure 104: Effect on predicted void volume fraction of changing void volume fraction required for coalescence. Experimental data included for comparison..... 112
Figure 105: Effective plastic strain distribution as the sheet is formed into the die. Contours are effective plastic strain. 114

Figure 106: Detailed view of the tool/sheet interaction in the area of the tip of the sample. Contours are of void volume fraction (not adjusted for nucleated second phase fraction). 115
Figure 107: Typical stress and strain histories for a region below the neck of a free-formed sample. Note that final shape is reached at 0.31 ms. 116
Figure 108: Stress and strain history for the necked region of a free-formed sample. Note that final shape is reached at 0.31 ms. 117
Figure 109: Stress and strain histories for the step area of a 40º conical sample. Time of impact is 0.19 ms. Scales vary for the stresses and strains but are constant for each type. 119
Figure 110: Stress and strain histories for an area below the tip of a 40º conical sample. Time of impact is 0.28 ms. Scales vary for the stresses and strains but are constant for each type. 120
Figure 111: Normalized hydrostatic stress and void volume percentage histories for a region below the neck of a free-formed sample. Hydrostatic stress is normalized by the yield stress of 97.7 MPa. 123
Figure 112: Normalized hydrostatic stress and void volume percentage histories for the neck of a free-formed sample. Hydrostatic stress is normalized by the yield stress of 97.7 MPa. 124
Figure 113: Normalized hydrostatic stress and void volume percentage histories for the step area. Hydrostatic stress is normalized by the yield stress of 97.7 MPa. Time of impact is 0.19 ms. 126
Figure 114: Normalized hydrostatic stress and void volume percentage histories for the area below the tip. Hydrostatic stress is normalized by the yield stress of 97.7 MPa. Time of impact is 0.28 ms. 127
Figure 115: Strain path history for elements of a) the step and b) the tip area of a free-formed sample. 129
Figure 116: Strain path history for elements of the step and tip area of a 40º conical sample. 130
Figure 117: Effect of cone angle on damage distribution for AA5754. 131
Figure 118: Effect of cone angle on damage distribution for AA6111. 132

Figure 119: Failed AA5754 45º sample compared to numerical prediction. A nucleation strain of 10% was required to produce failure. 133

LIST OF TABLES

Table 1: Normal compositions (wt%) of AA5754 [20] and AA6111 [] aluminum alloys..... 31
Table 2: Summary of damage parameters used in the constitutive model in the present study. 49
Table 3: AA 5754 samples used for the experimental program. S=strain measurements, H= height measurements and M=microscopy (optical and SEM). 50
Table 4: AA 6111 samples used for the experimental program. S=strain measurements, H= height measurements and M=microscopy (optical and SEM). 51
Table 5: Summary of forming voltage and average sample heights. Fractured samples were those with complete separation of the tip. * Only two samples measured. 52
Table 6: Summary of damage data for the AA5754 samples. S= safe, N= necked. * see Figure 68. + Due to the abraded condition of the grids of the sample where the damage was measured, strain values are an average of the strains in the region for the other two samples. 76
Table 7: Summary of damage data for the AA6111 samples. S= safe, N= necked. * see Figure 70. + Average value for region of fracture. 78
Table 8: Comparison between numerically predicted and experimental sample heights. For details on individual sample heights and forming conditions see Table 3 and Table 4. * Average of highest point in the samples..... 96

CHAPTER 1

INTRODUCTION

Recent interest in lightweight vehicle production has led to increased use and consideration of aluminum as an automotive manufacturing material. Aluminum alloys offer the possibility of reduced car weight; which in turn leads to reduced fuel consumption. Unfortunately, aluminum has poor forming characteristics [1,2,3], which when combined with its relatively high cost, put it at a disadvantage relative to steel, the traditional material of choice in the automotive industry.

One way of overcoming aluminum's poor formability has been through the use of high velocity forming techniques like explosive forming, electrohydraulic forming and electromagnetic forming (EMF). The current research will focus on EMF, since it has the greatest potential of these high rate processes for application in the automotive industry.

EM forming has been in use since the early 1960's [4,5]; however, it has remained a niche manufacturing technique used mainly for the production of axi-symmetric parts from tube and for mechanical joining, with limited commercial sheet forming application. EM forming of sheet has been studied and used since the introduction of EM forming, without ever gaining wide spread acceptance. Recently, interest in EMF has been renewed to explore the possibility of applying this process to automotive production, due to the reported increases in formability that it affords.

A review of the basic principles and available literature on EMF, with an emphasis on aluminum alloys, will be presented in the remainder of the chapter. Sections on high strain rate forming of aluminum and ductile fracture are included to familiarize the reader with these topics, but they are not intended as comprehensive reviews of the subjects.

1.1 The EM Process

A schematic of the EM process is shown in Figure 1. The process begins by charging a capacitor bank to the voltage required for the specific operation and then discharging it through a coil. A current pulse flows through the coil, generating a transient magnetic field. This magnetic field in turn generates a time varying current in the conductive workpiece, which generates a magnetic field that opposes the field of the coil. The magnetic fields repel one and other, generating a body force on the workpiece that propels it away from the coil. This force is typically referred to as the "magnetic pressure" [4,5,6,7,8].

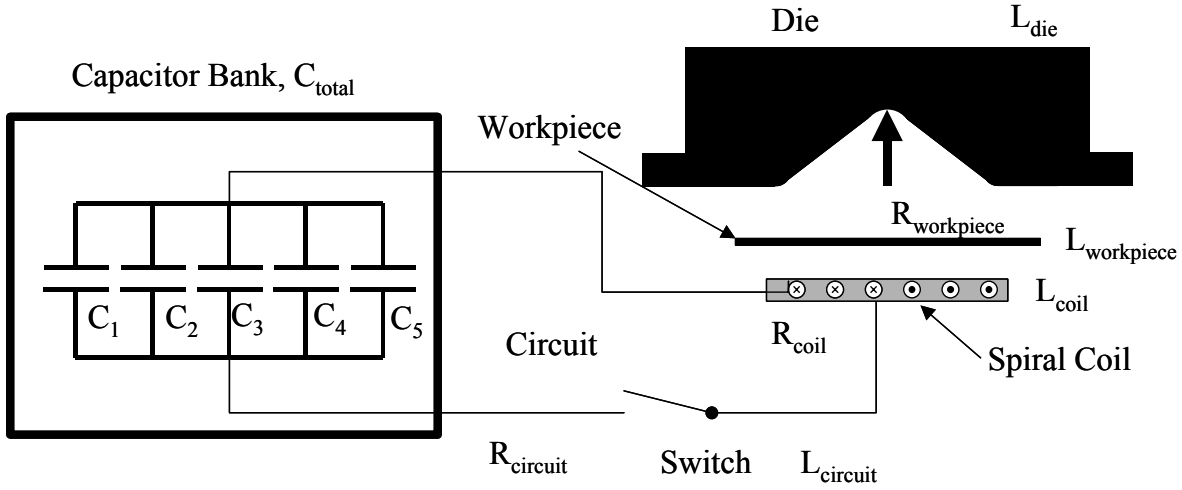

Figure 1: Schematic of EM forming .

Figure 1 also shows the properties of the basic EMF circuit. The capacitor bank has a capacitance, C_{total}, and the coil, workpiece and each circuit element has a resistance, R, and inductance, L, associated with it. A more detailed analysis of the process will be presented in the Section 1.7.

Electromagnetic forming can be divided in two major categories, forming of axi-symmetric workpieces (*e.g.* tube) and forming of sheet. The latter is the focus of this work; however, a brief review of the former is presented to introduce some basic concepts and to offer a historical perspective.

1.2 EM Forming of Axi-Symmetric Workpieces

EM forming of axisymmetric workpieces has been a niche manufacturing technique for many years. This process uses solenoidal coils, which produce a nearly uniform magnetic field. The uniform magnetic field, combined with an axi-symmetric workpiece, makes the process relatively easy to design and implement. Tubes can either be expanded or contracted, depending on the location of the coil, as shown on Figure 2.

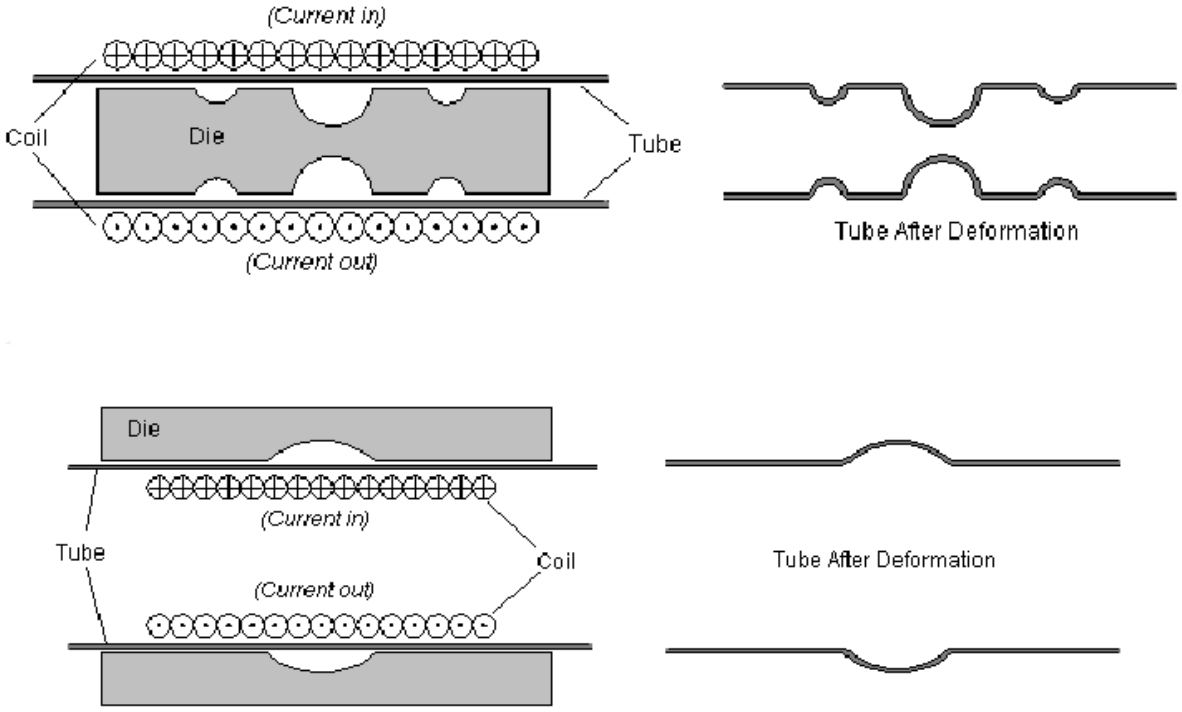

Figure 2: Tube contraction and expansion EM operations [6].

Several authors have carried out theoretical analysis of EM free expansion of tube, which typically simplify the process as an RLC (resistor-inductor-capacitor) circuit [7,9,10]. The tubes are generally considered to be of fixed length and long enough to neglect any edge effects on the EM field. Section 1.7 includes a more detailed explanation of this approach.

Tube contraction uses the same principles to contract a tube [11]. It is mainly used in industry to produce mechanical joints (crimping), since uniform pressure distributions given by the coils produce better crimp joints than those made with mechanical presses [8].

1.3 EM Forming OF Sheet Metal

EMF of sheet has never gained as much acceptance as tube forming in commercial applications. EMF can be used to form parts from flat sheet, or to sharpen features of pre-formed workpieces (Figure 3) in so-called hybrid operations. Sheet metal workpieces do not deform uniformly, as do tubes, leading to additional complications in the design and implementation of the process.

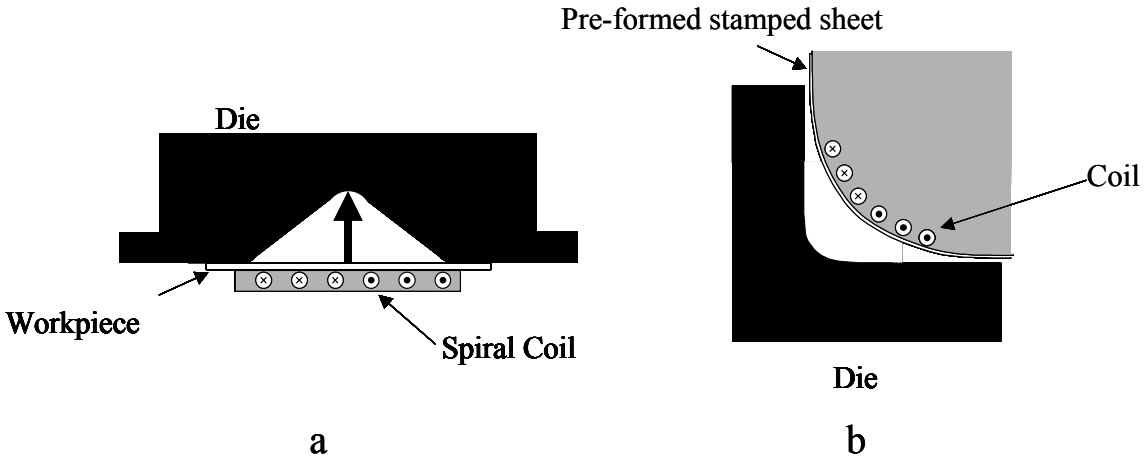

Figure 3: Two types of EMF a) flat sheet forming and b) feature sharpening.

Flat or "pancake" coils are generally needed to form parts from sheet metal (Figure 4). These coils do not produce uniform magnetic fields and often have dead spots where the magnetic field, and thus the induced pressure are zero [6]. The magnetic field is cancelled out for adjacent coils for which current flow occurs in opposing directions.

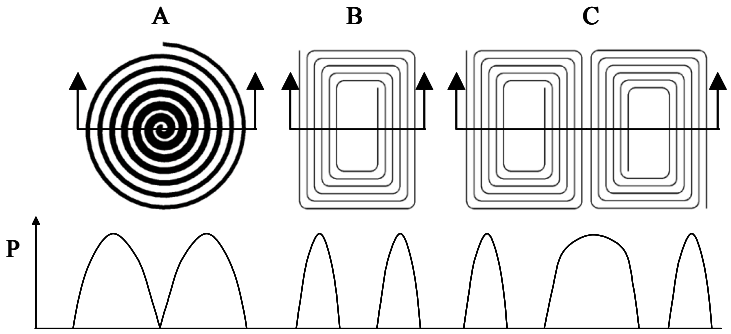

Figure 4: Types of flat or pancake coils with approximate resulting pressure distributions along indicated sections [6, 12].

EMF of sheet has become the focus of numerous investigations due to the possibility of increasing the formability of aluminum alloys. Several studies have indicated that the formability of aluminum increases when it is formed using high-speed processes like EMF or electrohydraulic forming [13,14,15,16,17,18,19]. Work on electrohydraulically formed AA6061 has shown significant increases in formability (Figure 5). AA6111 EM formed in to a V-shaped die has also shown increases in formability, as shown in Figure 6. Both figures show a significant increase in formability when compared to the conventional forming limit diagram (FLD).

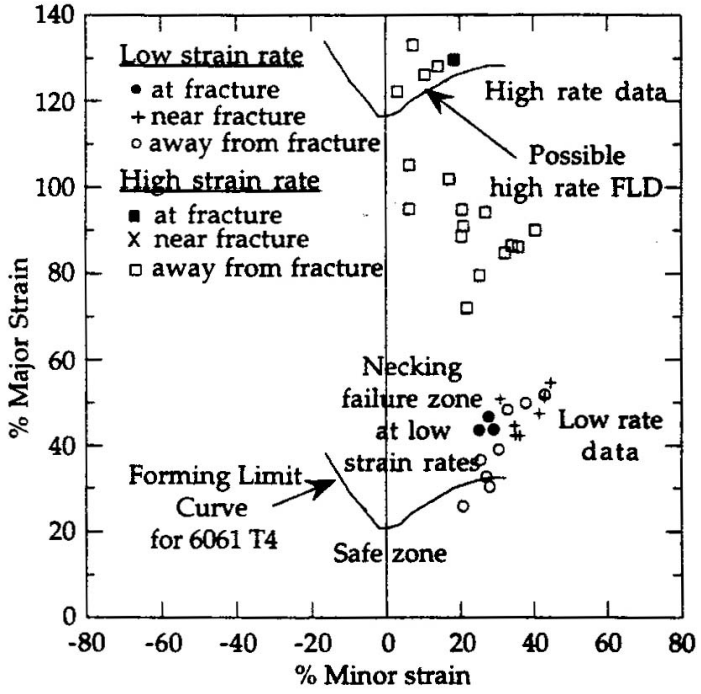

Figure 5: Formability data for electrohydraulically formed AA 6061 [14,15].

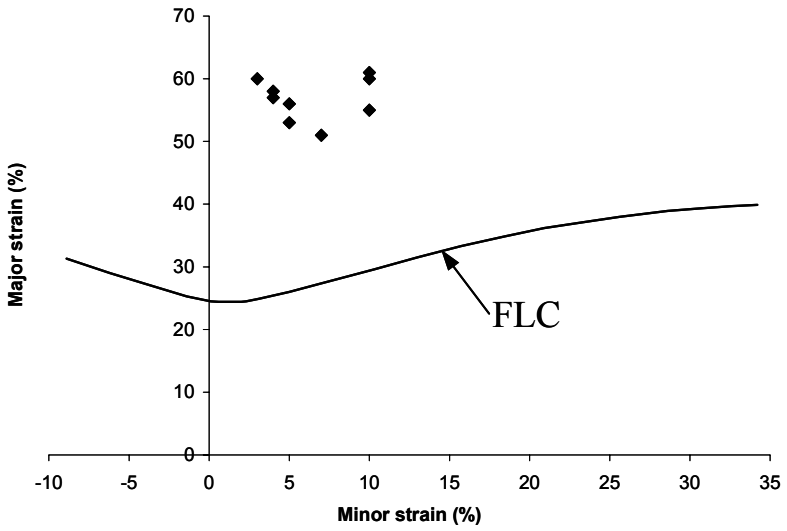

Figure 6: Formability data for AA6111-T4 EM formed into a V-die (taken from Golovashchenko *et al.* [16]). Forming limit curve (FLC) provided by ALCAN International [20].

1.4 Factors that Influence Formability in High Velocity Forming

The increases in formability observed in high speed forming have been attributed to constitutive and inertial effects. Constitutive effects are introduced by so-called high strain rate behaviour of materials, while inertial effects encompass the effects caused by the velocity and velocity gradients within the parts, being formed and the rapid decelerations during contact with rigid tooling. This section looks at the published information available on these phenomena for aluminum alloys.

1.4.1 Constitutive Effects - High Strain Rate Behaviour of Aluminum Alloys

At high strain rates, some materials exhibit an increase in flow stress and ductility [21]. Although aluminum shows hardly any strain rate sensitivity in the strain rates involved in typical forming operations, at high strain rates, some aluminum alloys show strain rate dependence. The increased formability observed in high velocity forming processes has been attributed in part to strain rate effects. No data on the high strain rate properties of AA5754 and AA6111 was available when the work presented in this thesis was carried out. Obtaining this data is the focus of ongoing research at the University of Waterloo, and recent work on

AA5754 at strain rates in the order of 1000 s^{-1} by Smerd *et al.* [22] has shown that the flow stress exhibits very low strain rate sensitivity, while the elongation increases with strain rate. The available information indicates that the flow stress of most aluminum alloys is not strain rate dependant, but that the composition of the alloys plays an important role in how elevated strain rates affect properties. Since very little data on AA5754 and AA6111 has been published, data published on similar aluminum-magnesium and aluminum-magnesium-silicon alloys is presented in this review.

Figure 7 shows the strain rate sensitivity of pure aluminum and aluminum alloys, as compiled by Lindholm *et al.* [23]. A "strain sensitivity parameter" was used that is equal to the derivative of the flow stress with respect to the strain rate, normalized by the yield stress. It can be seen from the figure that the strain rate sensitivity decreases with decreasing purity and alloy strength.

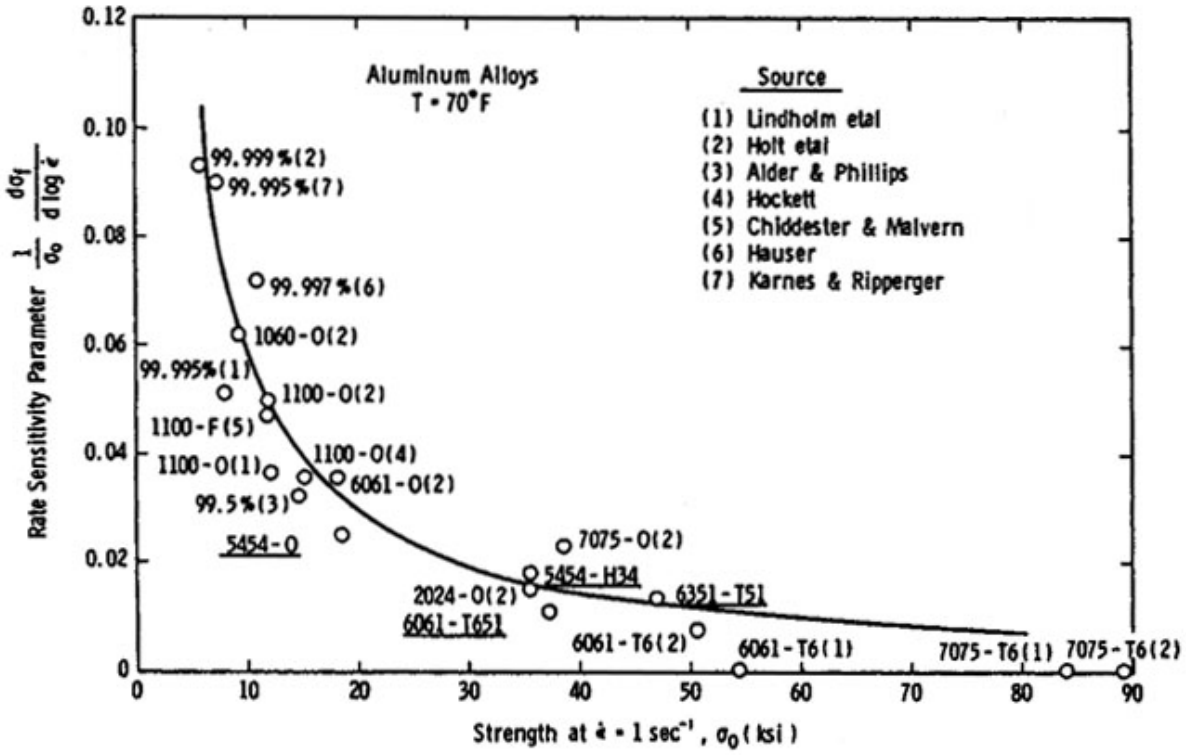

Figure 7: Strain rate dependence of several aluminum alloys compiled by Lindholm *et al.* [23].

Tensile data for wrought aluminum alloys 5454 and 6061 for strain rates in the range of 10^{-4} to 10^{3} s^{-1} by Lindholm *et al.* [23] is shown in Figure 8. Final elongation shows the

greatest sensitivity to strain rate, for the alloys tested, with the AA 5454 having the most dependence. The yield strength and the ultimate tensile strength show little strain rate dependance. The high strain rate data was obtained using a Hopkinson bar using a "top-hat" specimen design. The reader is referred to Gray [24] for an in-depth analysis of Hopkinson's bar testing.

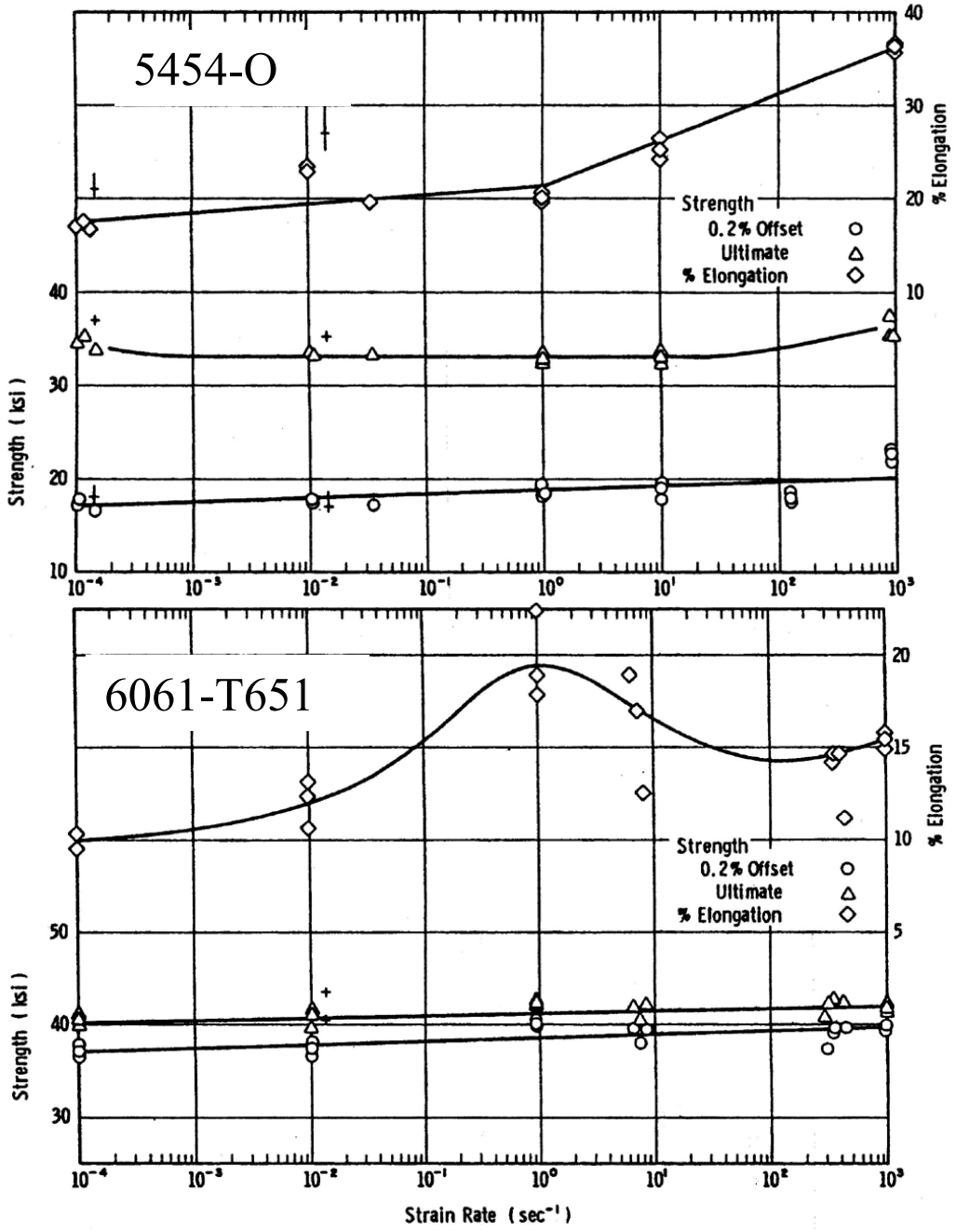

Figure 8: Mechanical properties versus strain rate for aluminum alloys 5454-O and 6061-T651 [23].

Tanaka and Nojima [25] performed compressive split Hopkinson bar testing on pure aluminum, Al 4.01wt% Cu and 17S Duraluminum (see Figure 9). The tests were performed at different temperatures, ranging from –195 to 450°C. They found that Al-4.01wt% Cu and 17S Duraluminum exhibited no strain rate sensitivity and no increase in flow stress (taken as the flow stress at 5% strain) at room temperature. At low and high temperatures, both alloys exhibited increased strain rate sensitivity and an increase flow stress. The final strain and flow stress increased monotonically for pure aluminum.

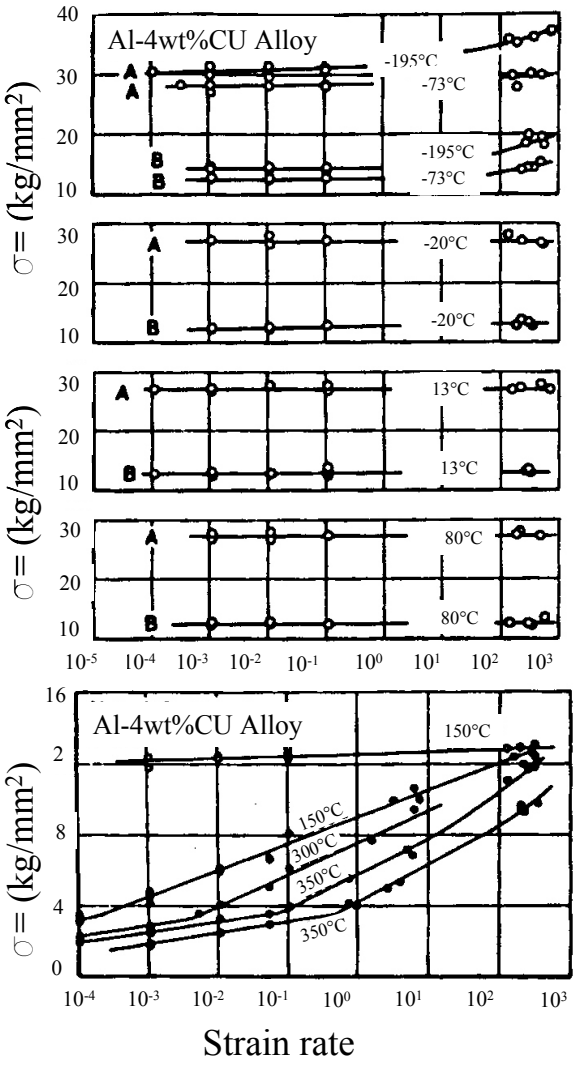

Figure 9: Flow stress at 5% strain vs strain rate for several alloys and temperatures from Tanaka and Nojima [25]. Stress units are kilogram, kg, divided by millimetre, mm, squared. A and B refer to alloys with different heat treatments, giving Vickers hardness of 98 and 34 respectively.

Data presented by Mukai *et al.* [26] for AA5056-O and AA5056 processed using equal-channel-angular-extrusion (ECAE) series alloy is shown in Figure 10. It can be seen from the figure that the alloys show little, if any, strain rate dependence in the range studied. A modified Hopkinson bar method was used for the high strain rate experiments [26].

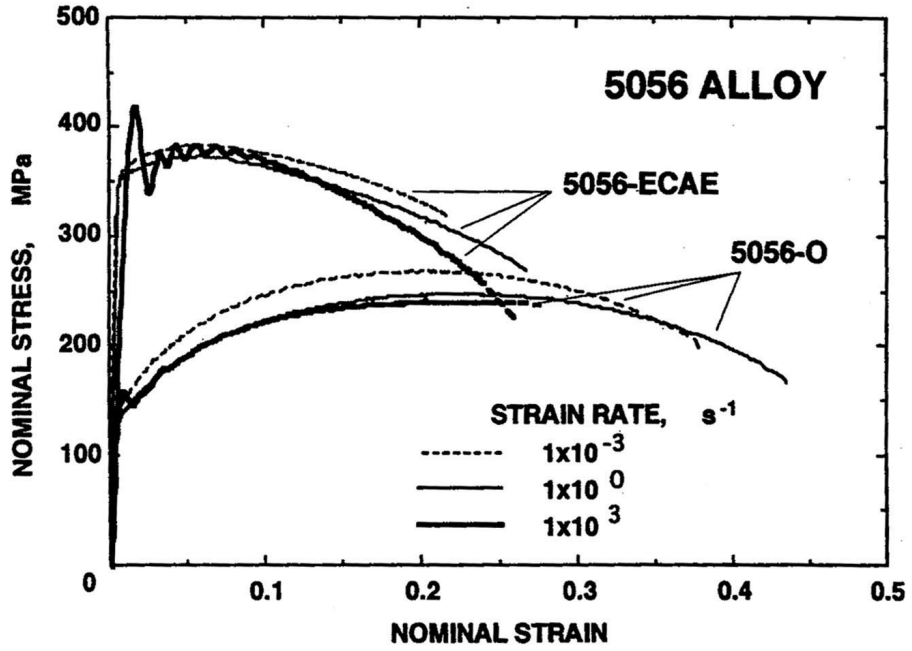

Figure 10: Stress versus strain data for AA 5056-O and 5056-ECAE [26].

Flow stress and elongation data for AA 5182 and other alloys reported by Higashi *et al.* [27] is shown in Figure 11. The flow stress of the AA 5182 shows negative strain rate sensitivity up to approximately 1000 s^{-1}, and then increases with the final flow stress being approximately 10% larger than the quasi-static value. In contrast, the elongation to failure increases with strain rate.

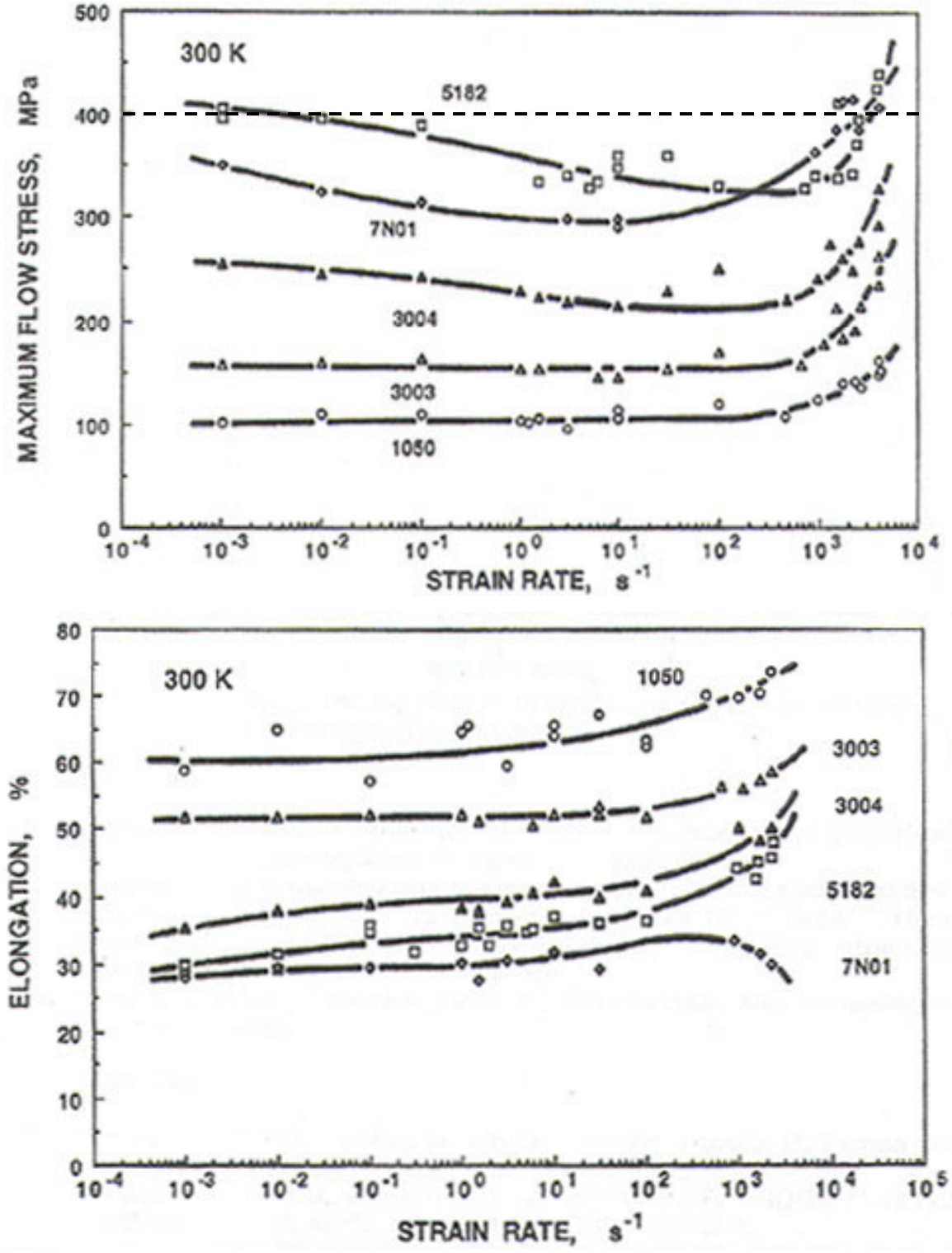

Figure 11: Flow stress and elongation data for several aluminum alloys presented by Higashi *et al.* [27]. The present author added the horizontal dashed line to illustrate how the strain rate sensitivity can be both negative and positive for the same material at different strain rates.

Oosterkamp *et al.* [28] tested AA 6082 T6 and AA 7108 T79 alloys at different strain rates and temperatures using a compressive split Hopkinson bar test. Low rate sensitivity was observed for the AA 6082 at room temperature (see Figure 12). Note that the last data point for the room temperature test seems to show negative strain rate sensitivity.

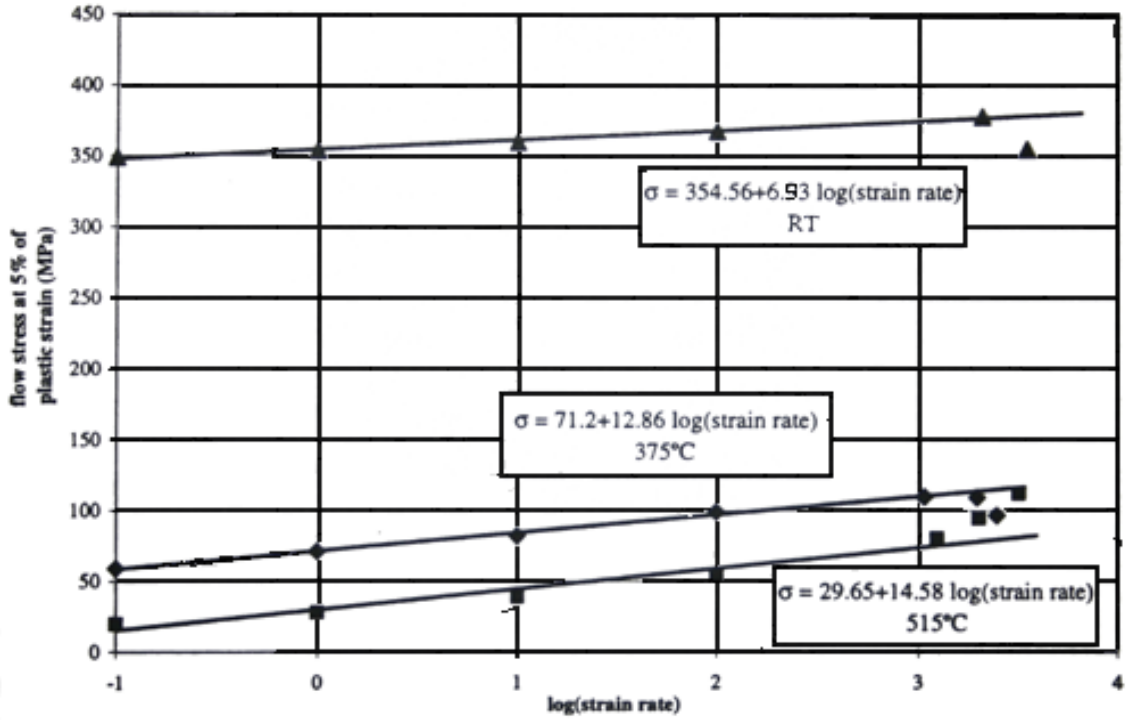

Figure 12: Flow stress at 5% strain for AA 6082-T6 at room temperature, 375 and 515 °C [28].

To summarize, the published work indicates that some aluminum alloys are strain rate sensitive at high strain rates. The strain rate sensitivity seems to be dependent on the alloy composition, with pure aluminum being the most strain rate sensitive. Very limited work is available on aluminum alloy sheet, which, to some degree, will behave differently due to the anisotropy of sheet material. Due to the dependence of strain rate sensitivity on composition, each alloy must be characterized individually at the strain rates involved in the particular application.

1.4.2 Inertial Effects

It has been reported by many authors that inertial effects increase ductility [14,15,29,30,31,32,33,34,35]. These effects occur in addition to any rate sensitivity of the material. The reasons for this increase in ductility are not yet completely understood; however, several theories have been proposed.

Rajendran and Fyfe [29] studied the ductile failure of thin rings numerically and experimentally. They observed an increase in ductility that they attributed to inertial effects since it was present for strain rate dependant and independent materials. Numerical models that considered the material as porous and non-porous were compared. It was found that the critical void volume fraction provided a failure criteria applicable to conditions were inertia is important and that it gave a more realistic failure strain for porous materials. It was reported that the critical void volume fraction was essentially strain rate independent.

Ragazzoni *et al.* [31] proposed that the increase in elongation was caused by an unloading front, which results in an extra amount of deformation in the non-localized region of the part (see Figure 13).

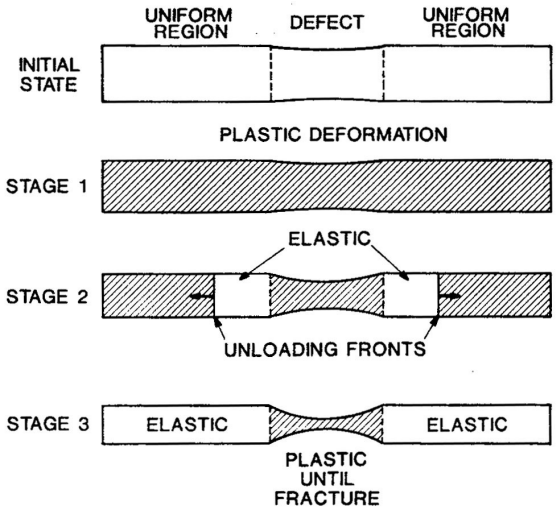

Figure 13: Ragazzoni *et al.'s* proposed unloading front [31]. In stage 1 the material is deforming plastically throughout. Elastic waves emanate from the defect in stage 2, which eventually lead to localization of the plastic deformation in the defect in stage 3.

Another theory proposes that necking is retarded by the inertial forces caused by the difference in velocity within the part [14,15,32-35]. When a sample is deforming, different parts of the body will have different velocities ranging from zero at the clamped edge, to the test velocity on the moving end. At high speeds, the difference can be substantial enough to produce an inertial force opposite to the applied force as the material at different locations of the sample accelerate to the test velocity. Several researchers [14,15,32-35] have argued that this inertial force reduces the net load on the part retarding necking (see Figure 14). Increases in ductility relative to quasi-static deformation of up to 60 and 150 % were reported for electromagnetically expanded fractured thin rings of AA6061 and AA6061 T6, respectively [35].

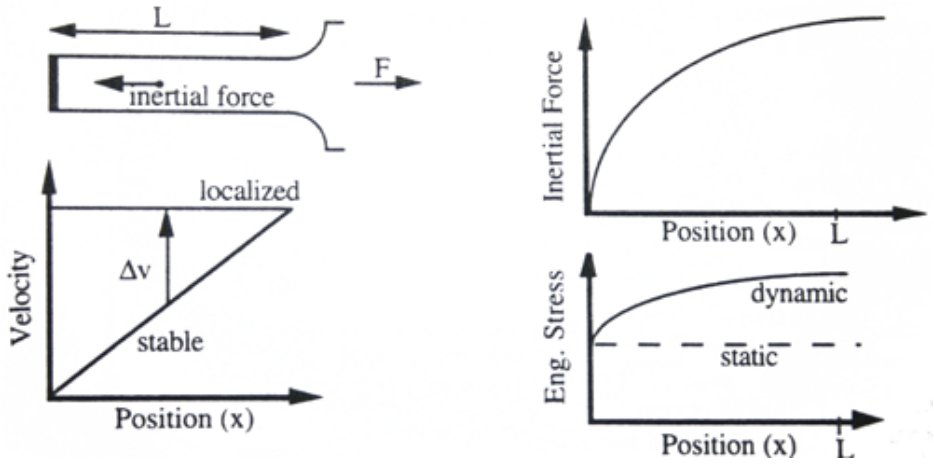

Figure 14: Inertial force neck retardation effect as proposed by Balanethiram and Daehn [14].

1.4.3 Tool/Sheet Interaction Effects

The data presented in Figure 5 and Figure 6 for sheet formed into dies at high speeds show increases in formability that are larger than the increases in ductility that have been reported in high strain rate experiments. Thus, the increase in formability cannot be due exclusively to constitutive and inertial effects. Figure 5 shows increases in major strains for AA 6061 in the order of 150% when formed with electrohydraulic forming. In contrast, Figure 8 shows increases in elongation for AA 6061 of only 50% at high strain rates when compared to quasi-static testing. The difference is enough to suggest that other mechanisms

are at play, even considering the possibility of differences between the material condition, temper, etc.

One obvious difference between the high strain rate tests and high speed forming processes, like EMF, is the interaction between the workpiece and the tool. In a high speed forming process, the material will impact the die at high speeds. This tool/sheet interaction has not been extensively studied.

Balanetherian [15] proposed that when a sheet of material impacts a die at high velocities, a compressive through-thickness stress is generated (see Figure 15). Balanetheriam [15] suggested that the compressive forces "contribute to stretching of the sheet metal instead of localization", in a form of "inertial ironing" not unlike the ironing process used in can manufacturing and spinning processes.

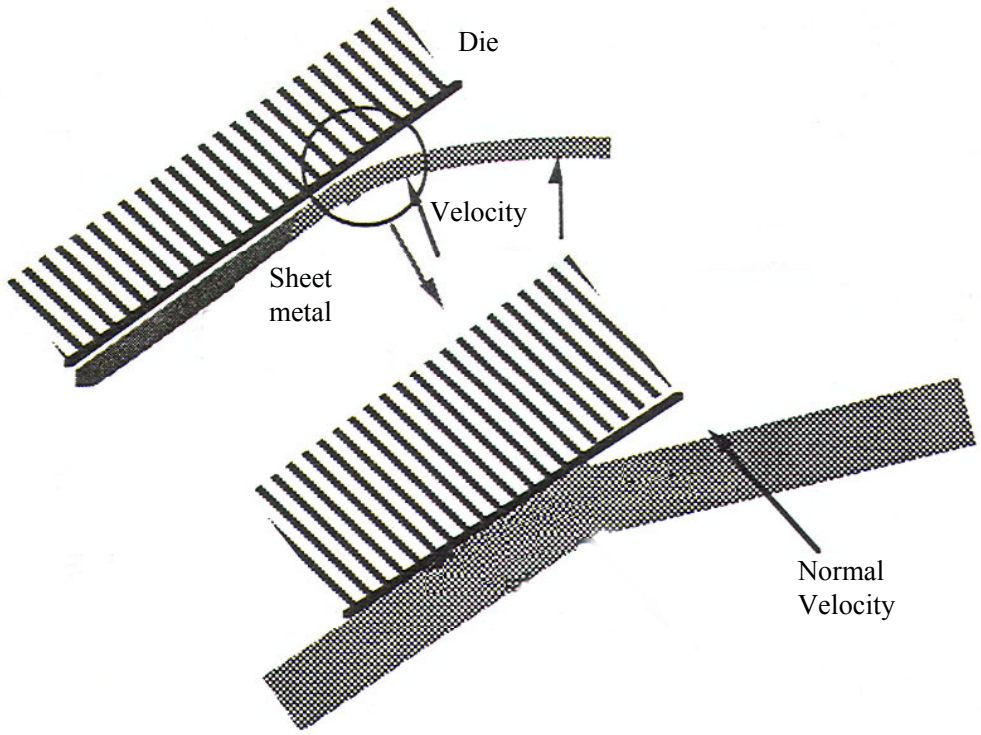

Figure 15: Schematic diagram illustrating the inertial ironing effect [15].

The pressure caused by the impact of the workpiece on the tool has been examined by Golovashchenko [36] who reported compressive stresses on the order of the yield strength, for

tubes expanded into a die. Fenton and Daehn [37] have also studied the impact pressures created by sheet forming, and found that they peaked at approximately three times the yield stress of the material.

1.5 Effects of EM Forming on Properties of Aluminum

In general, the available literature ignores any effects the EM field itself has on the mechanical properties of aluminum. Skripnichenko [38] reported that the yield stress of aluminum decreases with exposure to a pulsed EM field. This was determined by exposing a sample in a quasi-static, one dimensional tensile test, to several EM pulses. It was reported that the majority of the decrease in yield stress occurred after the first pulse, and that additional pulses had a decreased effect. An explanation for this behaviour was not presented. Figure 16 shows some of the results. This paper is only one of several from the same author and his co-workers; unfortunately, most of the papers have proved very difficult to obtain and are available only in Russian.

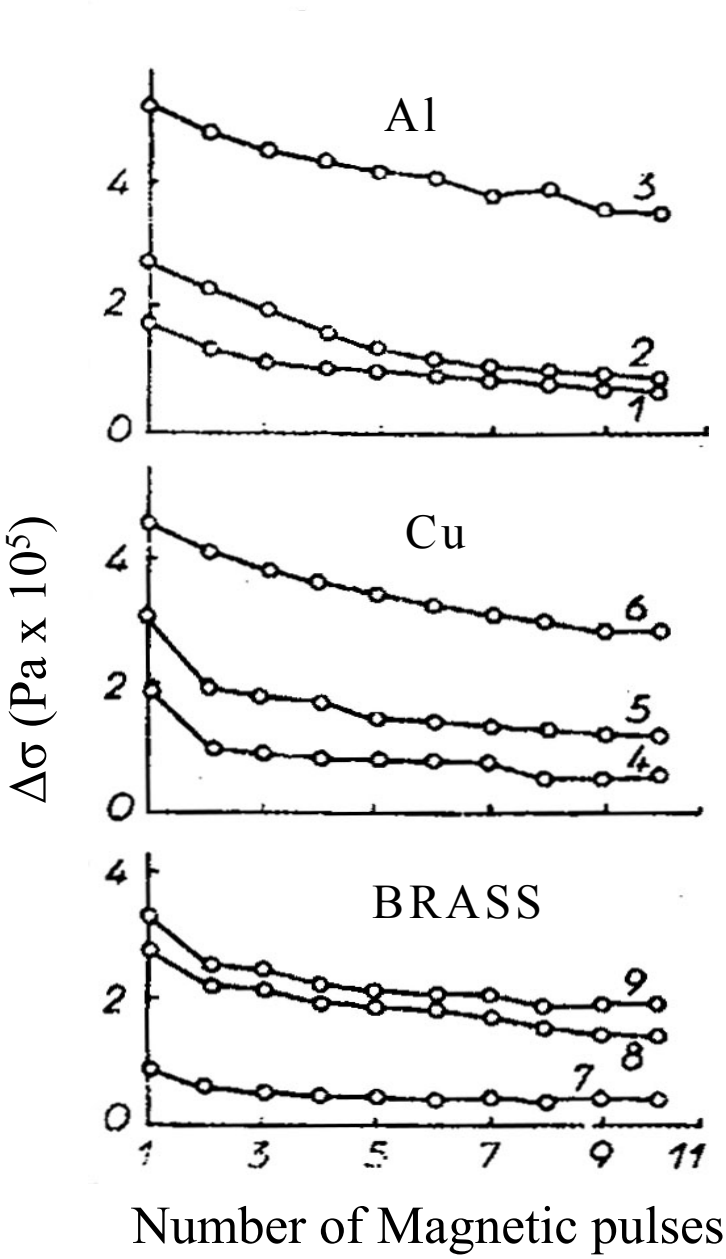

Figure 16: Change in flow stress ($\Delta\sigma$) versus number of magnetic pulses. Figures are, from top to bottom for pure aluminum, copper and brass [38].

Given the importance of the high strain rate effects, inertial effects and the tool/sheet interaction, the reduction in yield strength that results from exposure to EM pulses seems to be of second order importance. Figure 16 supports this, since the reduction in yield stress for aluminum is approximately 0.2 MPa. Despite this, they should be further investigated in the future.

1.6 Failure of Ductile Materials

Failure in ductile materials is characterized by an area of localized plastic deformation, be it a neck or shear band that eventually leads to fracture. Ductile materials exhibit three types of failure: plastic failure, ductile fracture and shear fracture (see Figure 17) [39]. In plastic failure, the material of the neck continues to deform to a point or line (see Figure 17a). This type of failure typically occurs in pure materials with no second-phase particles or impurities, and when all other failure mechanisms are suppressed [39,40]. An important characteristic of this type of failure is that there is no volume change. Since the term plastic failure has been used extensively to describe all types of failure in ductile materials, the term "plastic collapse" will be used henceforth to describe plastic failure.

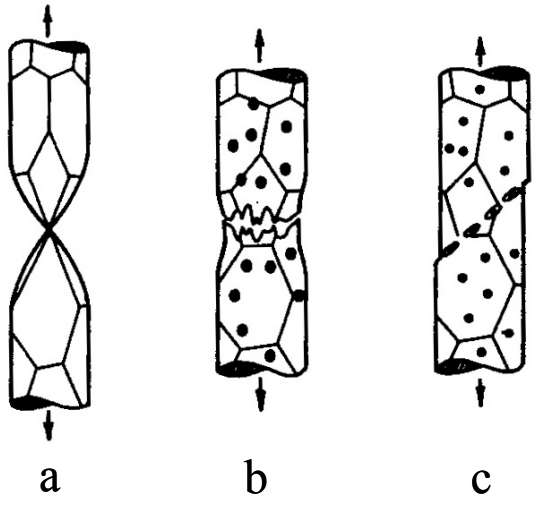

Figure 17: Fracture modes for ductile materials: a) plastic collapse, b) ductile failure and c) shear fracture [39].

Materials that are not pure will fail by either ductile or shear fracture. Ductile fracture is depicted in Figure 17b. After a critical amount of deformation occurs, the plastic deformation localizes in a neck. Voids or "damage" form in the neck, grow as the strain increases and eventually coalesce to form a crack. The material will fracture shortly after the crack forms. In shear fracture (see Figure 17c) an area of very high shear strain, called a shear band, forms in the material. Within the shear band, voids can nucleate and elongate, eventually linking and producing a fracture; this process is referred to as shear banding.

Failure in a shear band can also occur without any significant void formation, in a manner analogous to plastic collapse.

1.6.1 The Role of Microvoid Damage

For ductile fracture or shear banding to occur, microvoids must nucleate, grow and coalesce leading to microvoid damage and eventually failure. Voids can nucleate at grain boundaries, [41] or, more commonly, from second phase particles and inclusions [41,42]. This review will concentrate on the latter mechanism, since the former is associated with deformation at intermediate to high temperatures [41]. Henceforth, microvoid damage will simply be referred to as damage. Voids will usually form through either de-cohesion of the particle/matrix interface or from the fracture of second phase particles [42]. Uniform particles with low aspect ratio will usually nucleate voids by de-cohesion, whereas irregularly shaped particles with large aspect ratios will typically do so by fracture (Figure 18) [41].

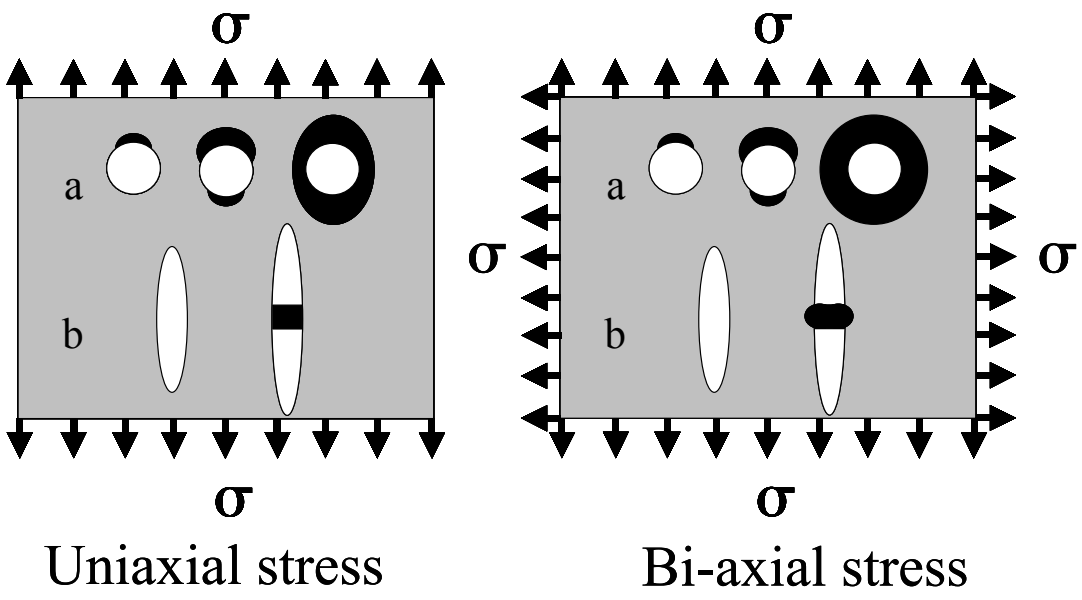

Figure 18: Simplified view of the two types of void formation; a) de-cohesion of the particle matrix interface and b) particle cracking.

Once voids nucleate they must grow in order for the material to eventually fail. Their rate of growth will depend on the magnitude of the hydrostatic stress they are subject to. Hydrostatic stress is given by;

$$\sigma_h = \frac{1}{3}\left(\sigma_{11} + \sigma_{22} + \sigma_{33}\right) = \frac{\sigma_{kk}}{3} \tag{1-1}$$

Where the summation convention is adopted. Hydrostatic stress is typically non-dimensionalized by the flow stress and referred to as "triaxiality."

The most favourable stress state for void growth is a large positive (tensile) hydrostatic stress, produced when the principal stresses are all positive, as shown in Figure 19. In a neck, the triaxiality is very high [43]; thus, once the material localizes, the voids in the neck will start growing at much faster rate than in the rest of the material, eventually leading to coalescence and fracture.

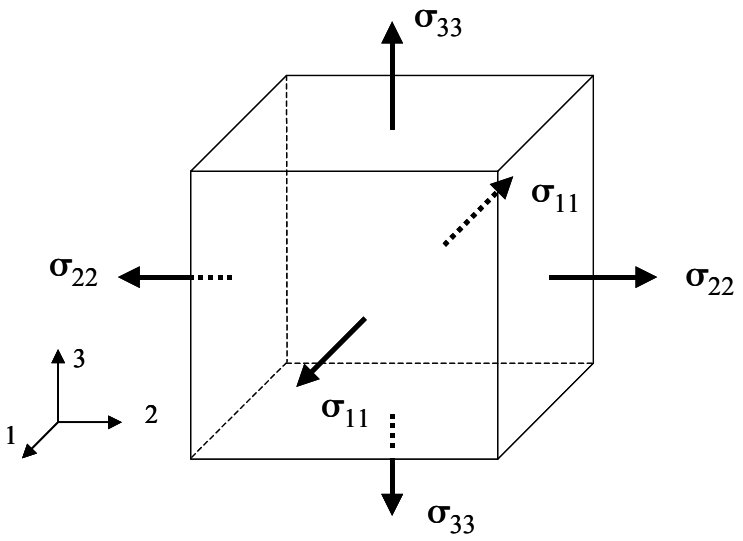

Figure 19: The most favourable stress state for the growth of voids is a positive hydrostatic stress state, *i.e.* $\sigma_{11}=\sigma_{22}=\sigma_{33} >> 0$.

Void coalescence is the final step before the formation of a crack and eventual fracture. Once the voids reach a critical size they will start coalescing to form bigger voids. Coalescence will occur when the void's length is approximately equal to the spacing between them [41, 44]. As voids coalesce and become larger, they start coalescing with other voids, rapidly resulting in the loss of material strength.

1.6.2 Damage Suppression by Hydrostatic Pressure

If a positive hydrostatic stress promotes void growth and thus an increase in damage, it is logical to think that a negative hydrostatic stress (a hydrostatic pressure) will retard or even suppress void growth. This effect has been demonstrated in numerous studies [39,45,46,47,48,49]. Materials deformed under hydrostatic pressure have shown an increase in ductility and a change in failure mode from ductile fracture to plastic collapse or even brittle fracture [47-49]. Figure 20 shows the difference in failure mode in an Al-Cu alloy deformed at ambient pressure and under a hydrostatic pressure of 300 MPa, as reported by French and Weinrich [49].

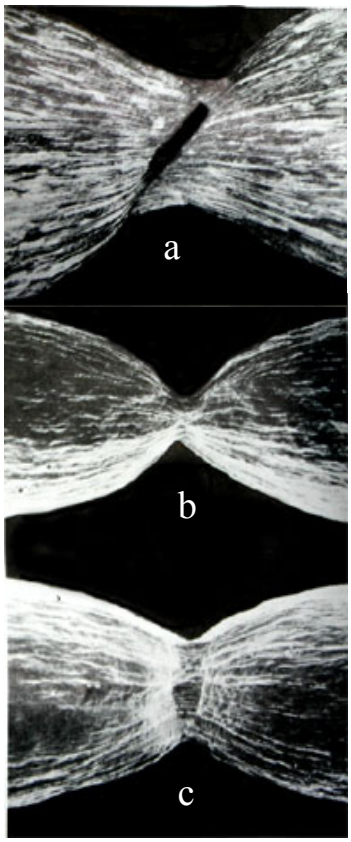

Figure 20: Aluminum-Copper alloy deformed at a) ambient pressure and b) and c) with a hydrostatic pressure of 300 MPa. Images b and c show views of the neck of the same specimen at 90º from each other [49].

As discussed by Lewandowski and Lowhaphandu [45] shear band failure is not suppressed by superimposed hydrostatic pressure. Materials that fail predominantly in this mode will not benefit from being formed under a high hydrostatic pressure environment.

A more comprehensive review of the literature on the effects of hydrostatic stress on ductility and failure modes is beyond the scope of this work. The reader is referred to Lewandowski and Lowhaphandu [45] for an in-depth review.

1.7 Simplified Analysis of EM Forming Processes

A simplified analysis of the EM forming process is presented here to familiarize the reader with the basic principles of the process and how the forming pressures are generated. The circuit used in EM forming can be simplified as an RLC circuit, to perform a first order analysis. Figure 21 shows the simplified circuit [4-7].

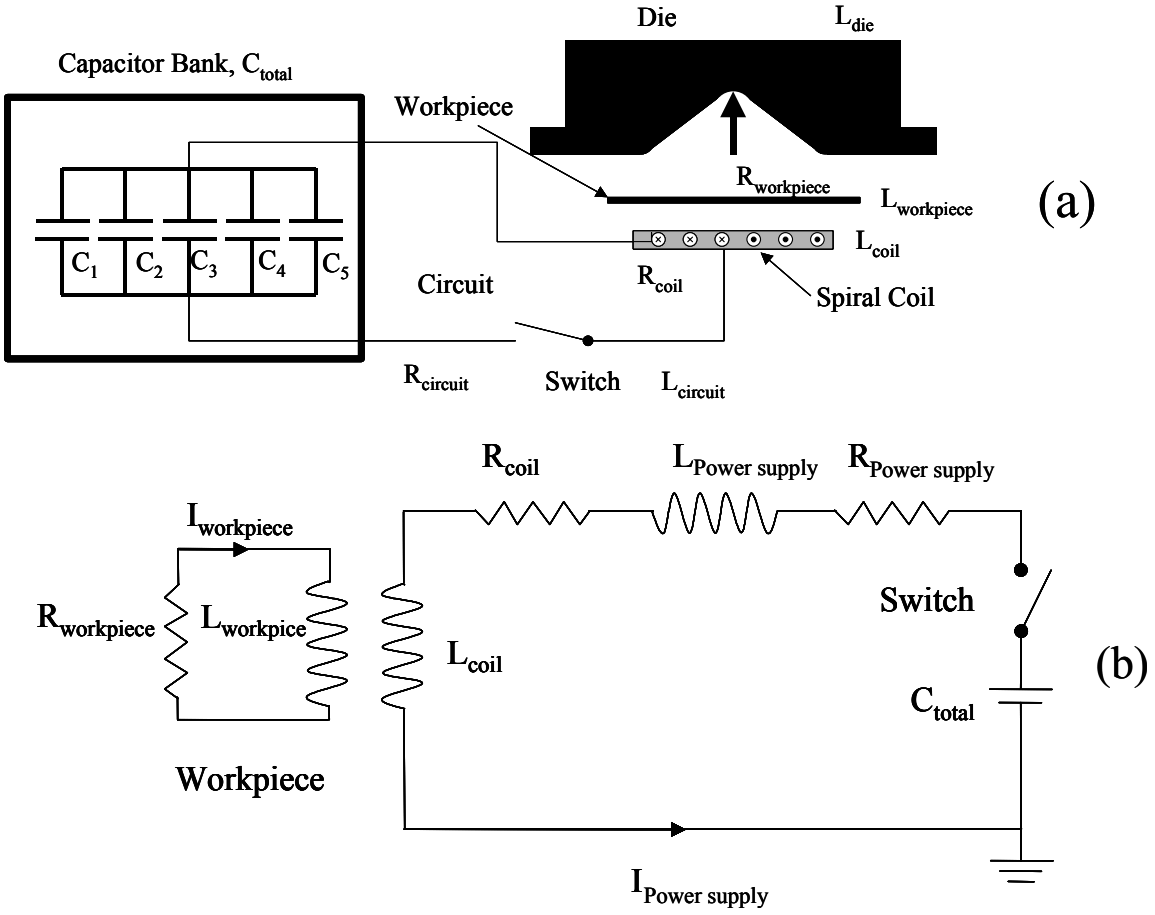

Figure 21: a) schematic illustration of an EM forming system, b) simplified EM forming circuit.

The current discharged through the coil in this circuit can be described by the following differential equation [4]:

$$\frac{d^2I(t)}{dt^2} + 2\xi\omega\frac{dI(t)}{dt} + \omega^2 I(t) = 0 \tag{1-2}$$

$$\xi = \frac{1}{2}R_a\sqrt{\frac{C}{L_a}} \tag{1-3}$$

$$\omega = \sqrt{\frac{1}{L_a C}} = 2\pi f \tag{1-4}$$

where I = current in Amperes, t= time in seconds, R = resistance in Ohms, C = capacitance in Farads and f= frequency in Hertz.

$$R_a = R_{coil} + R_{power\ supply} \tag{1-5}$$

and,

$$L_a = L_{coil} + L_{power\ supply} \tag{1-6}$$

where L = inductance in Henrys

The discharge current profile given by this equation is shown in Figure 22. The resulting current profile has oscillates between positive and negative values and decays with time.

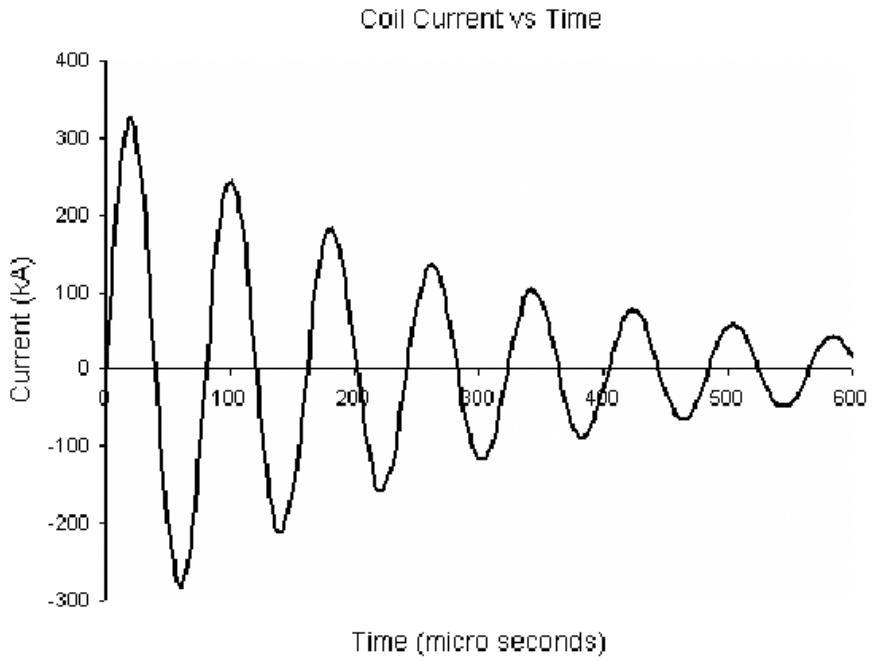

Figure 22: Current versus time profile given by the solution equation 1-2 [6].

In an actual EMF process, the current profile would be quite different, as shown in Figure 23. The process only lasts for a few microseconds and the current is prevented from becoming negative by adding a diode to the circuit to avoid damage to the capacitors, which do not react well to changes in the sign of the applied current [6].

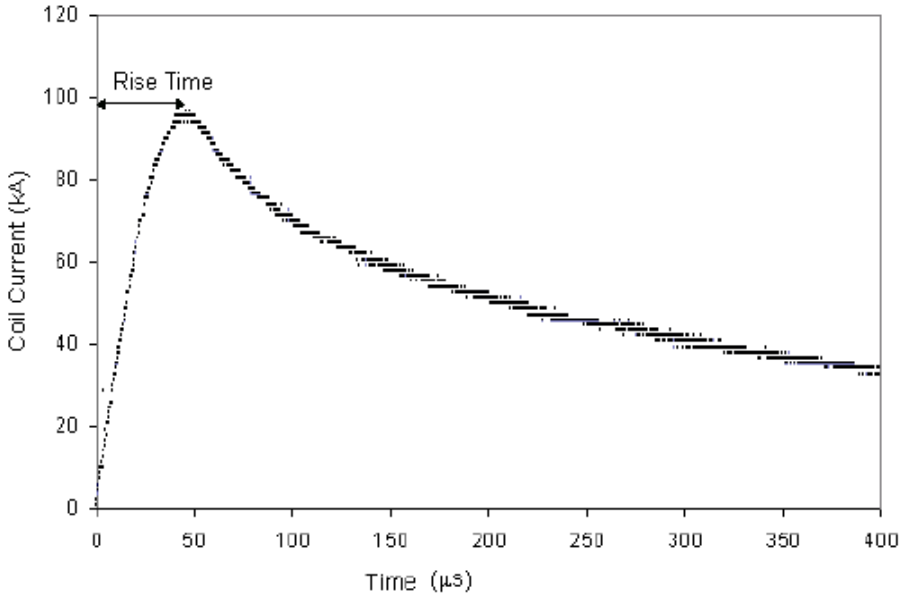

Figure 23: Current versus time profile for an actual EM forming coil [6].

The simplified analysis does not take into account the changes in the magnetic field caused by the deformation of the workpiece. These changes can have significant effects, as shown by Oliveira [6]. Numerical analysis is required to analyze these effects and a more rigorous analysis of EM forming theory is offered by Belyy *et al.* [50].

1.7.1 Magnetic Pressure Distribution

The magnetic field in the coil and the magnetic field induced in the sheet repel each other resulting in a body force on the sheet that is typically referred to as the magnetic pressure. Analyzing the interactions between a varying magnetic field and a deforming workpiece is not a trivial matter. The magnetic pressure is given by [6]:

$$P = \frac{\mu_o H^2}{2} \tag{1-7}$$

where P = pressure in Pascals, μ_o = permeability of free space and H = electromagnetic intensity.

The electromagnetic intensity varies with time, location, applied current and geometry, and is very hard to determine. Electromagnetic intensity distributions for idealized spiral coils have been analytically determined, but no general analytical solutions exist for sheet metal forming operations with flat coils.

Despite the complexities of the problem, Plum [8] reports an empirical formula that can be used to determine the magnetic pressure required to form a part from a tube. The relationship is given by:

$$\frac{(YS)(2t)}{OD} = P_y \tag{1-8}$$

$$(P_y)(N) = P_m \tag{1-9}$$

where YS = yield strength, t = wall thickness, OD = outer diameter, P_y = pressure to yield the hoop, P_m = magnetic pressure, N = a correction factor that ranges from 2 to10. The correction factor N accounts for inertial effects, high strain rate effects and the geometry of the part [8]. The formula works for both SI and Imperial as long as consistent units are used. Magneform [51], a company with over 40 years of experience in EM forming, developed and uses this

formula. An obvious problem with this approach is the correction factor, which can have a value anywhere from 2 to 10 [8].

1.7.2 Magnetic Pressure Distribution on a Sheet Caused by an Idealized Spiral Coil

Al-Hassani [12] determined theoretical magnetic pressure distributions caused by different coils on flat conductive plates. Several simple geometries were analyzed which led to an expression for the magnetic field intensity and the pressure distribution caused by a spiral coil. The equations for the magnetic field intensity, H, and pressure distribution, P, are;

$$H_r = \frac{IN}{\pi}\left\{\tan^{-1}\left[\frac{-2gr}{g^2+a_2^2-r^2}\right]+\tan^{-1}\left[\frac{-2gr}{g^2+a_1^2-r^2}\right]\right\} \qquad (1\text{-}10)$$

and,

$$P_r = \frac{\mu_o I^2 N^2}{2\pi^2}\left\{\tan^{-1}\left[\frac{-2gr}{g^2+a_2^2-r^2}\right]+\tan^{-1}\left[\frac{-2gr}{g^2+a_1^2-r^2}\right]\right\} \qquad (1\text{-}11)$$

where I = current in Amperes, N = number of turns in the coil, g = distance from the coil to the workpiece in meters, a_1 = distance from the centre of the coil to the first wind of the coil meters, a_2 = distance from the centre of the coil to the last wind meters and r = radius in meters.

The theoretical predictions were compared with experimental results [12]. A comparison between the analytical predictions and experimental results for a spiral coil is shown in Figure 24, which shows reasonably good agreement between the theoretical and measured values.

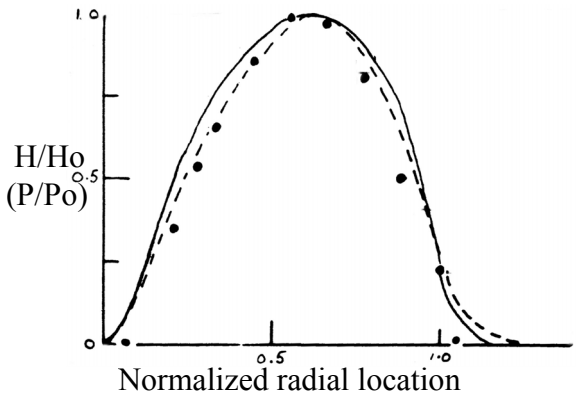

Figure 24: Normalized predicted (solid line) and measured (dashed line and points) magnetic intensity (and pressure) distribution versus radial position for a spiral coil, as reported by Al-Hassani [12]. Ho and Po are the maximum magnetic intensity and pressure, respectively.

1.7.3 Skin Effect

A magnetic field will penetrate a surface of a workpiece a distance δ, given by [6]:

$$\delta = \sqrt{\frac{2}{\mu_o \sigma \omega}} \tag{1-12}$$

where σ = conductivity, ω = ringing frequency (2π x frequency) in Hertz and μ_0 = permeability of free space. δ will be given in meters when standard SI units are used.

Magnetic field frequencies within a certain range will cause the skin penetration greater than the thickness of the sheet, leading the field to "leak" through the workpiece, thus reducing the effect of the forming operation [6,52]. Therefore, an optimal skin depth exists for EM forming processes [6,52].

1.8 Numerical Simulation OF EMF

In conventional forming operations, analytical solutions for all problems are not available and numerical methods, principally finite element analysis (FEA), are used to simulate the processes. The same is true for EMF processes, with the added complication of the time varying magnetic fields. Three numerical approaches have been used to model the EMF process:

- Use of a structural FEA code with an analytical pressure distribution;
- Use of an EM code to calculate the pressure distribution, which is then used in a structural code ;
- Simultaneous solution of the EM and structural equations.

Applying an analytical pressure distribution to the workpiece in a structural FEA code is the simplest way to model the process, since it does not require time consuming and expensive EM computations of the time varying magnetic fields and pressures. Analytical pressure distributions are used as input to a structural code. Accuracy is sacrificed since many simplifying assumptions are used to derive the analytical solutions, such as infinite sheet length, ideal coils and the EM pressure does not change with the deformation of the workpiece. This approach has been used to model tube forming processes by Lee and Lee [53] and Mahanian and Blackwell [54], and for sheet forming by Shangyu *et al.* [55] with good agreement between experiment and numerical models.

The second approach involves using an EM code to calculate the pressure distribution and passing this information to a structural code. This can be done once at the beginning of the simulation, or it can be repeated at discrete intervals throughout the duration of the simulation, leading to what is referred to as a "loosely coupled" code [6,56,57,58]. This process can capture the variation of the pressure distribution caused by the deformation of the workpiece [6,56,59]. Oliveira [6], Oliveira and Worswick [57] and Oliveira *et al.* [60] compared the results of a loosely coupled analysis with experiments and found good agreement between them. This approach has the advantage of being able to use proven codes that can handle complex 3-D structural and EM calculations; however, it is computationally

expensive since two codes must solve the respective problems and communicate with each other while doing so.

Codes that can simultaneously solve the EM and structural equations are called "coupled" or "fully coupled" codes. They provide the best available simulation of the time varying pressure distribution, at substantial computational cost [61]. Another draw back is that they are not widely available, which forces investigators to develop their own codes [36,37,62,63,64,65,66]. Bendjima and Féliachi [62] and Bendjima *et al.* [63] and Golovashchenko [36] have developed coupled codes for modeling tube EMF. Fenton and Daehn [37] used a 2-D Arbitrary Lagrangian Eulerian (ALE) hydrodynamic code to analyze free forming and die forming of a blank using a spiral coil. Stiemer *et al.* [65,66] developed a coupled 2-D finite element code which has been used to simulated free forming as well as die forming operations. All the authors report good agreement with experimental results for free formed parts. No proven codes that can handle 3-D fully coupled solutions are commercially available to the author's knowledge.

For a detailed review of electromagnetic theory and the modeling of coupled electromagnetic and structural problems the reader is referred to Oliveira [6] and El-Azab *et al.* [61].

1.9 Present Work

The aim of the present work was to determine if the formability of aluminum alloy sheet increases under electromagnetic forming conditions and, if so, to explain the reasons for the increases. To this end, an experimental and numerical program was carried out. Two commercially available alloys were chosen for the experimental work, AA5754 and AA6111, in the form of 1mm thick sheet. These alloys were chosen since they are currently in use in the automotive industry and are candidates for the fabrication of lightweight automotive body panels. The experiments consisted of forming free-formed (open-cavity die) and in-die conical samples using a spiral coil. This approach was chosen to try to isolate inertial and constitutive contributions to increased formability from contributions due to the interaction of the sheet with the tool (*e.g.* inertial ironing). Any formability increase observed in free forming could be safely attributed to inertial and constitutive effects, while any additional improvements

observed in the conical samples could be attributed to the tool/sheet interaction and its effects on the material.

To quantify the formability of the materials, the final strains were measured using the circle grid technique, and compared to the standard forming limit diagrams (FLD). The FLD was used since it is a widely accepted measure of formability in both academe and industry. Optical metallographic analysis was used to quantify the damage present in the experimental samples and to provide a comparison between the damage present in the free-formed, conical samples and the undeformed sheet. Scanning electron microscopy was also used for fractographic analysis to determine the nature of fractures produced.

Numerical simulations were carried out to help determine the details of the forming process and the causes of the increased formability. A modification of the Gurson-Tvergaard-Needleman damage-based material model was used. This type of model was chosen for its ability to predict damage evolution and ductile failure. Simulations were performed of both free-formed and in-die forming operations to discern any difference in the predicted damage rates.

The following chapters will present a detailed description of the experimental and numerical work carried out. Detailed descriptions of the experimental and numerical procedures used are in 0 and 0, respectively. Experimental strain measurements, metallographic and fractographic results are in Chapter 4, followed by the results of the numerical analysis, including validation of the model, in 0. A discussion of the results of this the work is presented in Chapter 6 and the conclusions and recommendations for future work are provided in Chapter 7.

CHAPTER 2

EXPERIMENTAL METHODS AND PROCEDURES

The experimental program consisted of forming sheet samples of AA5754 and AA6111-T4 using an EMF apparatus. Open cavity and conical dies were used to isolate the effects of the tool/sheet interaction from the high strain rate and inertial effects on formability.

2.1 Materials and Sample Preparation

2.1.1 Material Properties

The material compositions are shown in Table 1. The main difference between the alloys is that AA6111 contains less magnesium, and more silicon and copper than AA5754. Sheet of 1 mm nominal thickness was used, with actual thickness of 1.08 mm for the AA5754 alloy and 0.92 mm for the AA6111 alloy.

Table 1: Normal compositions (wt%) of AA5754 [20] and AA6111 [67] aluminum alloys.

Alloy	Mg	Mn	Fe	Si	Zn	Cu	Cr	Ti
AA5754	3.2	0.2	0.3	0.06	-	-	-	0.01
AA6111	0.5-1.0	0.1-0.45	Max 0.4	0.6-1.1	Max 0.15	0.5-0.9	Max 0.1	Max 0.1

The quasi-static true stress-strain curves for the alloys are shown in Figure 25. The yield stresses where 98.0 MPa for the AA5754 is and 135 MP for the AA6111 [20]. No high strain rate data for these alloys was available at the time of preparation of this thesis; however, the expected rate sensitivity is low (see section 1.4.1).

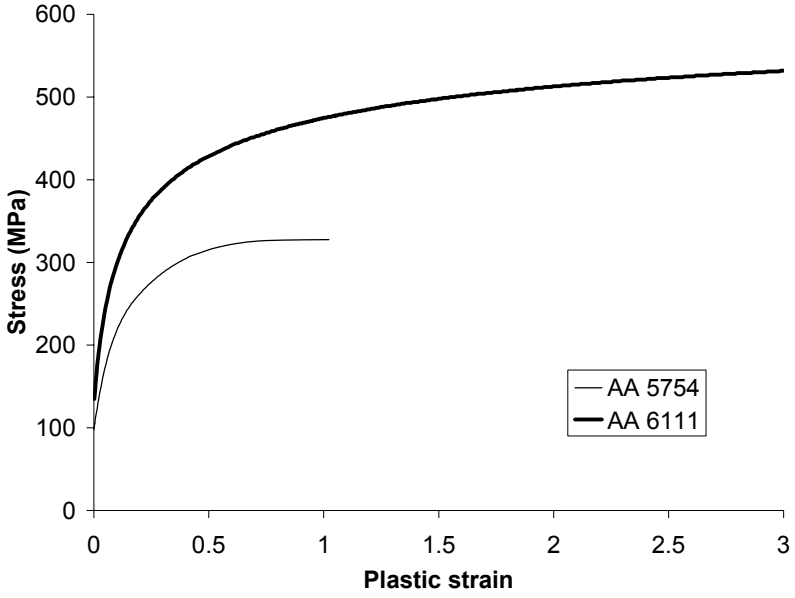

Figure 25: True stress-strain curves for AA5754 and AA6111 [20].

Due to scheduling difficulties, the experiments could not be carried while the AA6111-T4 was still "fresh" and the material had undergone between six to nine months of aging. The available quasi-static constitutive and formability data for this material is unfortunately not directly applicable to the aged material. The effects of the aging will be discussed when required throughout this work.

2.1.2 Sample Preparation

The material was cut into 165x165 mm (6.5x6.5 in) blanks prior to forming. Circle grids of 2.54mm (0.1 in) diameter were electrochemically etched on the blanks for post-forming strain measurements. The reader is referred to Oliveira [6] for a more in depth discussion on the circle grids used. The sheets were prepared for etching by thoroughly cleaning with detergent and acetone prior to etching. The AA5754 was supplied with a solid film lubricant, which was completely removed. The circle grids were electrochemically etched using Lectrotech 210A electrolyte [68] and a DC power supply.

2.2 Apparatus

The experimental set-up used is illustrated in Figure 26. The work piece is placed close to the coil, separated only by a thin insulating layer of Thermalux® between 2-4 mm thick. The die is then bolted in place to hold the blank, the bolts were tightened as much as possible with the principal requirement being no blank draw-in. The clamping force was not measured. The coil used was a 7-turn spiral coil with a nominal diameter of 100mm and a maximum diameter of 115 mm at the end.

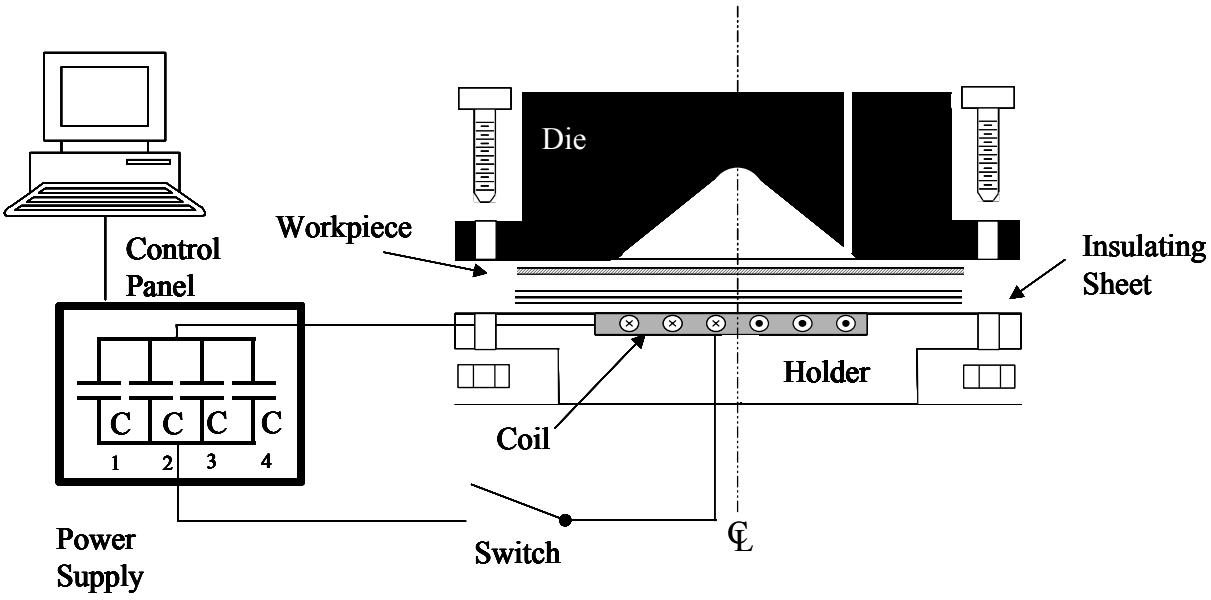

Figure 26: Schematic of experimental apparatus.

2.2.1 Power Supply and Experimental Set-Up

An IAP Magnepress [69] power supply with a storage capacity of 22.5 kJ at 15kV was used to form all of the samples. The power supply consisted of four capacitors of 50 μF each for a total capacitance of 200 μF. Tha system inductance, including three 1.5 m cables, was 230 nH. The maximum current capacity was 100 kA. Figure 27 shows the actual experimental apparatus used, which was located at Ford Motor Company's research laboratories in Dearborn, MI. The die was bolted to the base using six M10 nuts and bolts. A security bar was bolted to the die/holder assembly to prevent it from displacing from its

position due to the magnetic pressure (see Figure 28). Also seen is in the figure is a cap placed over the open cavity die, to prevent fractured pieces from leaving the die.

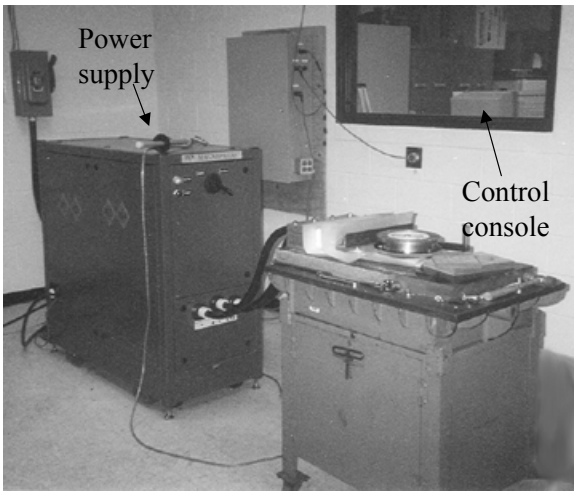

(a)

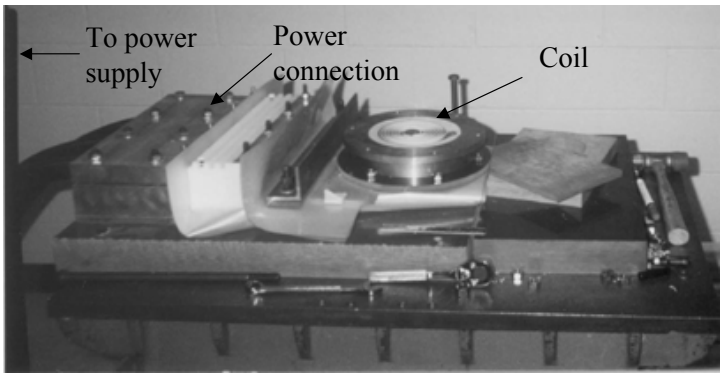

(b)

Figure 27: Experimental EMF apparatus; a) view of the complete apparatus including coil assembly, power supply and control panel and b) a close up of the coil assembly.

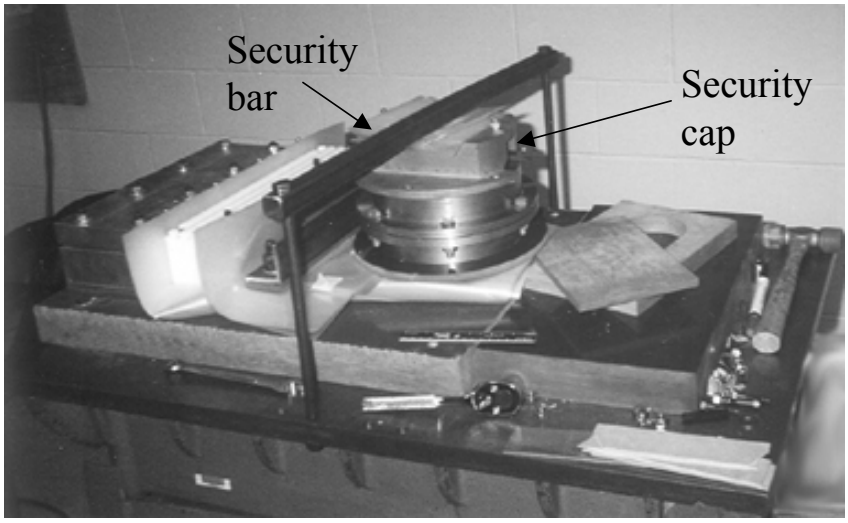

Figure 28: Apparatus ready for forming including security cap and bar.

2.2.2 Tooling

An open cavity die and three conical cavity dies were used in the experimental program. The open cavity die is illustrated in Figure 29. The die was made of unhardened mild steel, since the die was not going to be subjected to impact from the sheet. Six M10 bolts were used to fasten the die to the coil assembly (see Figure 28).

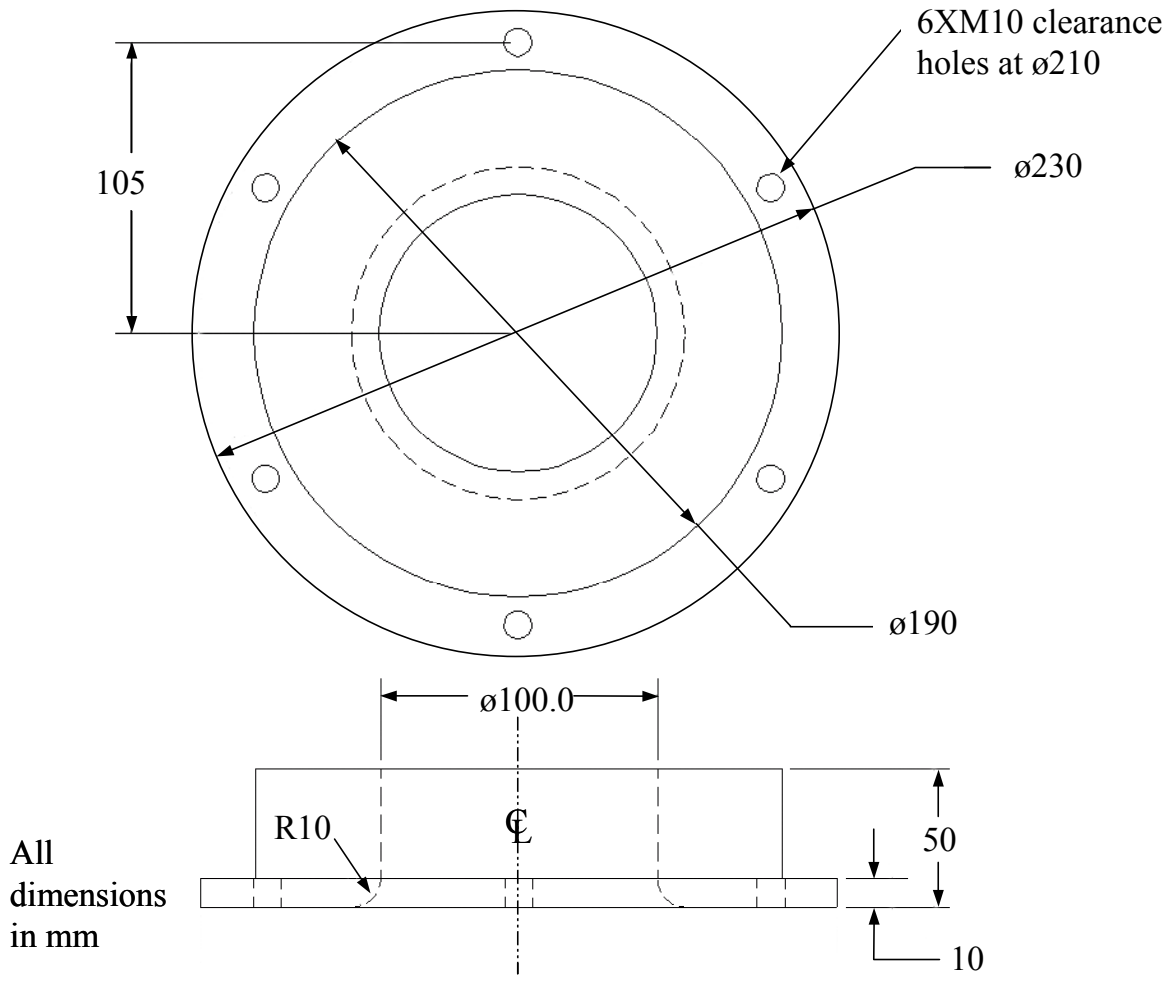

Figure 29: Drawing of the free forming die.

The conical cavity dies are shown on Figure 30 and Figure 31. The dies for the 40 and 45º experiments were made entirely from hardened tool steel (50 Rc), whereas the die for the 34º was comprised of a mild steel holder with a hardened insert (50 Rc). The heights of the cones for the different side angles are shown in Figure 30. The air from the dies had to be evacuated prior to forming. If this were not done, the trapped air would be compressed by the deforming sheet preventing complete filling of the die. Vacuum holes were placed as shown, in an attempt to prevent fracture of the tip, like that reported in references [14] and [15]. This vacuum hole location was not without problems, as will be discussed in Chapter 4. The conical tooling was designed and built at the University of Waterloo, while the free formed tooling was provided by Ford.

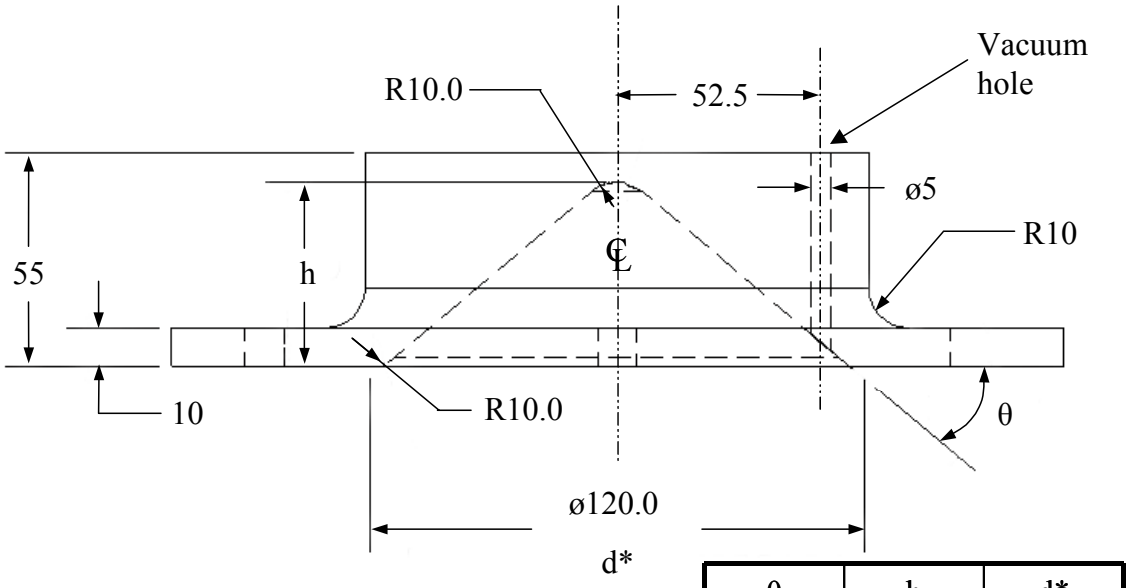

θ	h	d*
34º	37.98	126.0
40º	47.29	127.3
45º	55.86	128.3

Figure 30: Conical cavity die design for the 40 and 45º cone angles. Nominal cavity diameter 120.0mm, actual diameter (d*), with fillet, is shown in the table.

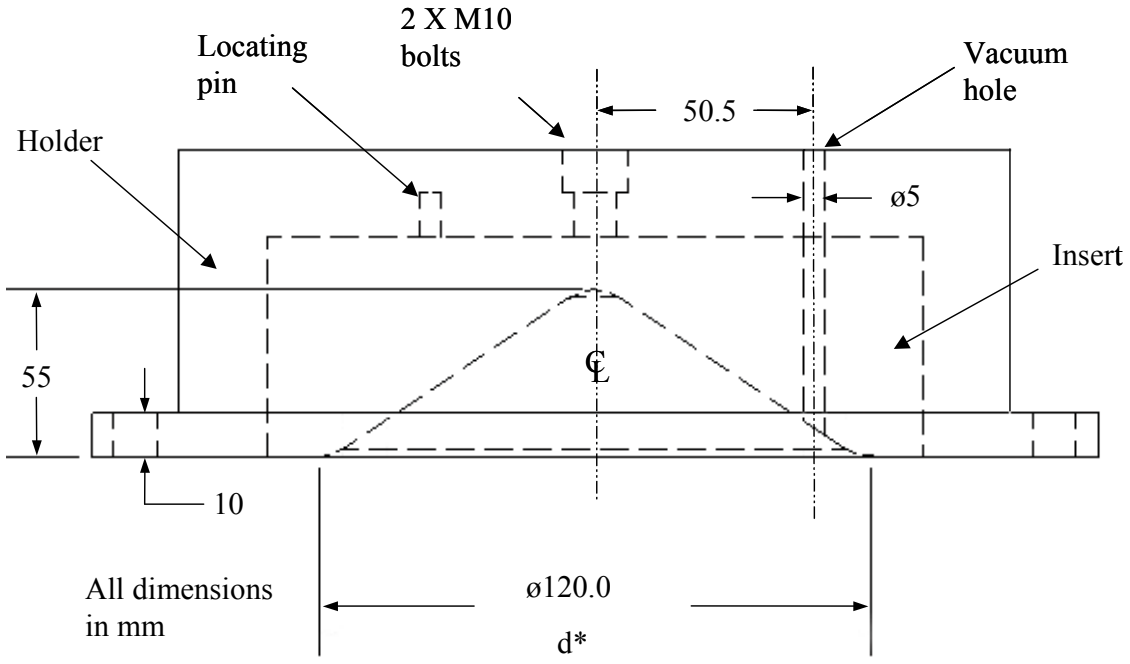

Figure 31: Tooling configuration for the 34º die. Exact height and d* dimensions are shown in Figure 30.

2.2.3 Experimental Procedure

The EM forming experiments started by placing the insulating sheet over the coil and placing the sheet metal on top of it. The die was then placed over the sheet and the nuts and bolts tightened. For the conical dies, a vacuum was drawn with a 0.5 hp vacuum pump that was kept on throughout the process. The exact pressure in the cavity was not measured. Once the sheet and die were in place the desired charge voltage was inputted into the control panel, which led to the automatic charging and discharge of the capacitor bank once the desired charge voltage was reached.

The charging voltages for each condition were determined using a trial and error calibrating procedure. For each material and die combination different charging voltages were used until the minimum voltage that produced the desired result (*e.g.* cavity fill or fractured free-formed samples) was found. Once the charging voltage had been established, three samples of each condition were formed.

2.3 Strain Measurements

The major and minor diameters of the ellipses resulting from the deformed circle grids on the sample were measured using a digital image analysis based grid measuring system connected to a computer based analysis program, with a micro-CCD camera (see Figure 32). The strains were measured by taking a digital image of the grid in question and then picking 5 points on the outside edge of the grids, from which the program calculated an ellipse. The major and minor axes of the ellipse are compared with an average of the diameter of the grids to determine the engineering strain. To determine the average original diameter, at least 5 grids are measured in an undeformed state. The final strain is the average of three measurements. The accuracy of these strain measurements has been estimated to be ± 5% strain [6].

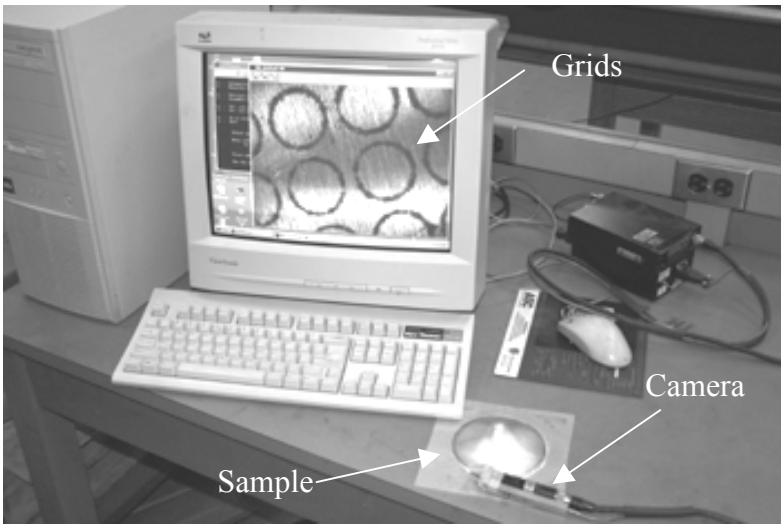

Figure 32: The grid measurement system.

Due to the abraded condition of the surface of some deformed sample parts, the grids could not be captured using the system just described. The strains of these grids were measured using an optical microscope.

2.4 Metallography

Metallographic analysis was carried out to quantify the damage present in the samples. Areas of interest from the samples were sectioned carefully to avoid additional damage and to avoid excess heating of the part. This process was accomplished by first using a band saw to cut the samples into specimens that could be handled by a precision circular saw, which was used for the final cut. The specimens were mounted with epoxy resin, to avoid any excess heating, and then wet ground using 320, 600, 1200 and 4000 grit SiC paper. Final polishing was carried out using 3 μm and 1 μm diamond paste, and 0.05 μm colloidal silica suspension.

An Olympus BH2-UMA optical microscope equipped with a Photometrics CoolSNAP CCD camera from Roper Scientific Inc [70], was used to produce eight-bit grayscale 1392 x 1040 pixel micrographs. A 20x objective lens in combination with white light was used, giving a resolution of 0.729 μm. The images obtained were analyzed using the Image-Pro Plus 4.5 software from Media Cybernetics [71]. The average percent area of voids was determined from void measurements acquired from a minimum of 15 images, corresponding to a total analyzed area of approximately 2.0 mm^2.

2.5 Fractography

Fractographs were taken using a JEOL JSM-840 [72] scanning electron microscope. The images were acquired using Oxford Instrument's INCA 3.03 software [73]. Samples were cut and cleaned in an ultrasonic bath for 5 minutes and then rinsed with alcohol prior to analysis.

CHAPTER 3

NUMERICAL MODEL

Numerical analysis was carried out using the explicit dynamic finite element code, LS-DYNA [74], which is capable of analyzing the plastic deformation and tool work-piece interactions associated with sheet metal forming. This chapter outlines how the model was created, but is not an in depth review of the code, for which the reader is referred to Hallquist [74].

3.1 Mesh

The workpiece and tooling were modeled as a blank, die and holder, as shown in Figure 33. One-eighth of the geometry was modeled, taking advantage of symmetry. An axisymetric model was not used, to facilitate future coupling with an electromagnetic code, which requires the use of solid elements. One-eight was chosen since it provided the most acceptable combination of number of elements and element geometry. The blank was held in place by applying a clamping force to the die and the holder was fixed in space.

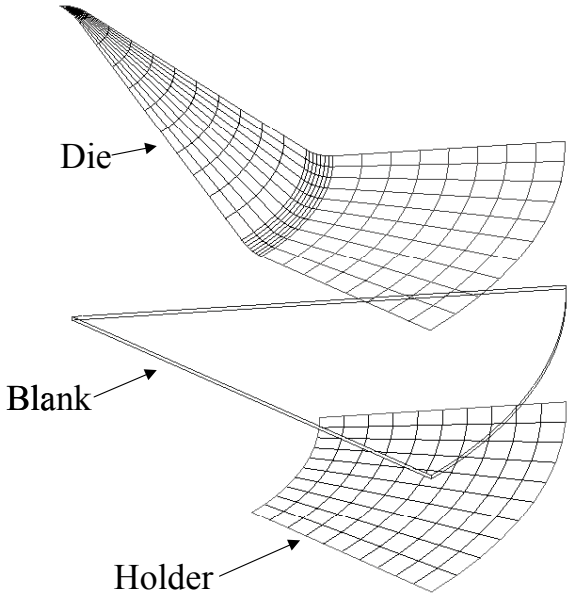

Figure 33: Exploded view of a cone (40º) model mesh. The blank elements have been omitted for clarity.

3.1.1 Blank Mesh

The blank was modeled using constant stress eight-node, brick solid elements. Figure 34 shows the blank mesh, which employed seven elements through the thickness. The coarser mesh and transition between the fine and coarse mesh are located in the area under the die that does not deform significantly. A total of 43,903 solid elements were used to model the blank. This resulted in 1,428 elements along the radius. This was the highest number of elements that could be used without producing elements of unacceptably small size and distorted geometry. The smallest element volume was 0.0024 mm^3. Seven through thickness elements were used to capture the shear stresses and to increase accuracy in future coupled simulations. Models with five elements through thickness and approximately half the number of elements were tried, but the results produced were demeaned unacceptable. Typical simulation times were 4.5 hours on a Pentium-4 2.4 GHz processor.

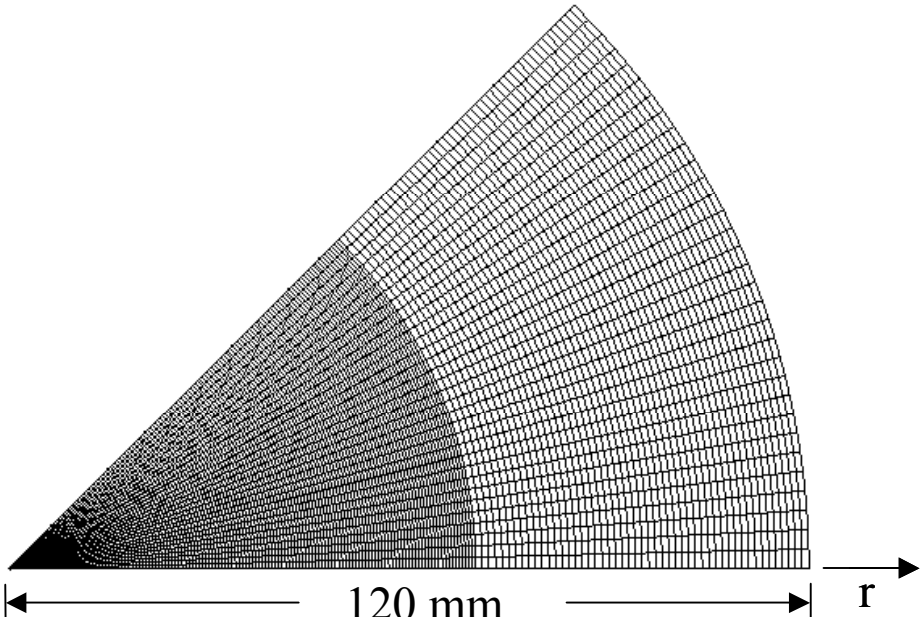

Figure 34: Top view of the blank mesh.

Due to the geometry used, the tip was an area of concern due to non-optimal element geometry (see Figure 35). This geometry resulted in minor hourglassing and an over-prediction of damage in the tip elements, which was deemed acceptable since the tip did not prove to be an area of interest in the experiments.

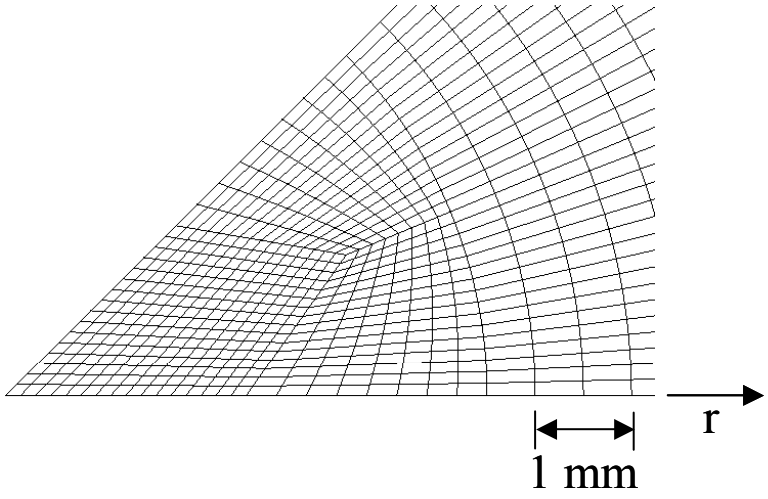

Figure 35: A close up view of the blank at the centre.

3.1.2 Tool Meshes

The dies and holder were treated as rigid bodies and only their surfaces were meshed using four-node quadrilateral elements. Since these samples were modeled as rigid bodies, the number of rigid surface elements used was the minimum required to accurately capture the geometry. The die meshes used are shown in Figure 36. The binder mesh is illustrated in Figure 33 (holder).

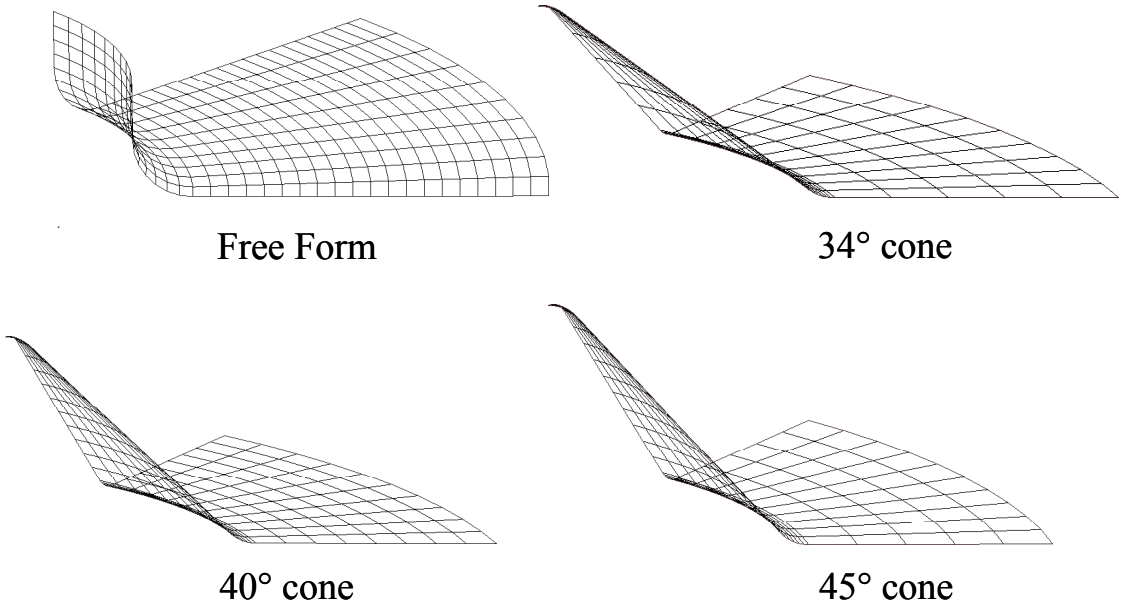

Figure 36: The die meshes used in this study meshed using four-node quadrilateral elements.

3.2 Loads and Boundary Conditions

A modified version of the analytical pressure distribution published by Al-Hassani [12] (shown in Figure 24) was used to model the pressure generated by the coil (see Figure 37). No pressure was applied to the nodes within a 5 mm radius of the centre of the blank, since a dead spot occurs at the centre. The pressure was applied as nodal forces to the nodes on the inside of the blank (the part of the blank that would be in contact with the coil). This assumes no penetration of the magnetic field into the sheet. Given the thickness of the sheet and the short time the material was exposed to the pressure pulse, this assumption was considered adequate for the purposes of this research. Forces were calculated by multiplying the pressure at the location of the node by the element area.

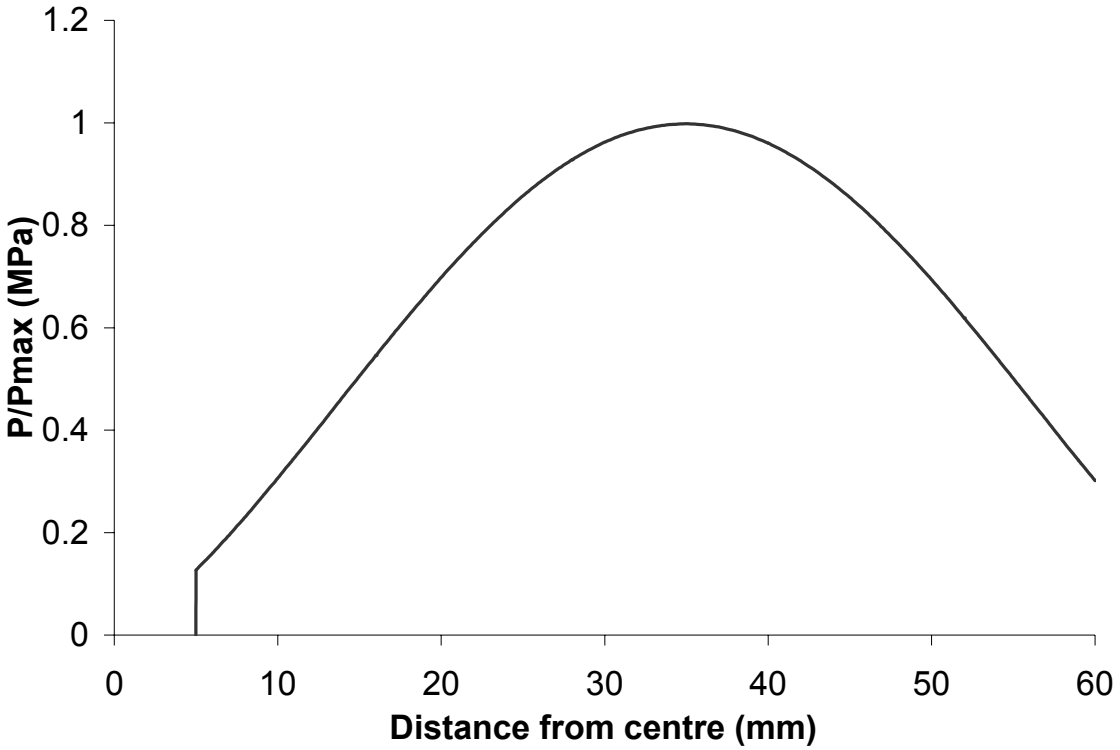

Figure 37: Radial pressure distribution used for blank loading. Taken from Al-Hassani [12].

The nodes were loaded using a sinusoidal pressure/time profile as shown in Figure 38. This is a simplification of the real time history, which would be similar to that shown in Figure 23. This approach has been proven to model the EMF process with sufficient accuracy by Oliveira [6]. Loading started at 0.11 ms, after the blank was fully clamped by the die, and ended at 0.144 ms. This time is equal to twice the average measured time to peak current of 0.017 ms.

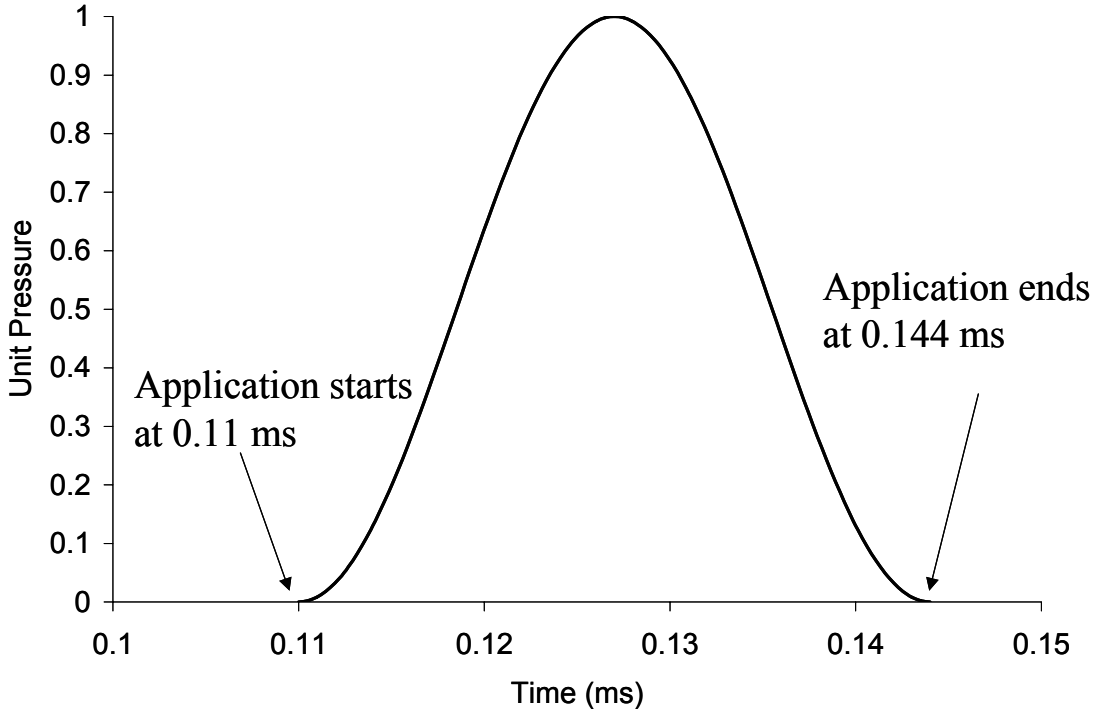

Figure 38: Pressure versus time profile used to load the nodes in the model.

No direct measurement of the pressure distributions was available from the experimental apparatus. The pressures used for the models were those that were deemed to best represent the experiments. For the free-formed cases, the pressure used for the safe models was the maximum pressure that did not produce localization, since the safe experimental samples were formed with the maximum charging voltage that did not produced necking. The pressures used for the rest of the models were the minimum ones that produced the desired result; that is, the lowest pressure that produced necking, fracture or complete die fill. The loading curves for each case are presented and discussed in 0 and compared with the experimental charge voltages.

The material was locked in place by applying a 100 kN clamping force to the die, which translates into a 800 kN force for a complete model due to the one-eight symmetry used. This force was used to prevented any blank movement during forming, thus simulating the experimental conditions where little or no movement was observed. The force was applied gradually to avoid any dynamic effects (Figure 39). The die was initially positioned 0.1 mm above the blank to minimize its travel and further reduce any dynamic effects.

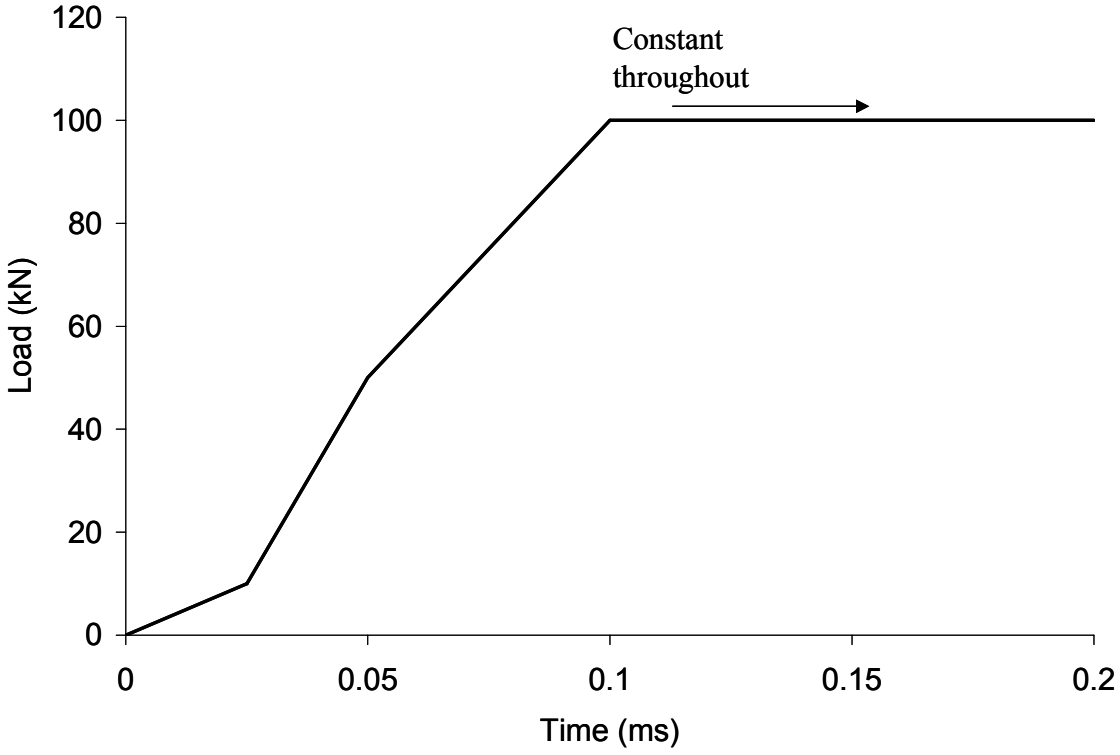

Figure 39: Clamping load application

3.3 Material Model

The constitutive model used in the present study is based on the so-called Gurson-Tvergaard-Needleman constitutive model, which consists of the Gurson yield function [75] with the modifications proposed by Tvergaard [76] and Tvergaard and Needleman [77]. This model was chosen since it provides good qualitative predictions of damage evolution and ductile fracture [78]. Damage evolution predictions were needed due to the damage suppression effects that were found during the course of the research, which will be described in detail in subsequent sections. The model results in a pressure sensitive yield function, given by:

$$\Phi = \left(\frac{\Sigma_{eq}}{\bar{\sigma}} \right)^2 + 2f^* q_1 \cosh\left(q_2 \frac{3\Sigma_{hyd}}{2\bar{\sigma}} \right) - 1 - q_3 f^{*2} = 0 \tag{3-1}$$

where, Σ_{eq} = equivalent stress, Σ_{hyd} = hydrostatic stress, $\bar{\sigma}$ = flow stress, q_1, q_2, and q_3 are calibration coefficients introduced by Tvergaard [76]. All stresses in this implementation were in megapascals. f^* is a measure of void volume fraction given by;

$$f^* = \begin{cases} f & \text{if } f \le f_c \\ f_c + \dfrac{f_u^* - f_c}{f_f - f_c}\left(f - f_c\right) & \text{if } f \ge f_c \end{cases} \tag{3-2}$$

where f = initial void volume fraction, f_c = critical value of porosity at which void coalescence starts, f_f = critical final value at which material has no more strength, and f_u^* = $1/ q_1$ = value of f^* at zero stress. For a material with zero void volume fraction, equation 3-1 reduces to the Von Mises yield function.

Void volume fraction changes as voids nucleate and grow. The rate of change of the volume fraction is given by:

$$\dot{f} = \dot{f}_{growth} + \dot{f}_{nucleation} \tag{3-3}$$

In this implementation of the model void nucleation is plastic strain controlled. The strain at which nucleation starts is called the average nucleation strain, it is one of the input parameters required by the model. Void growth and nucleation are given by the following equations [79];

$$\dot{f}_{growth} = \left(1 - f\right)\dot{\varepsilon}_{kk}^{p} \tag{3-4}$$

where, $\dot{\varepsilon}_{kk}^{p}$ is the volumetric (hydrostatic) component of plastic strain rate. For strain controlled nucleation [79]

$$\dot{f}_{nucleation} = A\dot{\bar{\varepsilon}}_p \tag{3-5}$$

where $\dot{\bar{\varepsilon}}^p$ = rate of effective plastic strain

$$A = \frac{f_n}{s_n\sqrt{2\pi}} \exp\left[-\frac{1}{2}\left(\frac{\bar{\varepsilon}^p - \varepsilon_n}{s_n} \right)^2 \right] \tag{3-6}$$

where $\overline{\varepsilon}^{p}$ = effective plastic strain, ε_n = average void nucleation strain, S_n = standard deviation of nucleation strains, and f_n = volume fraction of void nucleating particles

The model was implemented as a user defined material model in LS-DYNA, as described in detail by Worswick and Pelletier [79]. Table 2 summarizes the input parameters used for the two materials. The values for q_1, q_2, and q_3 were taken from [79]. Failure was predicted when the void volume fraction reached 5%, which resulted in the element deletion. The initial void volume fraction and second phase particles are the result of recent research performed at the University of Waterloo [80]. The rest of the values in Table 2 were the result of a parametric study, which will be described in 0.

Table 2: Summary of damage parameters used in the constitutive model in the present study.

Parameter	AA5754	AA6111
q_1	1.25	1.25
q_2	0.95	0.95
q_3	1.5625	1.5625
Initial void volume fraction (f_o)	0.00010	0.00013
Initial nucleating particle fraction (f_n)	0.0060	0.0068
Average nucleation strain (ε_n)	0.50	0.50
Critical value of porosity at which void coalescence starts (f_c)	0.016	0.016
Standard deviation of nucleation strain (s_n)	0.10	0.10
Failure void volume fraction (f_f)	0.05	0.05

The material stress-strain behaviour was modeled with a piece-wise linear plasticity curve with yield strengths of 98.0 and 135.0 MPa for AA5754 and AA6111 respectively [20]. The flow stress curves used are shown on Figure 25. An isotropic hardening response was used. No high strain rate data was used since none was available for the materials studied. Recent work by Smerd *et al.* [22] with AA5754 and AA5182, has shown that the constitutive rate sensitivity is small.

CHAPTER 4

EXPERIMENTAL RESULTS

This chapter presents results from the experiments, including observations of the deformed sample geometry, strains and formability data, metallographic analysis and finally the results of SEM fractographic analysis. In this work, deformed samples were classified as safe or failed. Safe parts were those that showed no evidence to the naked eye of necking or fracture, while samples that showed any evidence of necking or fracture were considered to have failed. Table 3 and Table 4 present the samples used for the experiments, their heights and the measurements made from them. Samples used for calibration purposes are not included.

Table 3: AA 5754 samples used for the experimental program. S=strain measurements, H= height measurements and M=microscopy (optical and SEM).

Sample Number	Charging Voltage (kV)	Condition	Height (mm)	Use
Free form				
5754-7	5.8	Safe	31.7	S, H, M
5754-8	5.8	Safe	30.2	S, H
5754-9	5.8	Safe	33.5	S, H
Free form necked				
5754-4	6.5	Necked	37.3	S, H, M
5754-5	6.5	Necked	38.0	S, H
5754-6	6.5	Necked	38.7	S, H
34º cone				
2506-5754-02	8.0	Safe	N/A	M
2506-5754-03	8.0	Safe	38.6	S, H
2506-5754-04	8.0	Safe	38.7	S, H
2506-5754-05	8.0	Safe	38.7	S, H
40º cone				
14-57-40-2	8.0	Safe	46.3	S, H, M
14-57-40-8	8.0	Safe	47.3	S, H
14-57-40-9	8.0	Safe	47.0	S, H
45º cone				
14-57-45-2	9.0	Fractured/Necked	54.6	S, H, M
14-57-45-5	9.0	Fractured/Necked	54.5	S, H
14-57-45-6	9.0	Fractured/Necked	53.9	S, H

Table 4: AA 6111 samples used for the experimental program. S=strain measurements, H= height measurements and M=microscopy (optical and SEM).

Sample Number	Charging Voltage (kV)	Condition	Height (mm)	Use
Free form				
14-61-ff-1	5.0	Safe	29.02	S, H, M
14-61-ff-2	5.0	Safe	29.04	S, H
14-61-ff-3	5.0	Safe	27.06	S, H
Free form necked				
07-61-01	5.2	Necked	31.28	S, H
07-61-02	5.2	Necked	31.92	S, H
07-61-03	5.2	Necked	N/A	S, H, M
07-61-04	5.2	Necked	31.94	S, M
34º cone				
07-61-05	7.0	Safe/Buckled	N/A	S, H, M
07-61-06	7.0	Safe/Buckled	35.74	S, H
07-61-09	7.0	Safe/Buckled	36.12	S, H
40º cone				
14-61-40-02	9.0	Safe/Buckled	45.04	S, H
14-61-40-03	9.0	Safe/Buckled	44.8	S, H, M
14-61-40-04	9.0	Safe/Buckled	45.0	S, H
45º cone				
14-61-45-05	10.0	Fractured/Buckled	52.9	S, H
14-61-45-06	10.0	Fractured/Buckled	50.1	S, H, M
14-61-45-07	10.0	Fractured/Buckled	48.3	S, H

4.1 Deformed Geometry

Free-formed samples of both alloys had a characteristic shape, as shown in Figure 40. This distinctive shape is the result of the deformation history produced by the EMF process, which will be discussed in more detail in 0. The regions marked on the figure will be used to describe the samples henceforth. Area A, was where the maximum strains were recorded and where some samples necked and eventually failed. The charge voltages used, as well as the average of the final measured height of the samples, based on three samples, are presented in Table 5.

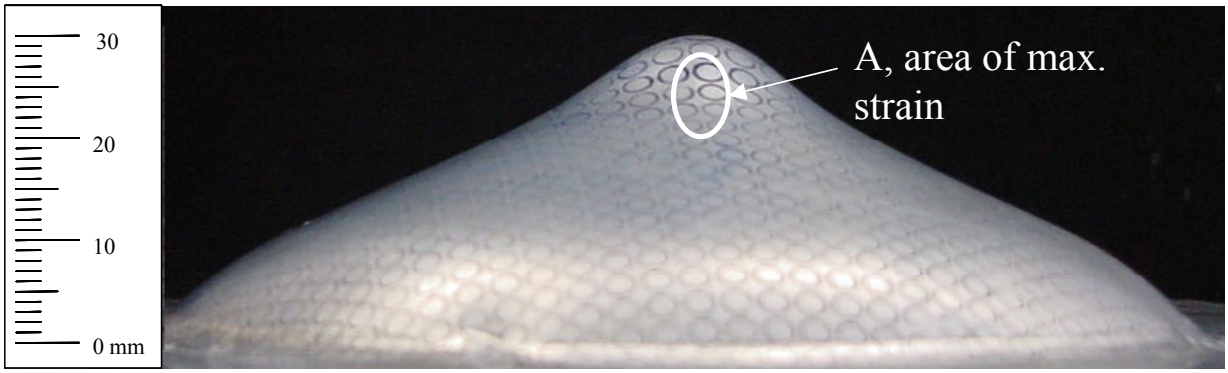

Figure 40: Typical AA5754 free-formed sample (5.8 kV).

Table 5: Summary of forming voltage and average sample heights. Fractured samples were those with complete separation of the tip. * Only two samples measured.

Sample	Charging Voltage (kV)	Average Sample Height (mm)	Tool Height (mm)
AA 5754			
Free form	5.8	31.8	N/A
Necked free form	6.5	38.1	N/A
Fractured free form	7.7	N/A	N/A
34º Cone	8.0	38.7	38.0
40º Cone	8.0	46.9	47.3
45º Cone	9.0	54.4	55.9
AA 6111			
Free form	5.0	28.0	N/A
Necked free form	5.2	31.7	N/A
Fractured free form	6.0	N/A	N/A
34º Cone	7.0	35.9*	38.0
40º Cone	9.0	44.9	47.3
45º Cone	10.0	50.4	55.9

.

At certain charging voltages, the samples failed at region A as shown in Figure 41. Both alloys exhibited the same general location and geometry of failure, with differences in the failure mode, which will be discussed in the metallography and fractography sections. Multiple necks were observed in both materials. Further increases in voltage resulted in failure shifting to the base of the sample (see Figure 42), producing a blanking type of operation. This catastrophic type of failure was not studied in detail in the present study.

Figure 41: Free-formed AA5754 failed sample (7.7 kV).

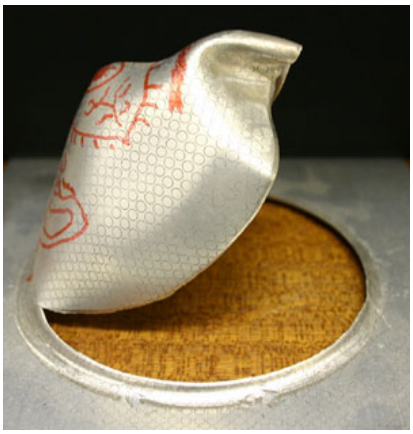

Figure 42: Blanking failure mode of free-formed AA 5754 sheet (8.0 kV).

Photographs of AA5754 samples formed into the conical dies are shown in Figure 43 to Figure 45. All samples have distinctive geometric discontinuities, referred henceforth as steps, at different locations relative to the base, depending on the die used. Samples formed with the 40 and 45º cones exhibited an area of burnishing near the tip, where the greatest strains were recorded and where fracture occurred in the 45º samples. The burnishing was not uniform throughout the samples, being present only in one quadrant of the sample. This is likely due to the non-uniform pressure distribution produced by the spiral coil.

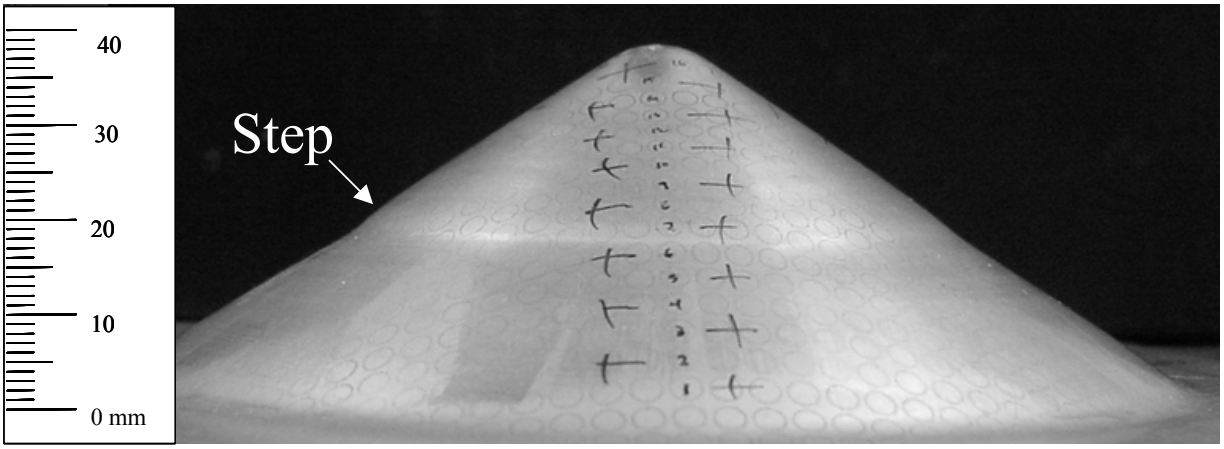

Figure 43: AA5754 sheet formed with 34º cone (8.0 kV).

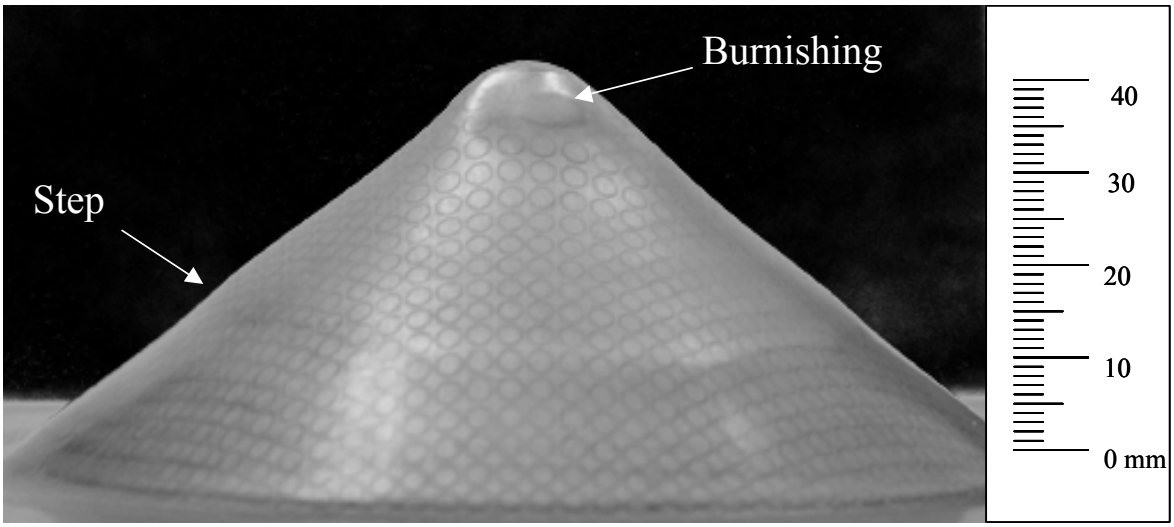

Figure 44: AA5754 sheet formed with the 40º cone (8.0 kV).

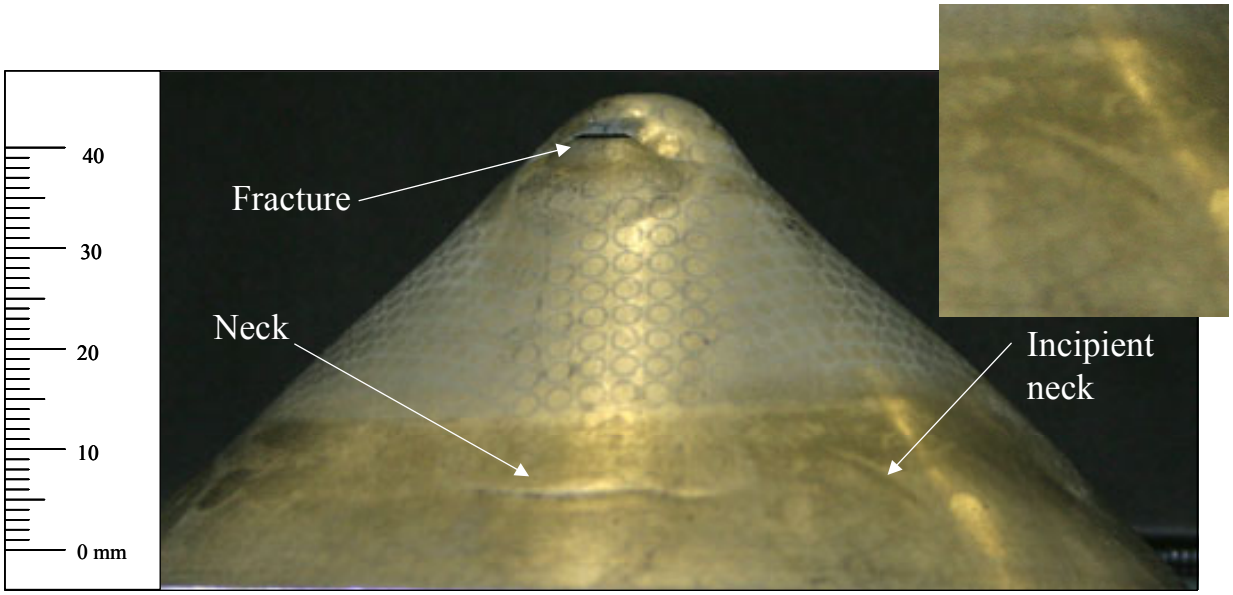

Figure 45: AA5754 sheet formed with the 45º cone (9.0 kV)**.**

Samples formed into the 40 and 45º cones buckled in the area of the vacuum hole as shown in Figure 46. This buckling is attributed to a weakness caused by the lack of support at the vacuum hole.

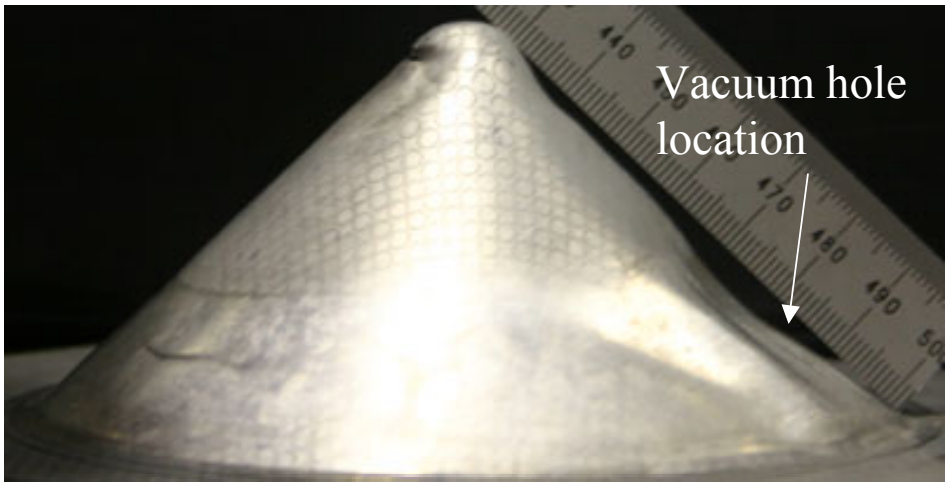

Figure 46: Buckling near the vacuum hole in a AA5754 sheet sample formed into the 45º cone.

Photographs of formed AA6111 samples are shown in Figure 47 to Figure 50. As can be seen from Figure 47, the free-formed samples exhibited the same distinctive shape as the

AA5754 samples. Steps similar to the ones present in AA5754 can be observed. The AA6111 samples differed from the AA5754 ones in three significant ways; they exhibited a different buckling mode, the lack of burnishing near the tip and visibly different fracture modes. Buckling occurred apparently independently from the vacuum hole and, contrary to the AA5754 cones, appeared in the 34º cones (Figure 48). Buckling in the AA6111 40 and 45º cones was different than that observed in the AA5754 cones. The former exhibited a more uniform and consistent buckling pattern, which could be the result of material anisotropy; whereas, the buckling in the AA5754 samples was clearly associated with the vacuum hole.

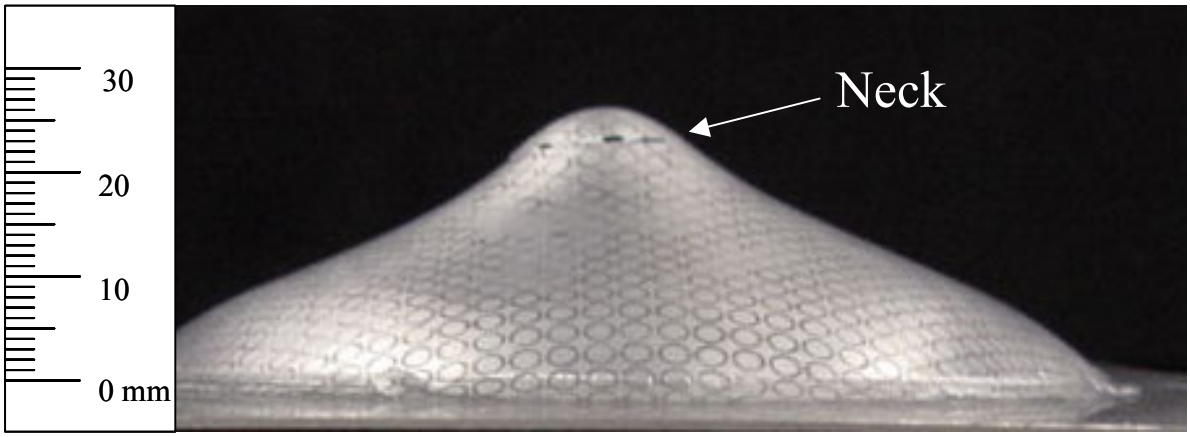

Figure 47: AA6111 free-formed sample (5.2 kV)

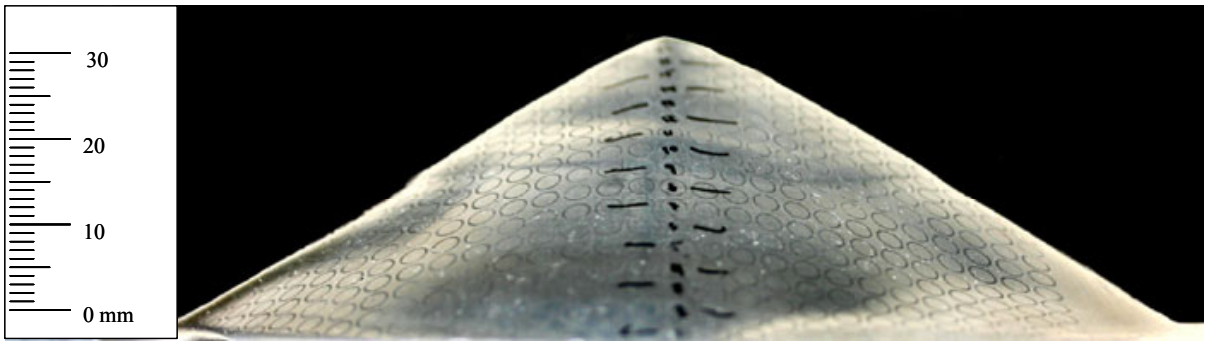

Figure 48: AA6111 sheet formed with the 34º cone (7.0 kV).

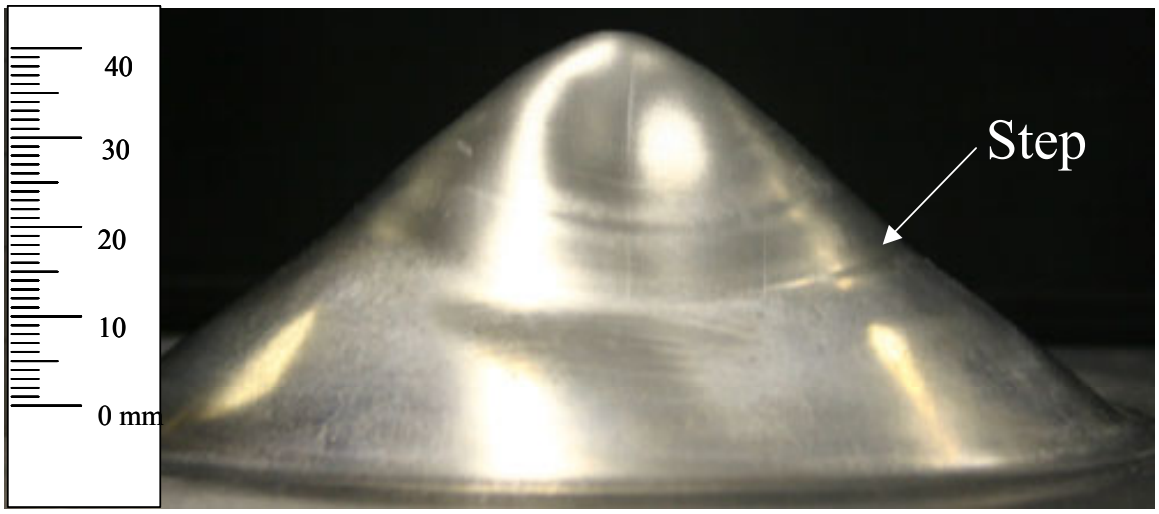

Figure 49: AA6111 sheet formed with the 40º cone (9.0 kV).

The lack of burnishing near the tip of the AA6111 specimens was likely related to the buckling, which could be preventing the material from properly filling the die. The buckling could result in non-uniform contact with the die, or in a lack of contact of the sheet with the die during the final stages of forming. Which mechanism, if any, of the two is taking place, could not be determined with the available experimental apparatus.

Two fracture modes were present in the AA6111 samples formed into the 45º cones, a "saw tooth" fracture with little evidence of necking below the step (see Figure 50) and what to the naked eye appears to be a tearing type of fracture in the buckled area of the tip (see Figure 51). These failures are in contrast to the fractures observed in the AA5754 samples that appear to be the result of localization and necking. All of these fractures will be discussed in detail in Sections 4.3 and 4.4.

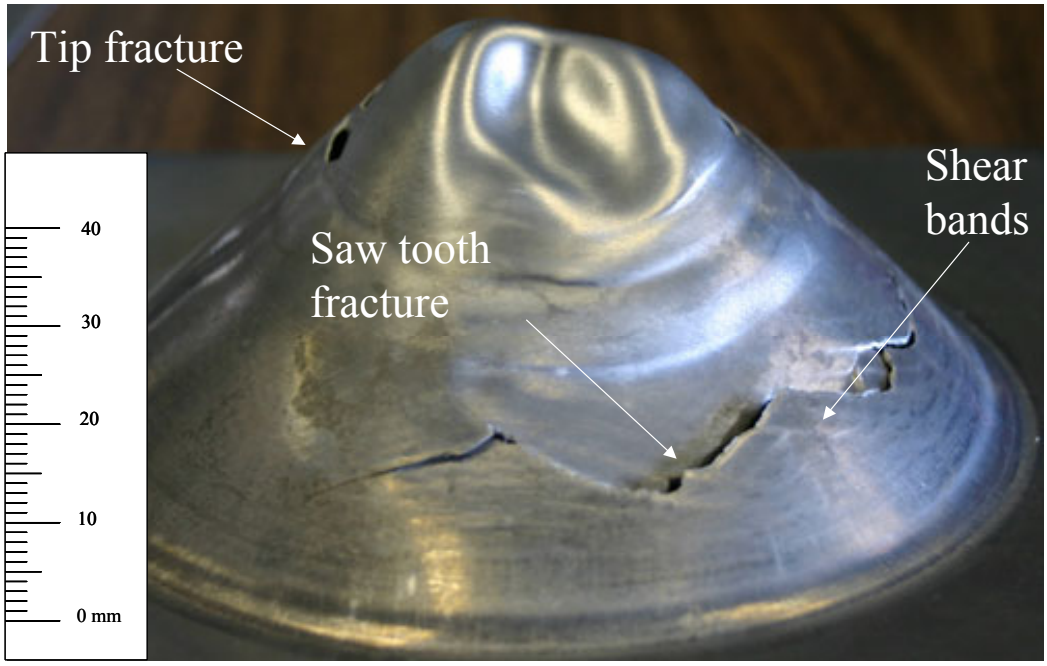

Figure 50: AA6111 sheet formed with the 45º cone (10.0 kV).

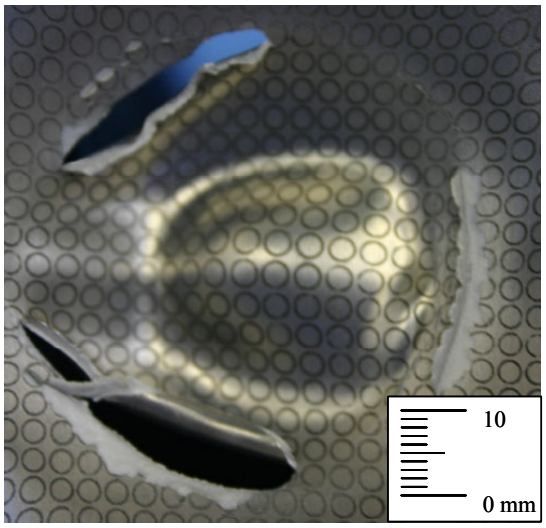

Figure 51: Typical tip fracture for AA6111 sheet formed with the 45º cone.

None of the conical samples conformed exactly to the die into which they were formed. The step and the buckling were the most obvious imperfections. As can be seen in Table 5, the cones are not the same height as the dies, with the AA5754 samples reaching a height closer to the die than the AA6111 samples. In the case of the AA6111 samples, the discrepancy in height is due to the buckling. For the AA5754 samples the reason for the difference in height

appears to be a "rebound effect" that has been reported previously [59], which consists of the sheet bouncing away from the die after contact is made. The rebound effect also contributes to the formation of the step. This behaviour was predicted by the numerical analysis and will be further discussed in the next chapter.

For both materials, the specimens formed into the 45º cones had significantly different degrees of surface abrasion between the areas above and below the step, as can be readily seen from the figures. The area below the step suffered more abrasion than the area above the step. Two possible explanations are that the material was not contacting the die after the step uniformly or that more sliding occurs along the die surface below the step. This could not be confirmed with the current apparatus, but should be considered in future work.

4.2 Formability Data

Formability data for free-formed and 34º, 40º and 45º die-formed cones is presented using a standard forming limit diagram (FLD) format. The FLD is a formability measure used in the sheet-metal forming industry that assumes quasi-static and plane stress conditions; the reader is referred to reference [81] for an in-depth description and analysis of forming limit diagrams. The EMF process is neither quasi-static nor plane stress (as will be shown in the next chapter), but the data is nevertheless compared to standard FLDs to provide a comparison of the limit strains achieved in the two processes, EMF versus stamping. In the present study, major versus minor engineering strains were plotted to facilitate comparison with standard quasi-static data. The strains were measured along a line oriented in the rolling direction. Radial distributions of strain are also presented to show the distribution of the strains within the samples. Three samples were measured for each condition.

Measured strains for the free-formed AA5754 and AA6111 samples are presented in Figure 52 and Figure 53 along with conventional FLDs for the respective materials. The AA5754 samples showed safe measured strains above the FLD in only one region, area B (see Figure 40). This region is where the samples consistently localized and eventually fractured and only a minor increase in formability compared to the quasi-static FLD can be observed. For the AA6111 there were no specimens with "safe" strains above the FLD. In fact, the AA6111 samples exhibited failure strains below the conventional FLD. The lower formability may be due to age-hardening of the material [82]. Due to logistical difficulties, the AA6111

used in the present experiments was stored for approximately nine months before the EMF experiments were performed.

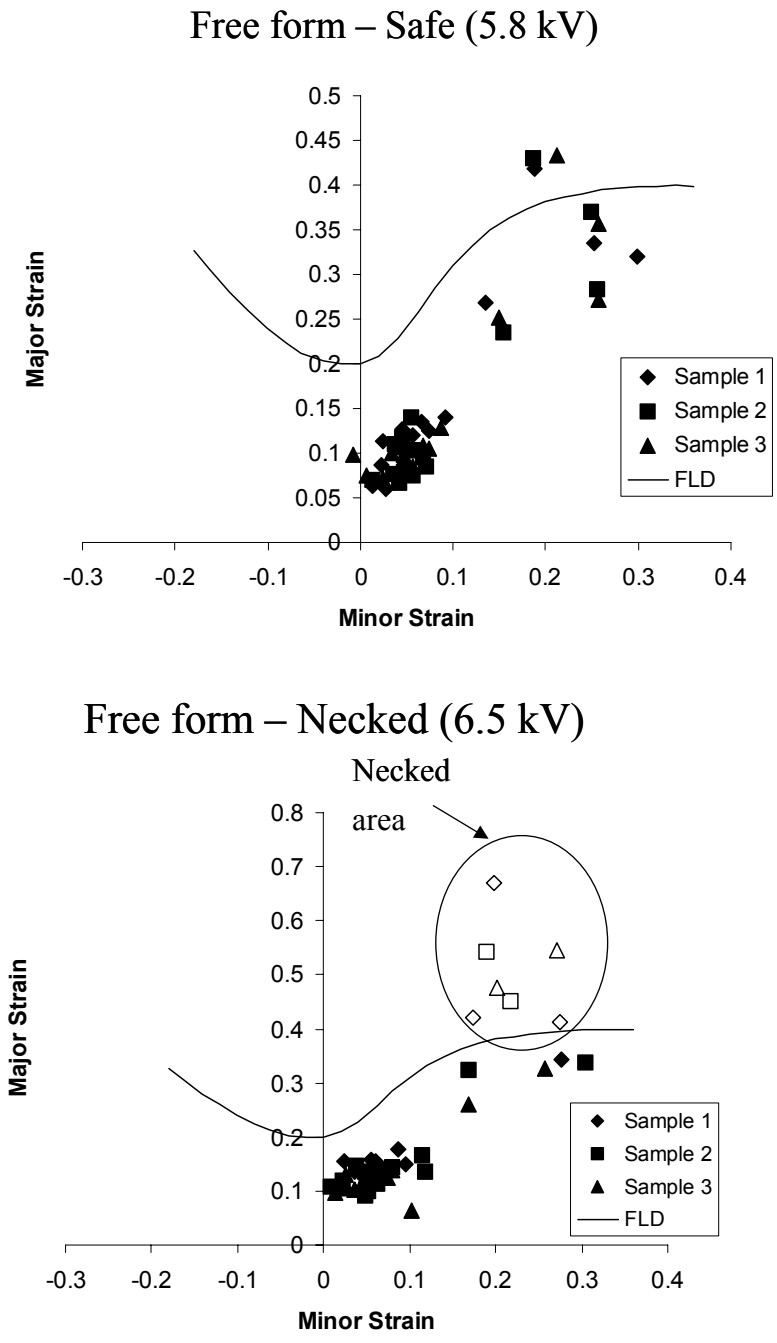

Figure 52: Formability data for free-formed AA5754 samples. The curve is a conventional FLD curve for the material [20]. Open symbols indicated measurements in the neck area.

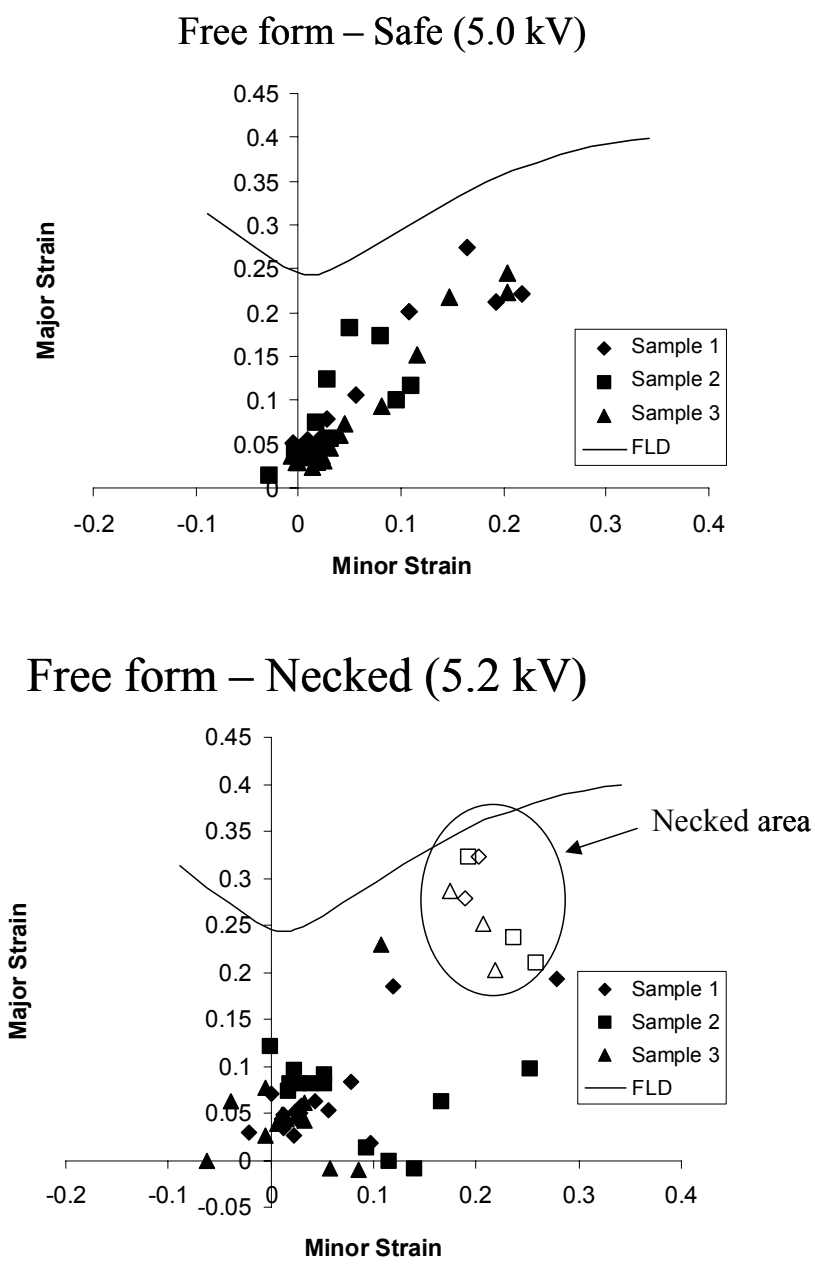

Figure 53: Formability data for free-formed AA6111 samples. The curve is a conventional FLD curve for the material [20]. Open symbols indicated measurements in the neck area.

Figure 54 and Figure 55 show the forming limit diagram results for the AA5754 and AA6111 samples formed into the different conical dies. In contrast to the free form cases, safe strains above those of the conventional FLD were observed for all of the conical samples. The AA6111 specimens formed with the 34 º die showed strains only slightly above the FLD.

Despite the ageing that may have occurred, the AA6111 samples showed increased formability when compared to the FLD.

In the free-formed cases, any increase in formability would necessarily come from inertial or high strain rate effects; the lack of any significant increases in the current free-formed samples indicates that these effects are not playing an important role. Therefore, the difference in formability of the free-formed and conical samples is attributed to the interaction between the sheet and the tool. Since strains higher than those observed for the conventional FLD were recorded in the conical samples, it is concluded that the tool/sheet interaction has a significant effect on formability.

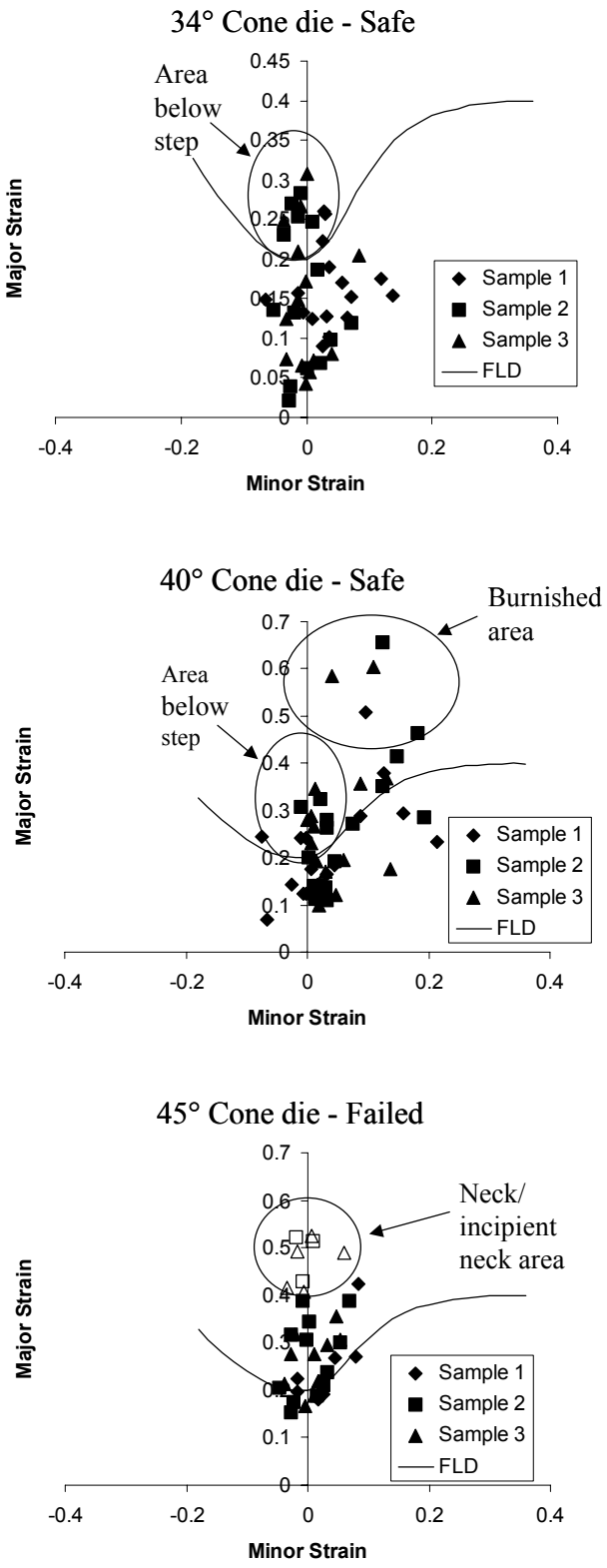

Figure 54: Formability data for the AA5754 conical samples. Open symbols indicated measurements in the neck area.

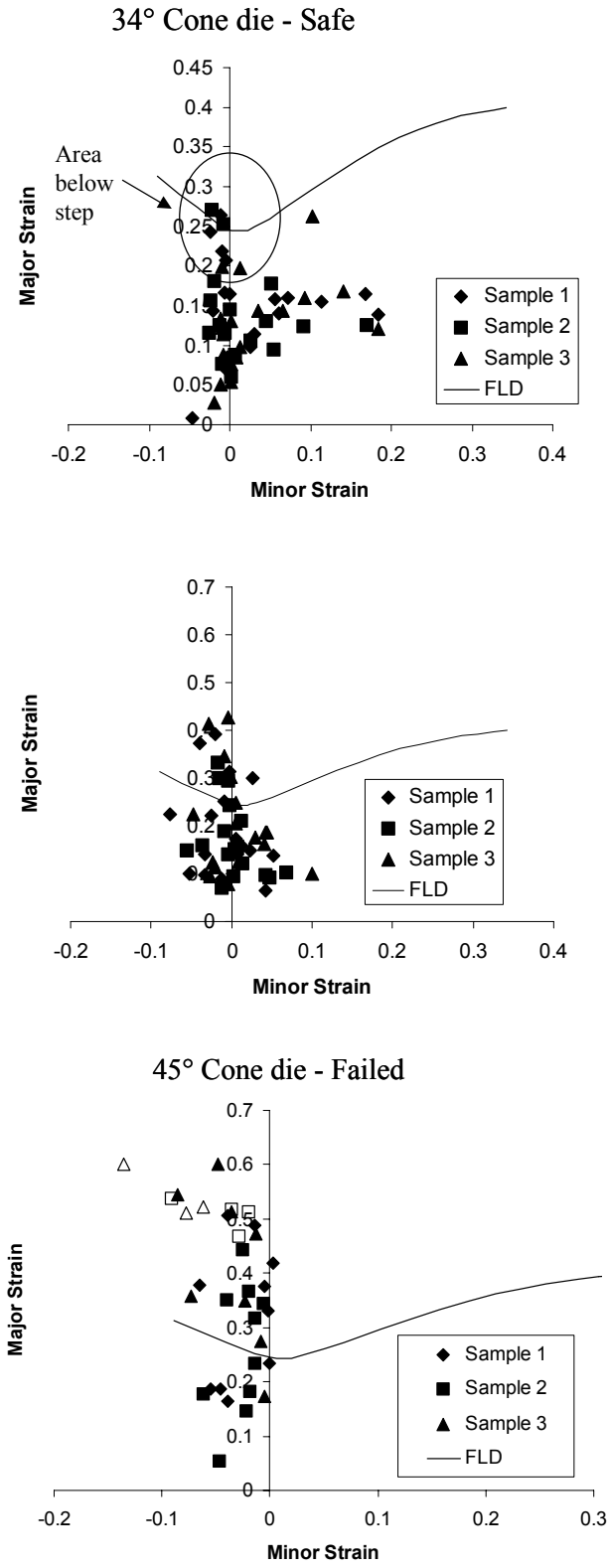

Figure 55: Formability data for the AA6111 conical samples.

The burnished tip area of the AA5754 samples presented significantly elevated strains, as can be seen in Figure 54. In the case of the specimens formed in the 40º die, the strains were more biaxial in nature than the other measured strains. The burnished area was not present at the tip of the AA6111 samples, likely due to the samples not fully filling the die.

To show the strain distributions within the samples, the measured strains for each grid from tip to base along the rolling direction are plotted. Major and minor strains are again plotted for consistency; they correspond to the radial and hoop directions respectively in the samples, as defined in Figure 56. As can be seen Figure 57 to Figure 60 the radial distributions of strains for the free-formed AA5754 and AA6111 samples show the same trends. The largest strains were recorded in the area just below the tip (area B). In the AA5754 samples, safe strains in this area were slightly above the conventional FLD. In contrast, the strains measured from the AA6111 samples were all below the FLD.

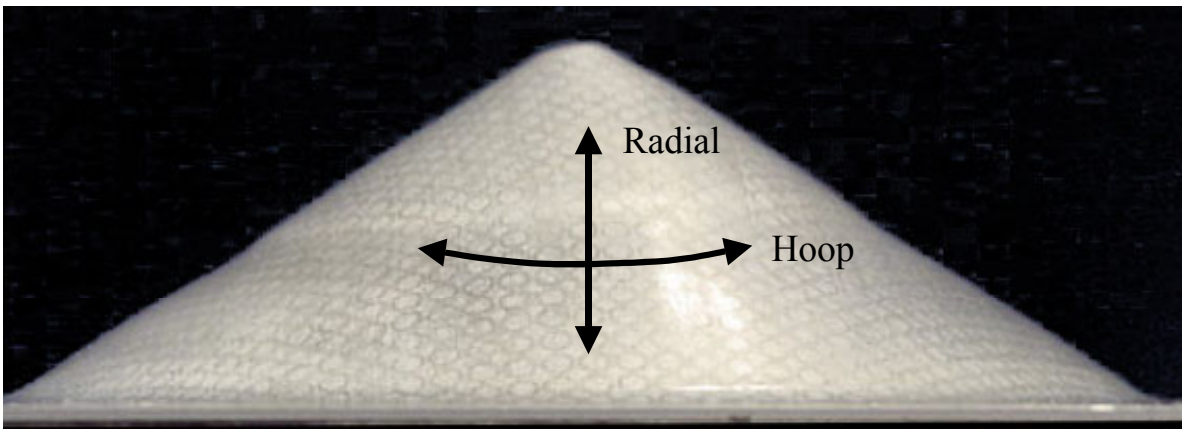

Figure 56: Photograph illustrating what will be called from now on the radial and hoop directions of the samples.

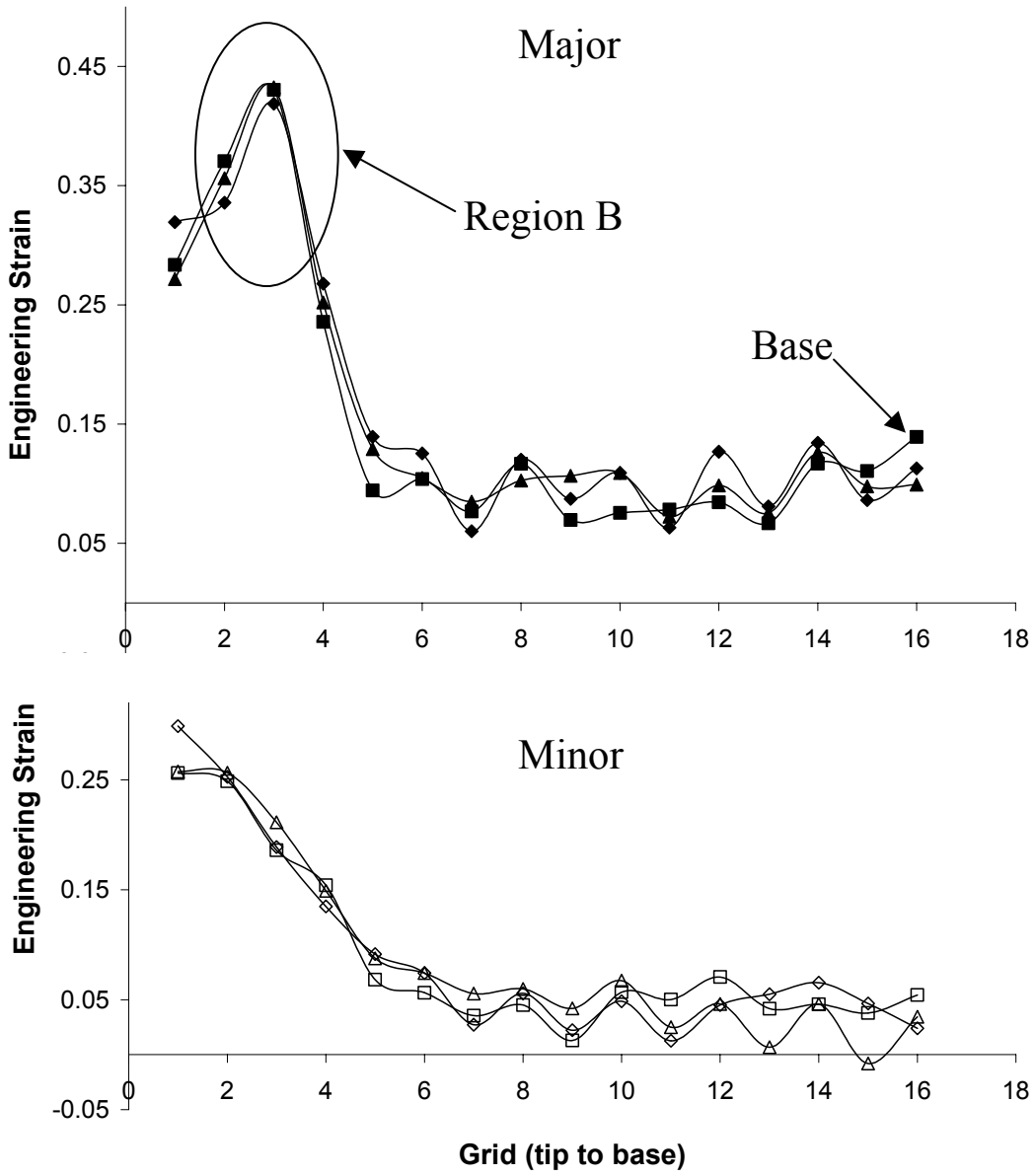

Figure 57: Radial distribution of strains for AA5754 safe (5.8 kV) free-formed samples. Solid symbols represent major strain and open ones represent minor strain. Sample 1=■, sample 2=▲ and Sample 3=♦.

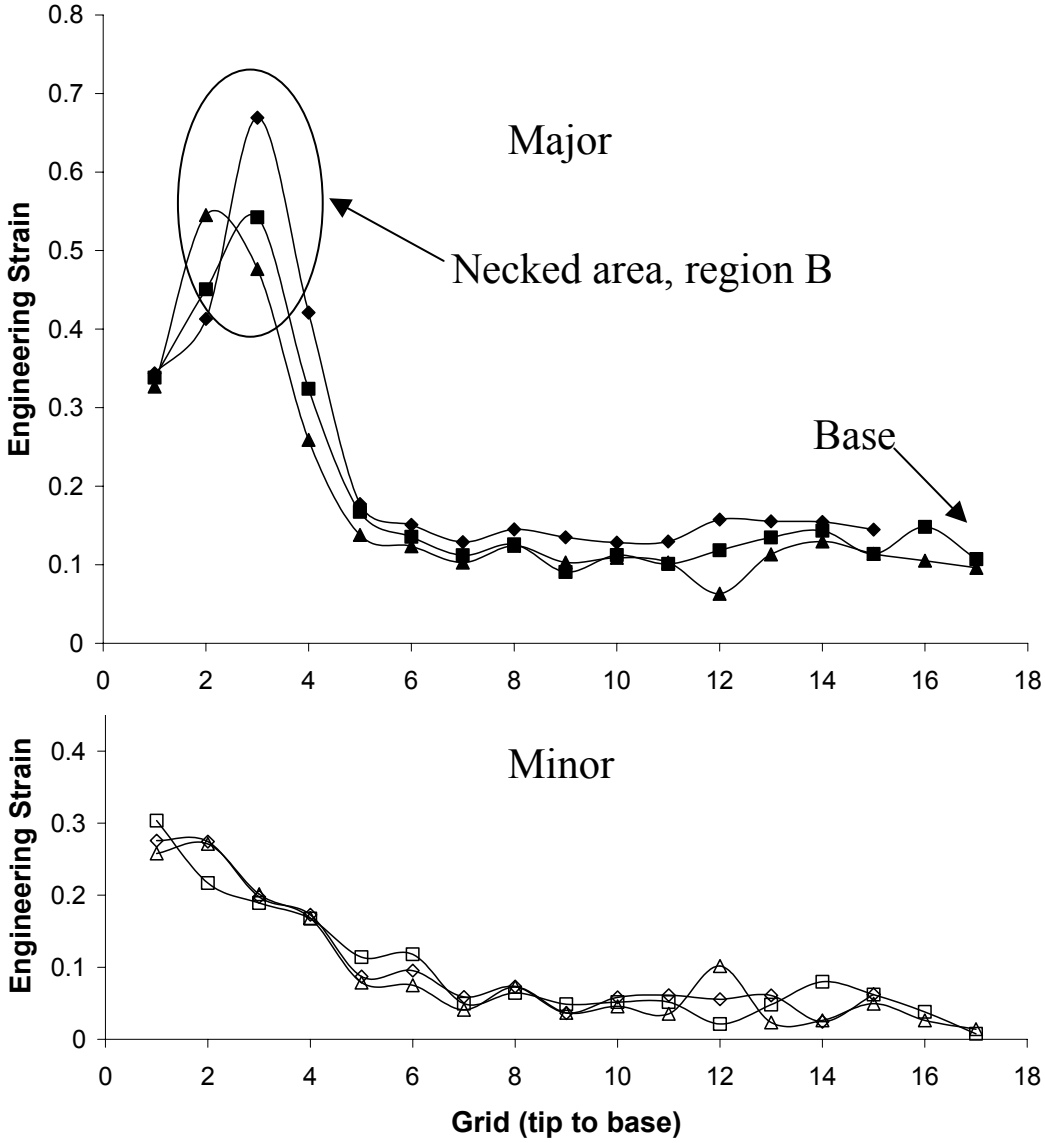

Figure 58: Radial distribution of strains for AA5754 necked (6.5 kV) free-formed samples. Solid symbols represent major strain and open ones represent minor strain. Sample 1=■, sample 2=▲ and Sample 3=♦.

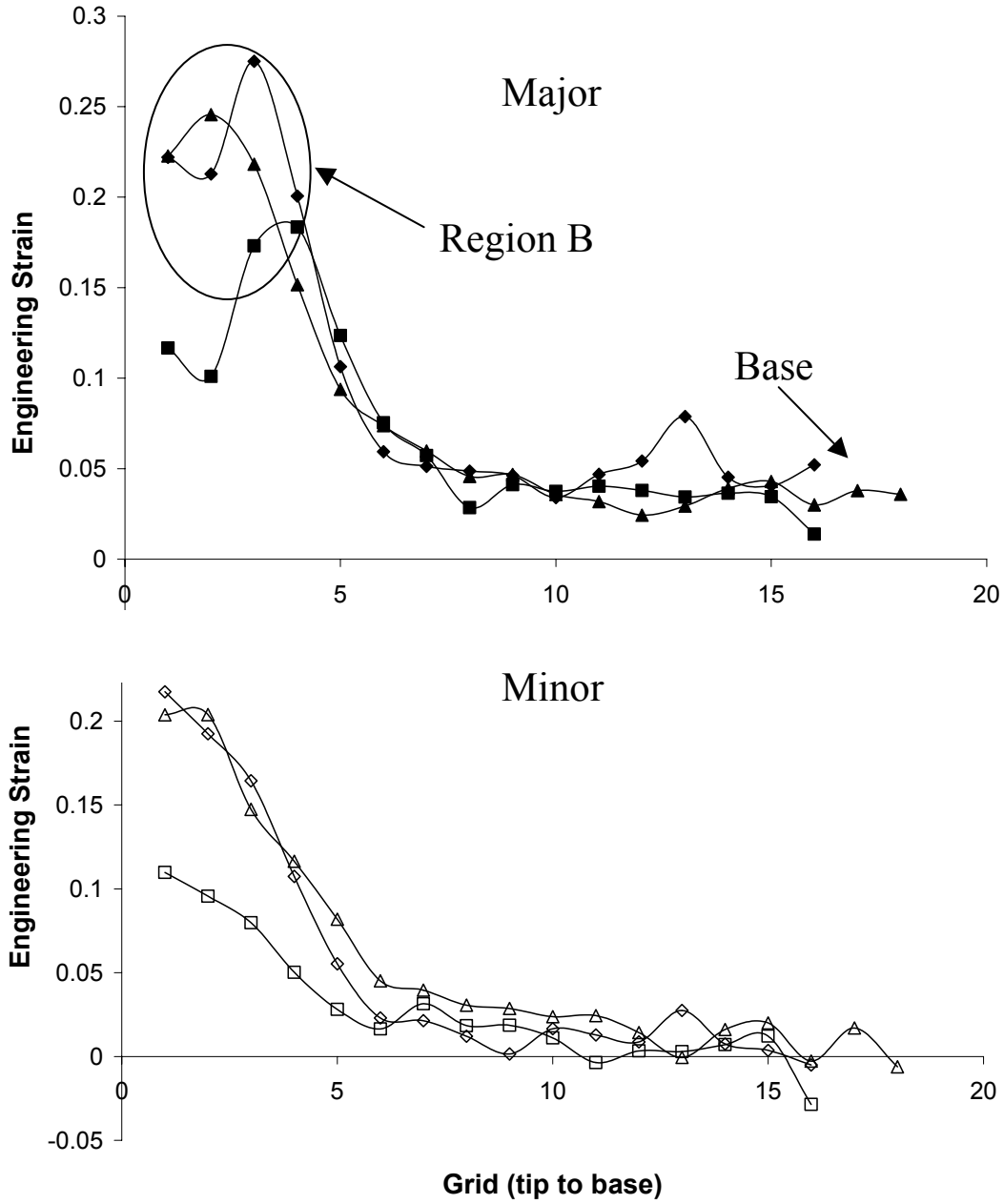

Figure 59: Radial distribution of strains for AA6111 safe free-formed samples (5.0 kV). Solid symbols represent major strain and open ones represent minor strain. Sample 1=■, sample 2=▲ and Sample 3=♦.

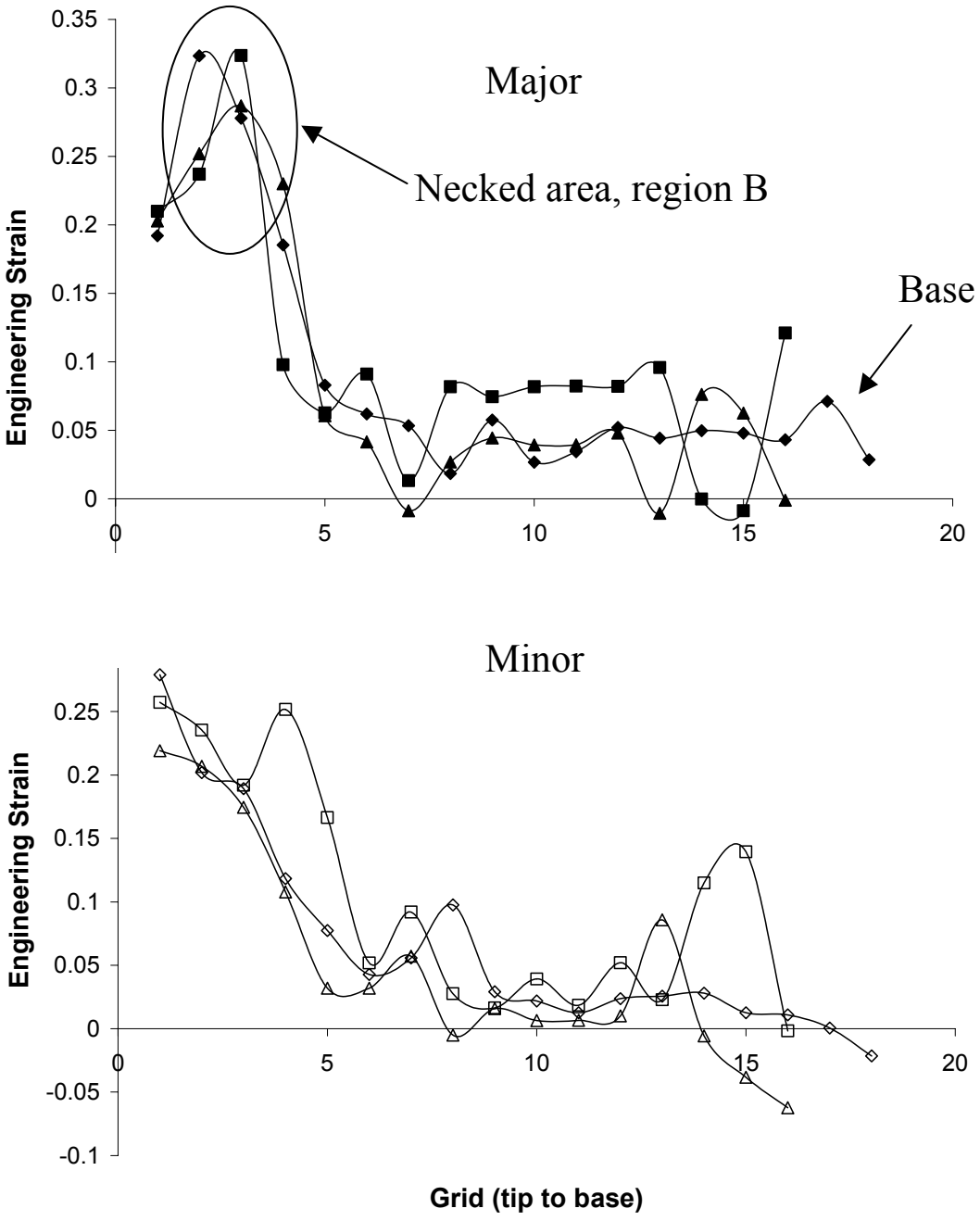

Figure 60: Radial distribution of strains for AA 6111failed (5.2 kV) free-formed samples. Solid symbols represent major strain and open ones represent minor strain. Sample 1=■, sample 2=▲ and Sample 3=♦.

Figure 61 to Figure 66 show the radial distributions of strain measured for the conical samples. The maximum strains were recorded in the area of the step, except in the samples with burnishing near the tip where the maximum strains occurred in the burnished area. It can

be seen from the figures that the strains in the area of the step correspond to near-plane strain conditions, while those in the impacted area at the tip are more biaxial in nature. Grids in the area above the step of the AA6111 samples formed into the 45º die could not be measured due to the abraded condition of the surface of the samples. For this region, the gird number in Figure 66 corresponds to the location just above the step, in contrast to the data from the other samples.

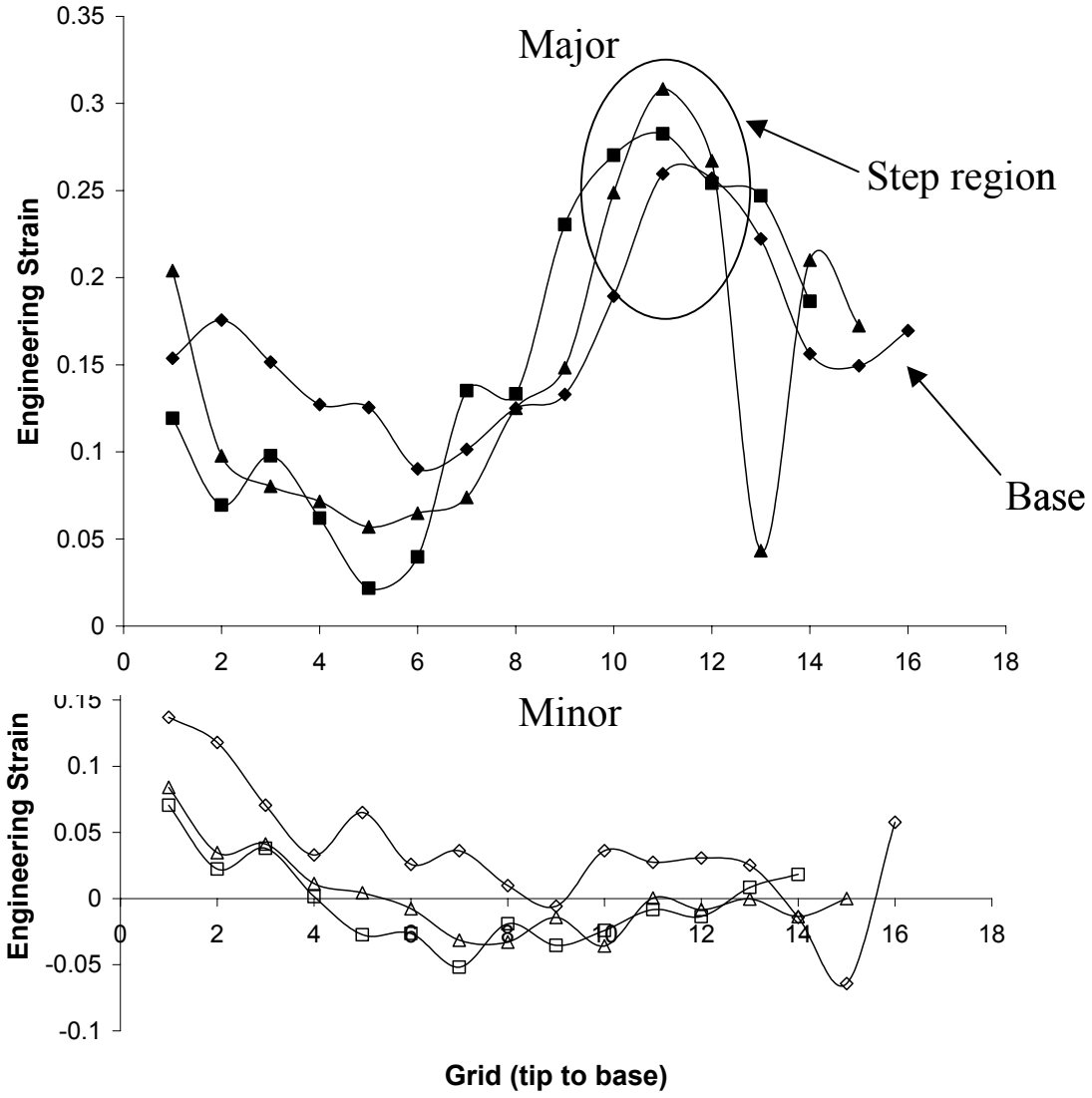

Figure 61: Radial distribution of strains for AA5754 34º samples. Solid symbols represent major strain and open ones represent minor strain. Sample 1=■, sample 2=▲ and Sample 3=♦.

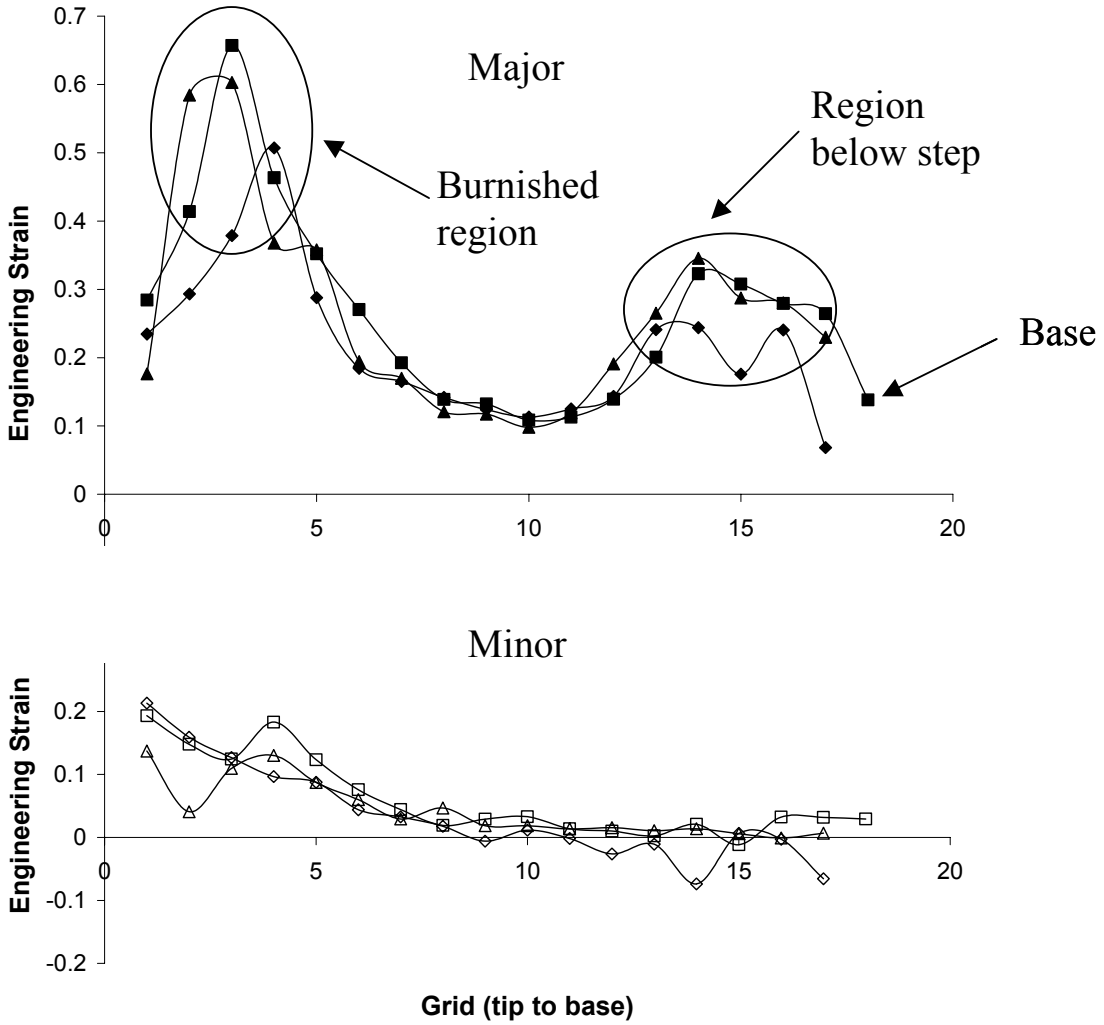

Figure 62: Radial distribution of strains for AA5754 40º samples. Solid symbols represent major strain and open ones represent minor strain. Sample 1=■, sample 2=▲ and Sample 3=♦.

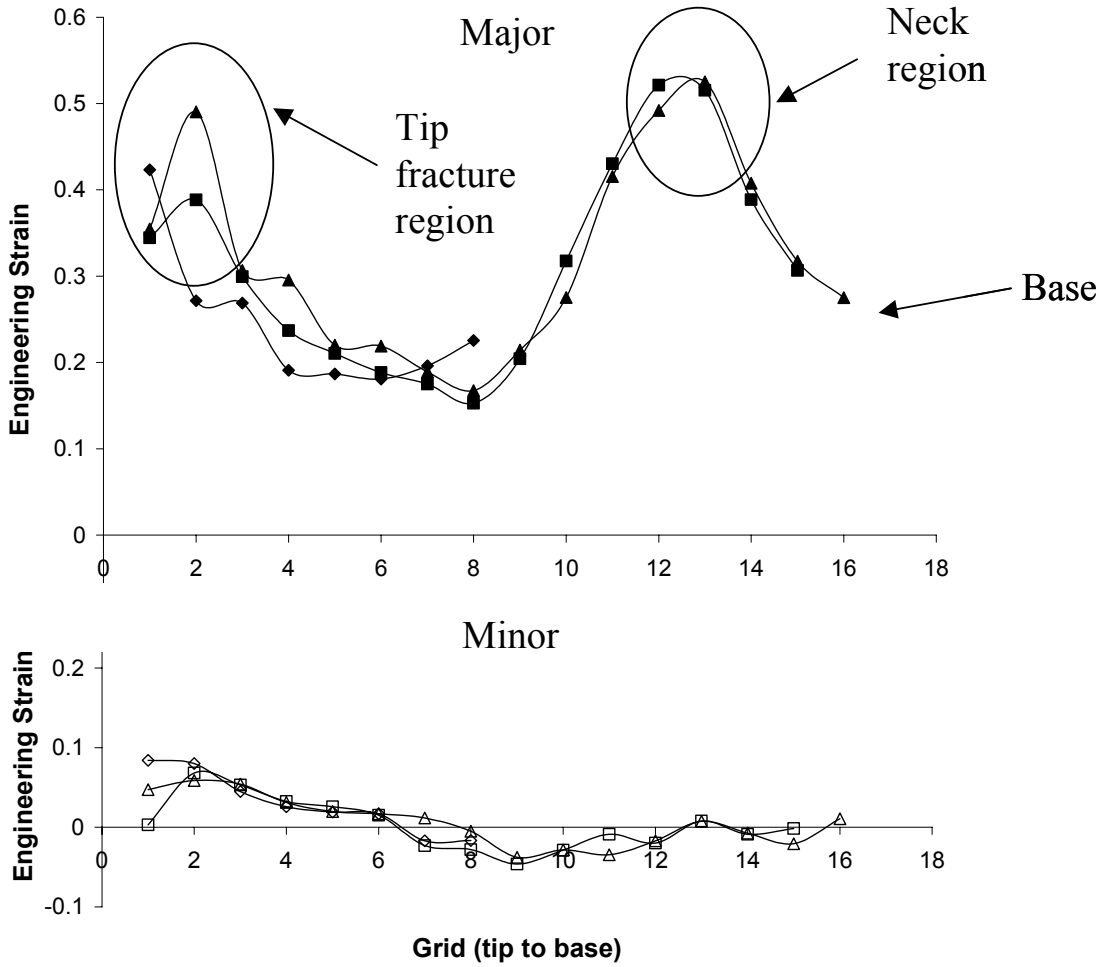

Figure 63: Radial distribution of strains for AA5754 45º samples. Solid symbols represent major strain and open ones represent minor strain. Sample 1=■, sample 2=▲ and Sample 3=♦.

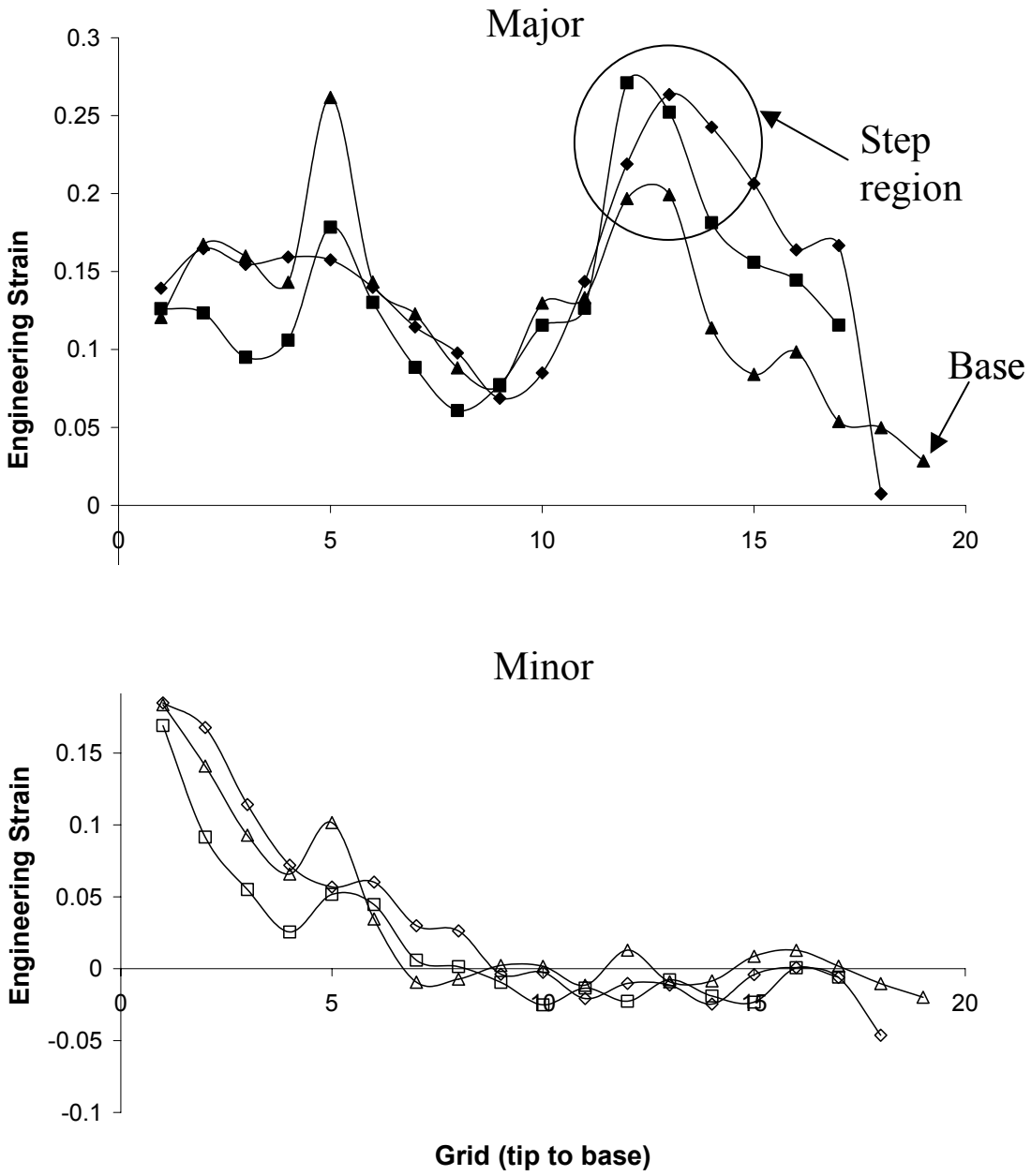

Figure 64: Radial distribution of strains for AA6111 34º samples. Solid symbols represent major strain and open ones represent minor strain. Sample 1=■, sample 2=▲ and Sample 3=♦.

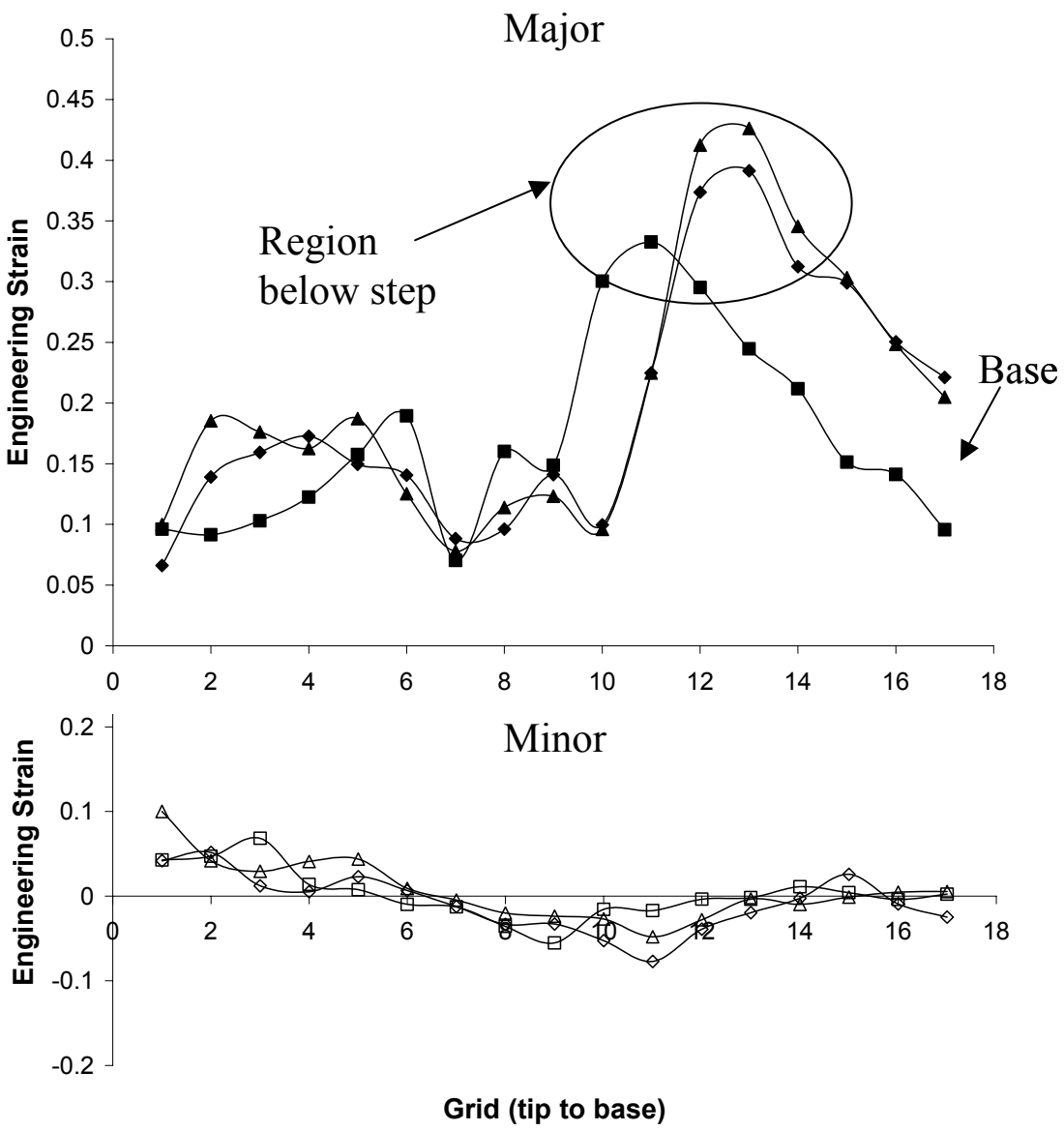

Figure 65: Radial distribution of strains for AA6111 40º samples. Solid symbols represent major strain and open ones represent minor strain. Sample 1=■, sample 2=▲ and Sample 3=♦.

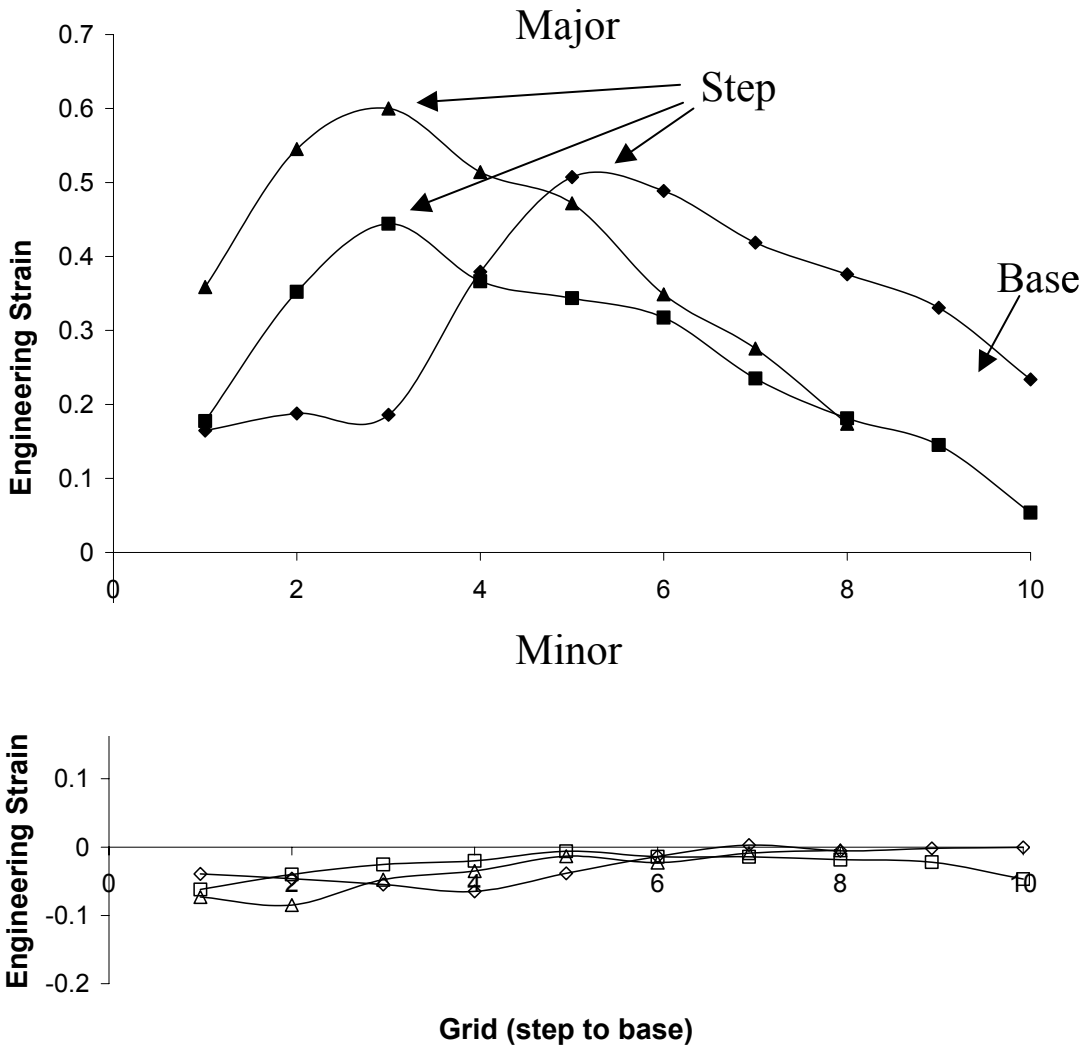

Figure 66: Radial distribution of strains for AA6111 45º samples. Measurements could only be taken from the step to the base due to the condition of the sample. Solid symbols represent major strain and open ones represent minor strain. Sample 1=■, sample 2=▲ and Sample 3=♦.

4.3 Microscopy and Damage Results

The formability data presented in the previous section shows a definite increase in formability of the material when it is formed into a die using EMF. In contrast, no significant increases in formability were observed in free-formed samples, in fact, the strains within the free-formed AA6111 samples lay below the FLD (see Figure 52 and Figure 53). To gain more insight into the reasons for the increased formability in the in-die operation and the role played by the tool/sheet interaction metallographic and fractograhic analysis were performed. This

section presents the micrographs and damage measurements obtained from the metallographic analysis.

To quantify the damage present in the formed samples, metallographic analysis was performed as described in 0. Data was gathered from the areas of interest of the samples. For the free-formed samples, these areas were the area of maximum strain (area B Figure 40), where the necks formed, and for the cone samples, the areas of the step, the impact region below the tip and the necks below the steps. The tip area of the 34º cones was not analyzed since no significant deformation or other features were observed there. Only one section of one sample for each condition was studied, due to the time consuming nature of the metallographic measurement process. Table 6 and Table 7 show the data for the AA5754 and AA6111 samples, respectively. Since the step was significantly narrower than the circle grids used to measure strain, the strain values presented are an average of the values for the grids immediately above and below the step. Figure 67 and Figure 68 show the locations where the damage measurements were taken.

Table 6: Summary of damage data for the AA5754 samples. S= safe, N= necked. * see Figure 68. + Due to the abraded condition of the grids of the sample where the damage was measured, strain values are an average of the strains in the region for the other two samples.

	Location	**Porosity area fraction (%)**	**Strain % (radial/hoop)**	**Condition**
SAFE FREE-FORMED SAMPLE				
	Area B	0.03	42/19	S
NECKED FREE-FORMED SAMPLE				
	Area B	0.15	67/20	N
34º CONE				
	Below step	0.004	13/3	S
	Step	0.05	11/5	S
	Above step	0.01	9/3	S
40º CONE				
	Below step	0.015	26/1	S
	Step	0.021	22/1	S
	Above step	0.011	19/2	S
	Tip	0.067	60/11	S
45º CONE+				
	Below step	0.025	51/-2	S
	Step	0.042	36/-3	S
	Above step	0.018	30/-3	S
	Neck*	0.22	52/-1	N

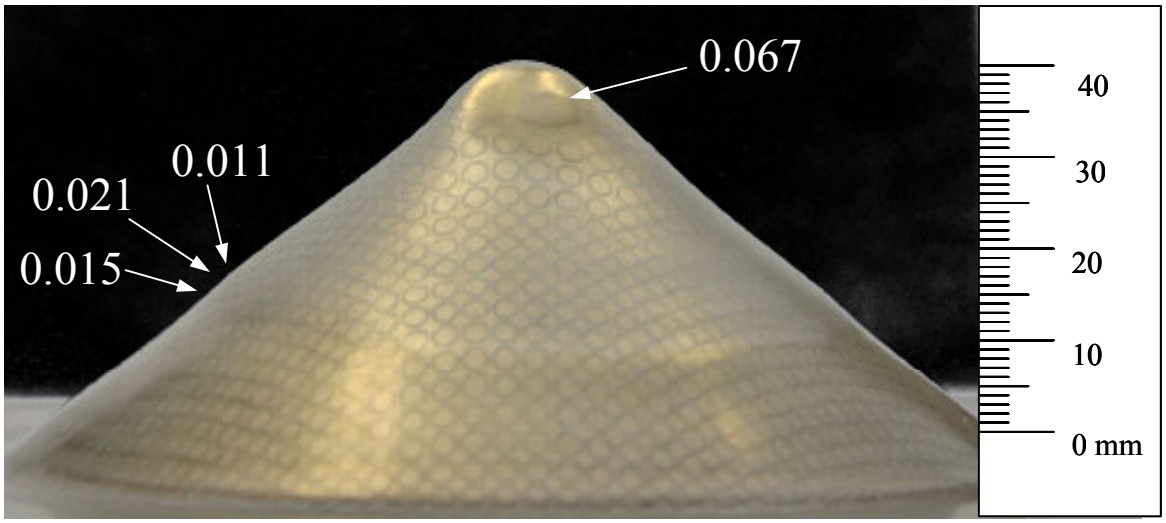

Figure 67: Measured porosity area fraction (%) for an AA5754 40º cone.

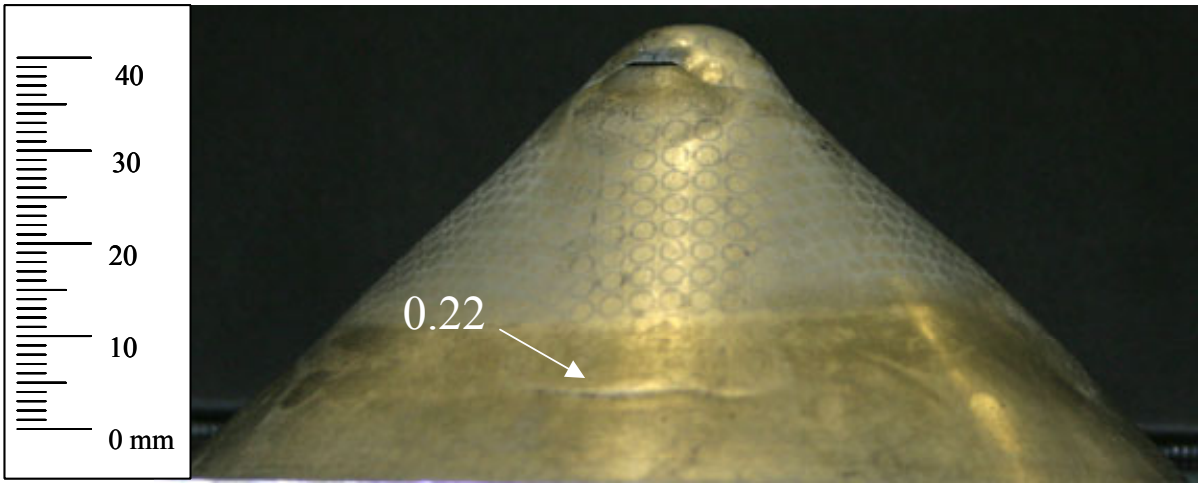

Figure 68: Measured porosity area fraction (%) for the neck of an AA5754 45º cone.

All the AA5754 conical samples follow the same trend, with the maximum damage occurring at the burnished area near the tip and at the step. The only exceptions were the necks, which had the most damage, as expected.

The data for the AA6111 samples (see Table 7) shows similar trends, with some differences due to the different failure modes observed. Higher damage values than those

observed in AA5754 were recorded, which is consistent with the higher concentration of second phase particles present in AA6111 (0.68% void volume fraction for AA6111 compared to 0.60% for AA5754 [80]). The localized region of the free-formed samples did not show the same increase in damage as was present in the AA 5754, due to the reduced amount of thinning of the AA6111 necks when compared to the necks in AA 5754; these differences in thinning will be shown in detail below. The conical samples showed the same trends as the AA5754 conical samples, except for the 45º cone, which showed a more uniform distribution of damage across the step. This is probably due to the presence of the cross-hatch necks that lead to the saw tooth fracture (see Figure 50), these localized areas could contribute to the damage to the step area. Another interesting phenomenon is the difference in damage between the area of the saw tooth fracture and the tip fractures (see Figure 51). The fractures in the tip area occurred with significantly less damage than those on the side.

Table 7: Summary of damage data for the AA6111 samples. S= safe, N= necked. * see Figure 70. $^{+}$ Average value for region of fracture.

	Location	**Porosity area fraction (%)**	**Strain (radial/ hoop)**	**Condition**
SAFE FREE-FORMED SAMPLE				
	Area B	0.036	28/16	S
NECKED FREE-FORMED SAMPLE				
	Area B	0.069	29/18	N
34º CONE				
	Below step	0.22	14/-2	S
	Step	0.084	18/-2	S
	Above step	0.025	26/-1	S
40º CONE				
	Below step	0.037	30/-2	S
	Step	0.081	22/-4	S
	Above step	0.05	15/-6	S
	Tip	0.14	12/-1	S
45º CONE				
	Below step	0.078	44/-3	S
	Step	0.073	27/-5	S
	Above step	0.083	18/-6	S
	Tip*	0.065	N/A	F
	Side*	0.32	36/-2^{+}	F

.

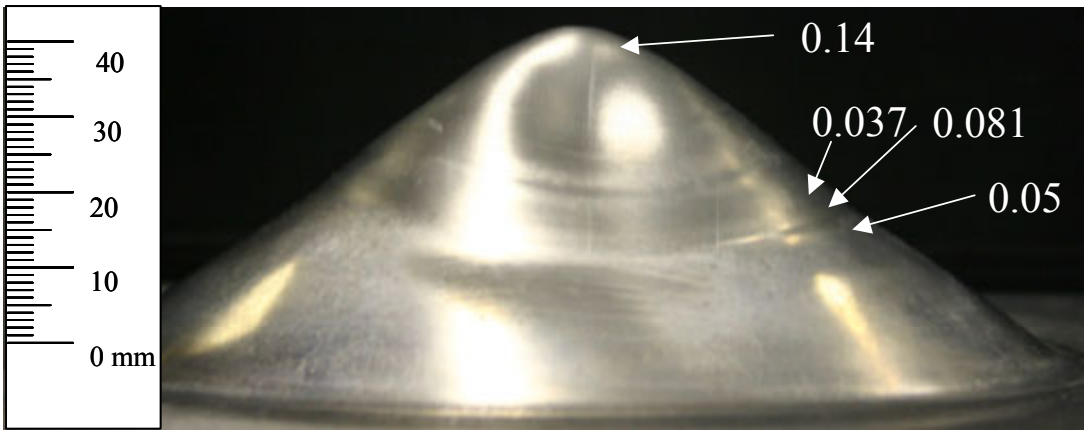

Figure 69: Measured porosity area fraction (%) for an AA6111 40º cone.

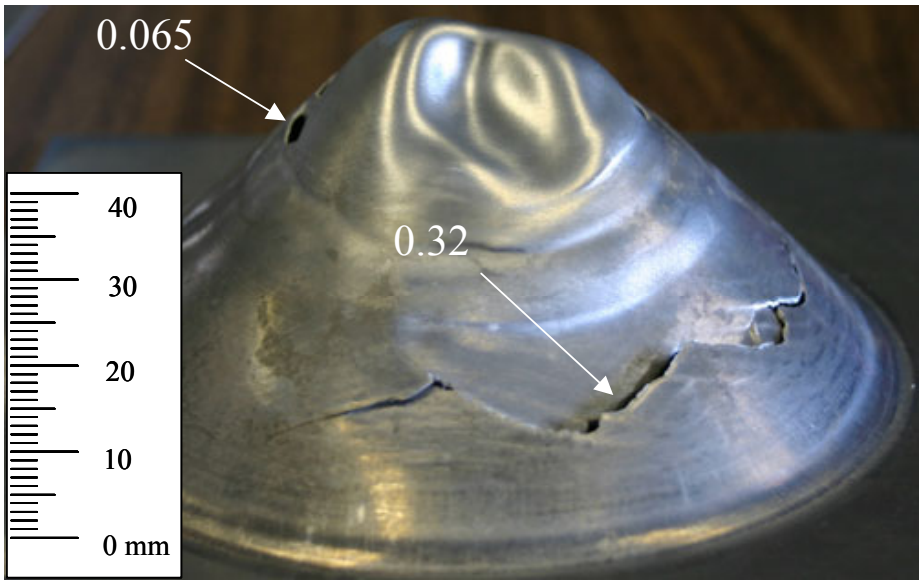

Figure 70: Measured porosity area fraction (%) near the two types of fracture of AA6111 45º cones.

Damage in both materials resulted from a combination of de-cohesion and particle cracking of the second phase particles. The second phase particles are intermetallic compounds composed of Iron and Manganese for AA5754 [80] and Iron and Silicon for AA6111, the later being Iron rich. Figure 71 and Figure 72 show typical damage observed in the samples. The larger fraction of second phase particles present in AA6111 is evident in the figures. Note that the voids do not seem to grow uniformly, but rather in the radial direction.

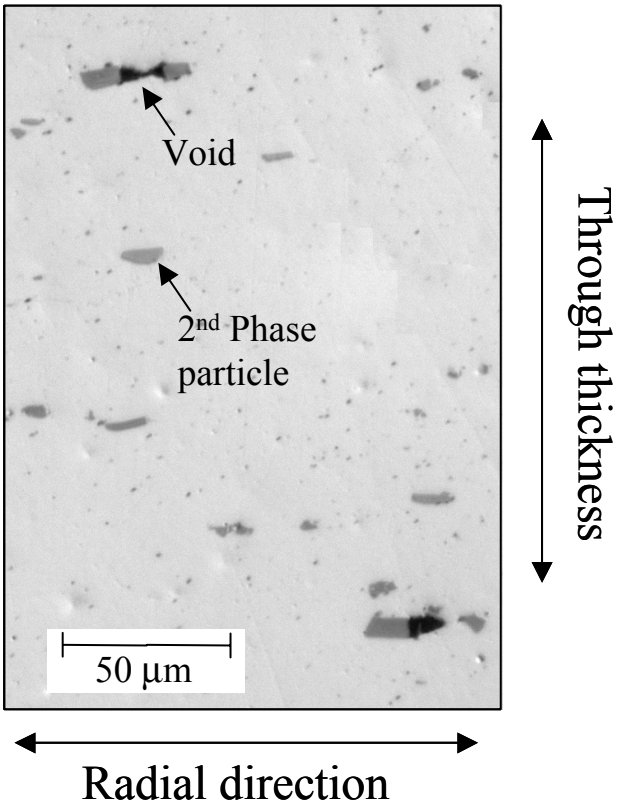

Figure 71: Typical damage and second phase particles present in AA5754 samples. Image in this figure comes from the step area of a 34º cone.

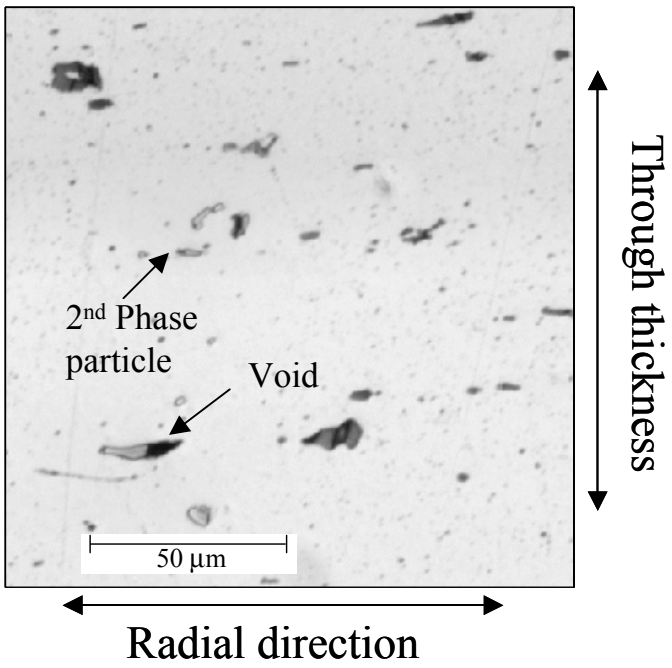

Figure 72: Typical damage and second phase particles present in AA6111 samples. Image in this figure comes from the step area of a 40º cone specimed.

Despite the two materials showing similar damage trends, the necking and failure was different for the alloys studied. The differences were evident in both the free-formed and conical samples. Figure 73 shows micrographs of the necks in the AA5754 and AA6111 free-formed samples. It is evident that AA5754 thins considerably more than the AA 6111 samples prior to fracture. The neck in the AA6111 is also more diffuse than that for AA 5754. Both samples were formed with a charging voltage just under that needed to cause fracture to produce the maximum amount of thinning possible.

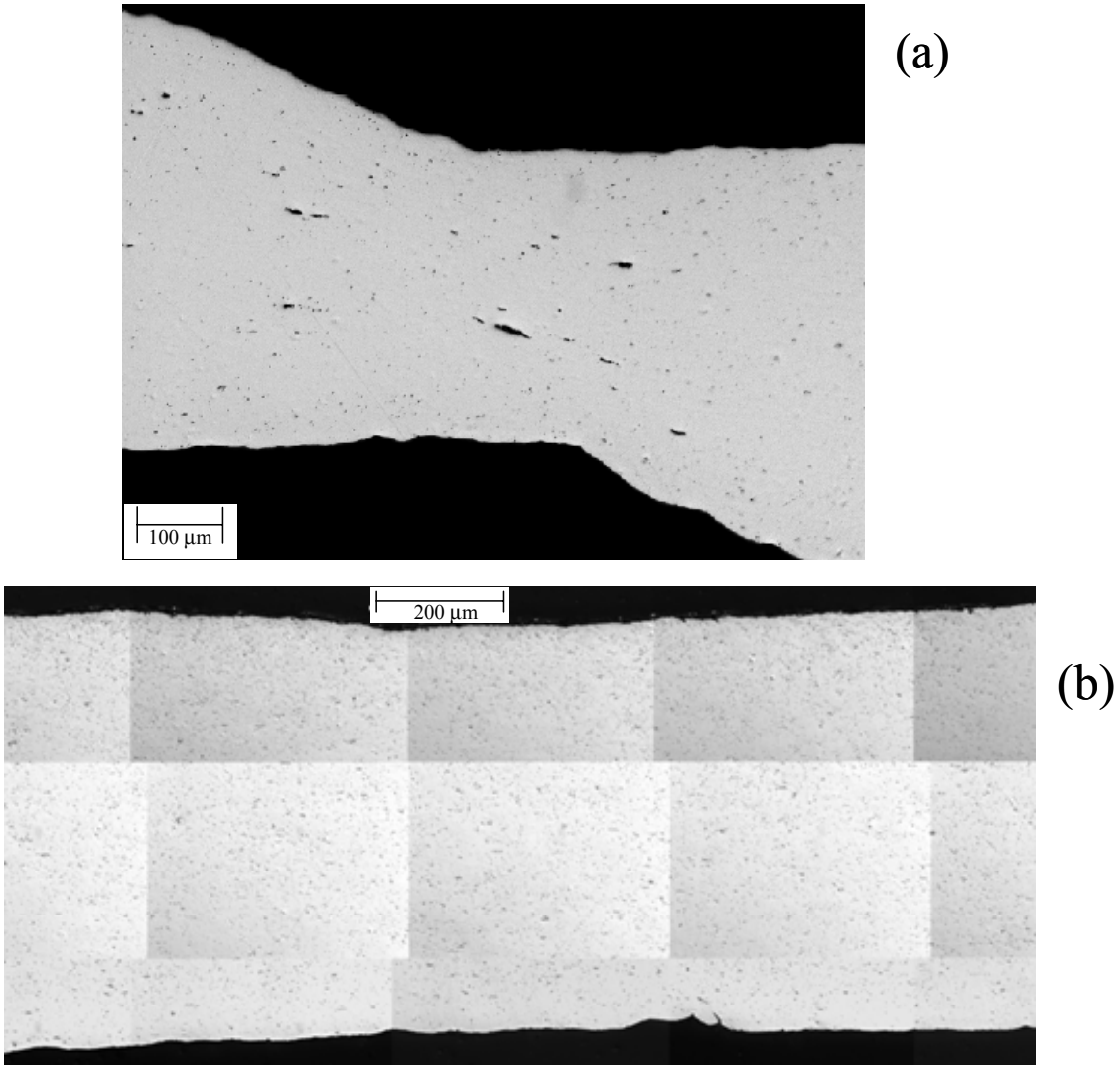

Figure 73: Comparison between a) AA5754 and b) an AA6111 free-formed necks.

There were also differences observed in the conical samples. The steps on the AA5754 samples were more pronounced than those in the AA6111 cones. Figure 74 shows cross-sections of the steps in specimens produced using different cone angles for both materials. In the AA6111 samples, the steps became less pronounced with increasing cone angle. In contrast, no apparent change in the severity of the step is evident in the AA5754 samples. The reason for this difference in behaviour remains an open question.

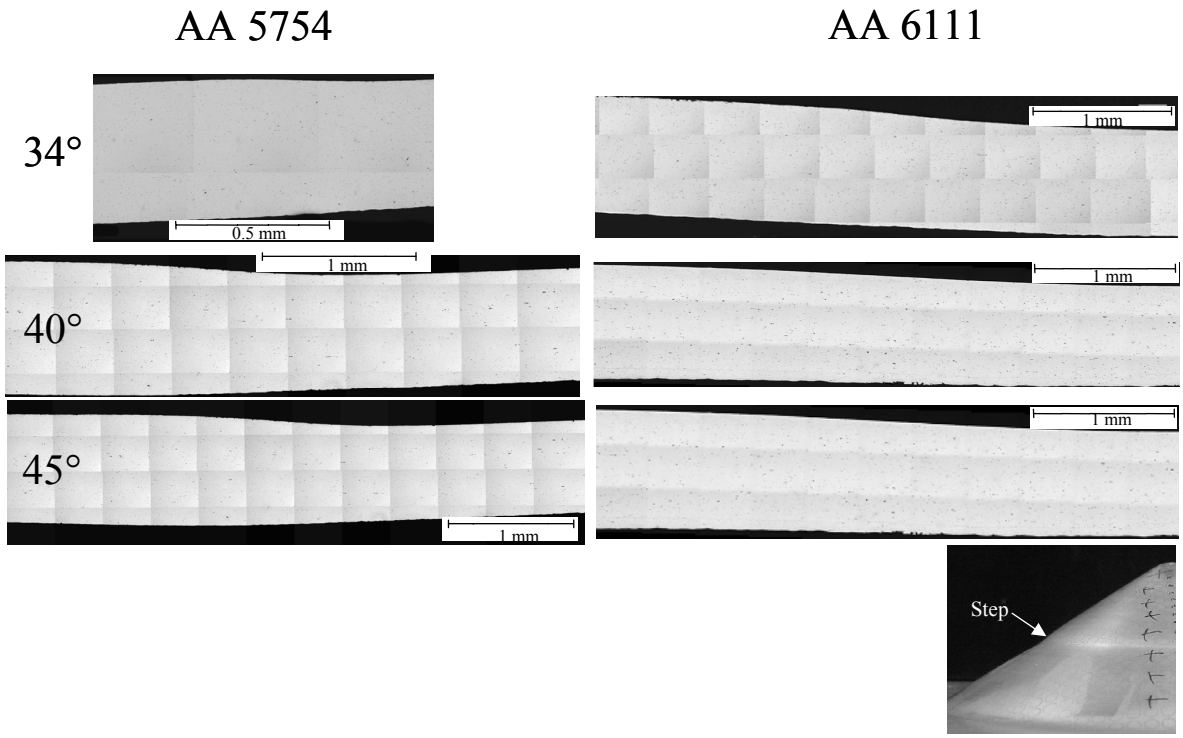

Figure 74: Comparison of AA5754 and AA6111 steps produced by the different conical dies.

The most pronounced differences between the two materials occurred in the failure modes of the conical samples. The materials could not be formed into the 45º cone safely, both failing by either necking or fracture. AA5754 failed in the area below the step, where distinct necks developed, and in the burnished area below the tip, where the material fractured (see Figure 45). Figure 75 shows micrographs of the fracture and necking present in the AA5754 sample shown in Figure 45. The material thinned considerably before fracture, in a manner more consistent with plastic collapse than with ductile fracture. The necked area shows voids elongated in the forming direction, with significant thinning but relatively little damage. Large voids, similar to the ones present in the neck, could be the precursor to the

rectangular feature present in the tip of the fracture surface. The material appears to thin considerably without a corresponding increase in damage, until the voids grow and coalesce to a size where the surrounding areas will either plastically collapse or fail in shear.

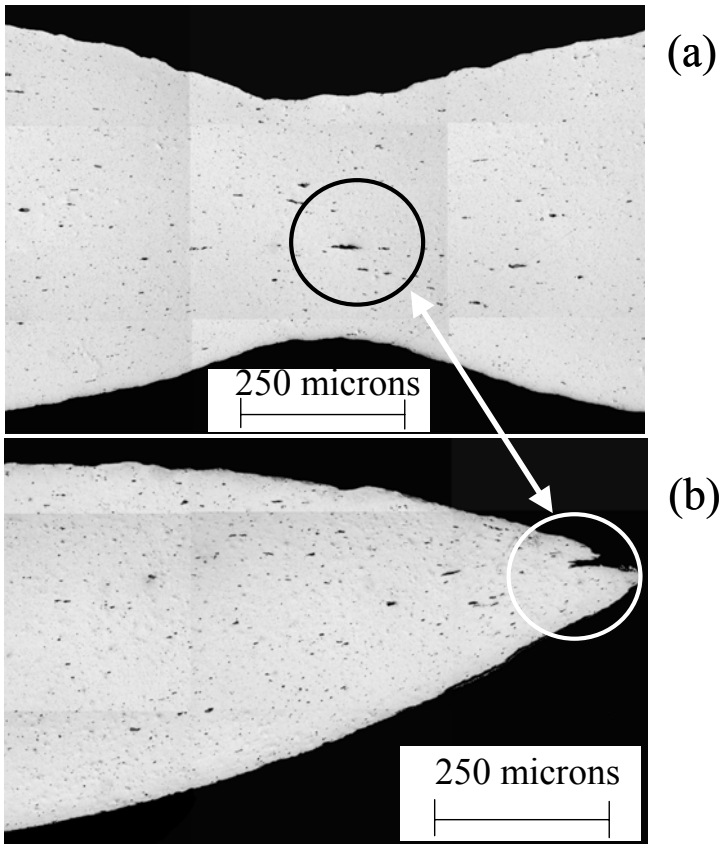

Figure 75: Micrographs of a) the neck and b) the tip fracture of an AA5754 specimen formed into a 45º cone.

The failure mode of the AA6111 samples was quite different from that in the AA5754 specimens, as can be seen in Figure 50 and Figure 51. Figure 76 shows micrographs of the fracture zones in an AA6111 specimen formed in a 45º die. Two distinct fracture modes are present, the "saw tooth" fracture that occurs on the side of the samples (see Figure 50) and the fractures present at the tip of the sample (see Figure 51). The saw tooth fracture (see Figure 76a) shows evidence of ductile-shear fracture, with no clear indication of a neck. The tip fracture (see Figure 77b) is quite distinctive, with a curling feature that abruptly ends and gives way to what appears to be a shear fracture. From observations of the sample and the micrographs it can be deduced that the fracture starts on the tip of the curl in a manner

resembling peeling and, after a critical point, the sample fractures in shear. This behaviour will be further discussed in the following section.

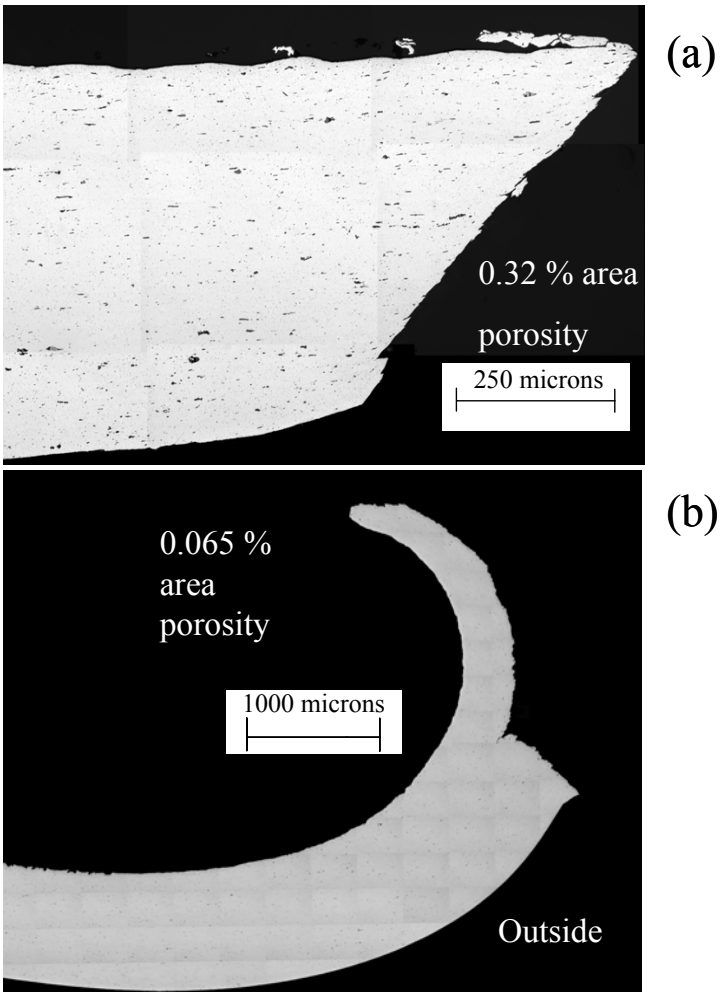

Figure 76: Micrographs of a) the "saw tooth" and b) the tip fractures present in AA6111 samples formed with the 45º die.

4.4 Fractography

Both materials failed in a manner not expected in sheet metal forming. The microscopy revealed evidence of fracture modes other than ductile fracture. To determine how the materials were fracturing, quasi-static, free-formed and conical samples were analyzed using a scanning electron microscope (SEM).

Samples of both materials were tested and fractured in tension under quasi-static conditions to provide a baseline for the analysis of the fracture of the EM formed samples.

Figure 77 and Figure 78 show the fracture surfaces for AA5754 and AA6111, respectively. Both alloys fail by ductile failure; however, they do not fail in exactly the same manner. From the figures it can be seen that the AA5754 thins more than the AA 6111 before final fracture, and that AA5754 exhibits larger and deeper dimples. The AA6111 exhibits areas of few or no dimples, which is consistent with shear fracture and/or intergranular fracture.

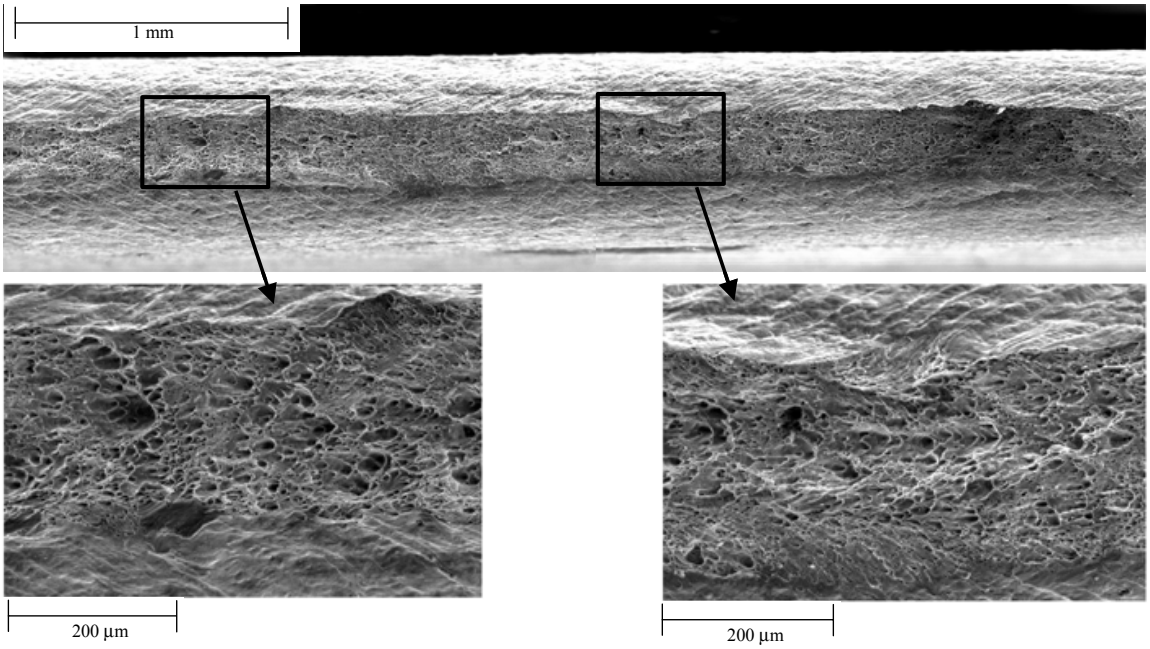

Figure 77: Fracture surface an AA5754 quasi-static tensile sample.

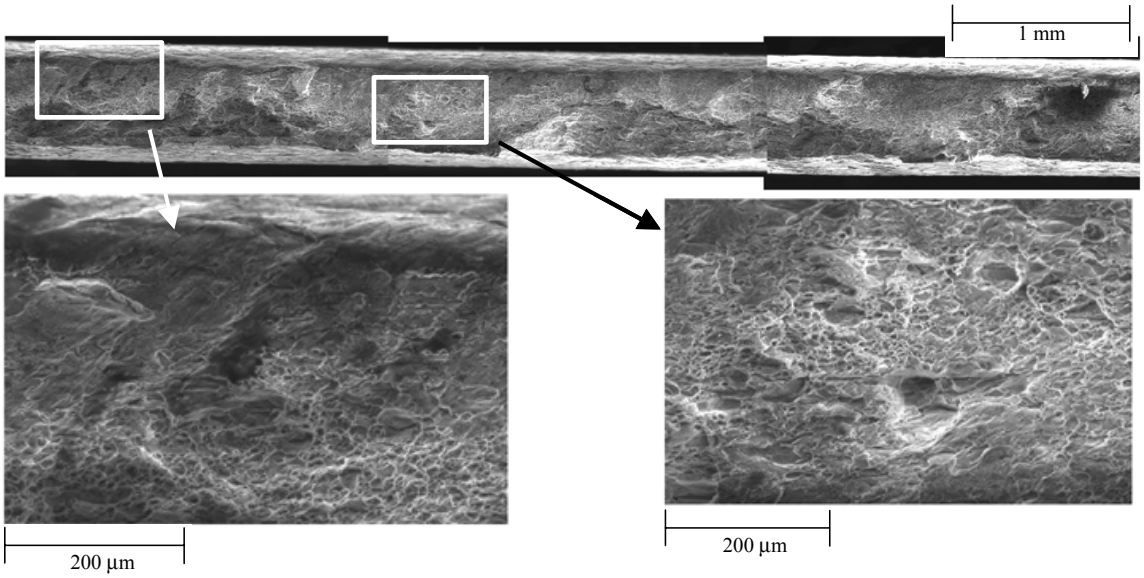

Figure 78: Fracture surface an AA6111 quasi-static tensile sample.

The fracture surface for a free-formed AA5754 sample is shown in Figure 79. Areas of ductile fracture predominate, with shear fracture present as well. The areas that failed under pure ductile fracture thinned more than in the quasi-static samples. High strain rate and inertial effects are the likely cause of the differences, though further research is required to confirm this.

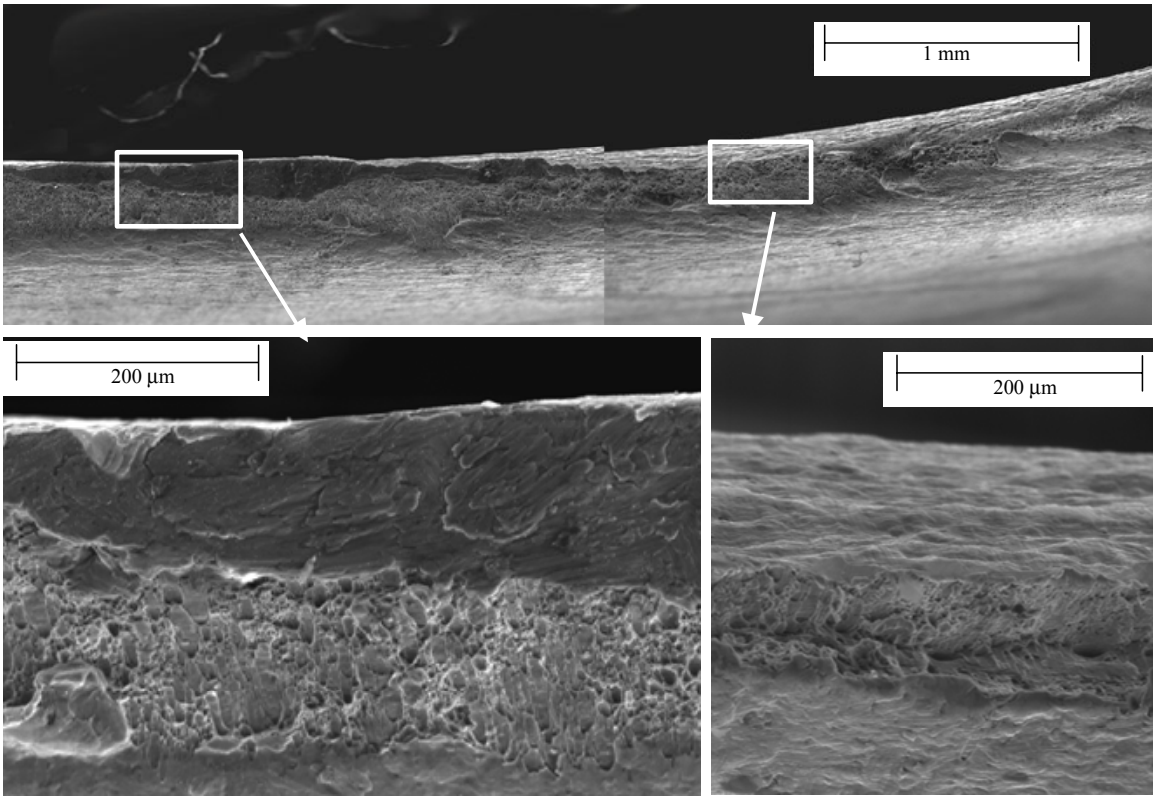

Figure 79: Fracture surface of a free-formed AA5754.

Figure 80 shows fractographs of the tip fracture of an AA5754 sample formed with the 45º cone. More shear fracture is present than in the free-formed case. The "knife edge" fracture shows evidence of shear and ductile fracture, as well as plastic collapse. This is consistent with the observations made from the microscopic analysis. Figure 80 B shows evidence of shear fracture and void sheeting, which consists of elongated dimples. It is clear that the fracture modes are different for the quasi-static, free-formed and cone die cases.

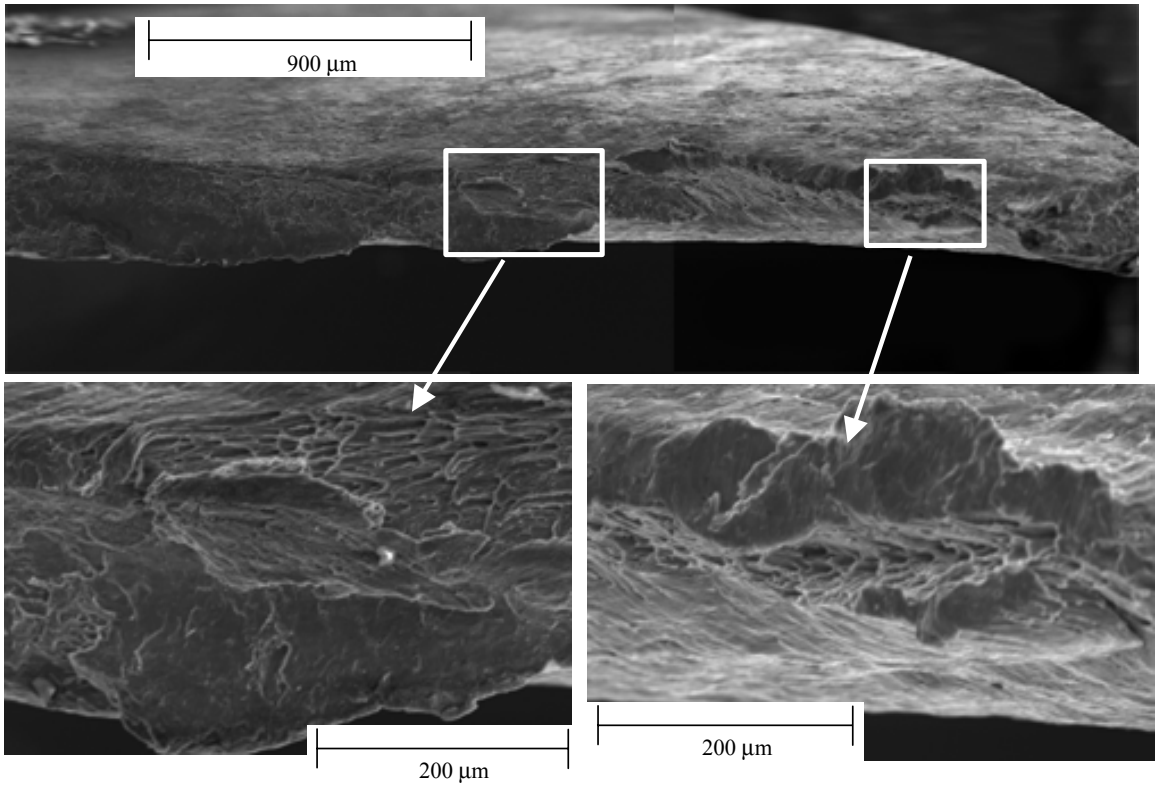

Figure 80: Fracture surface of a tip fracture in an AA5754 sample formed into a 45º cone.

Figure 81 shows the fracture surface of a free-formed AA6111 sample. It is similar to the quasi-static fracture, but with less thinning. The reasons for the difference between the quasi-static and free-formed fractures is not yet clear. Additional work is needed to understand the observed differences.

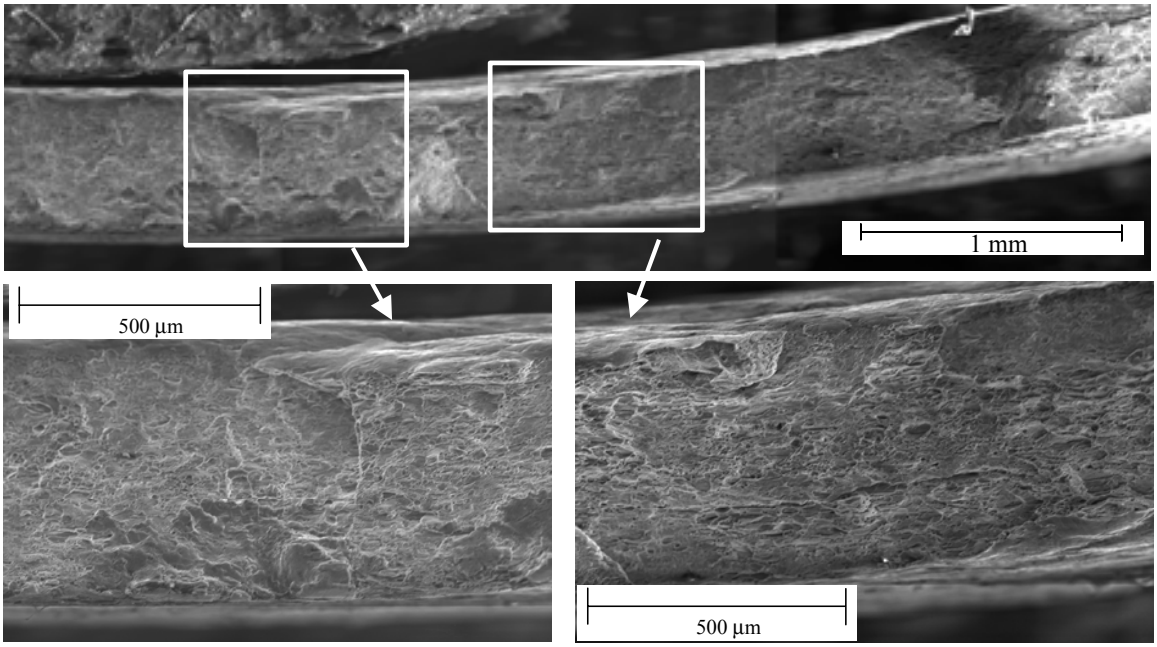

Figure 81: Fracture surface of a free-formed AA6111 sample.

The AA6111 cones failed in two distinct manners, a through-thickness saw tooth fracture on the areas below the step and a peeling type of fracture in the area of the tip. These fractures are not only different to the naked eye, but present very different features when examined using the SEM. Figure 82 shows the fracture surface of the saw tooth fracture. A combination of shear and ductile fracture characteristics can be observed, with more evidence of shear fracture than in the quasi-static and free-formed cases.

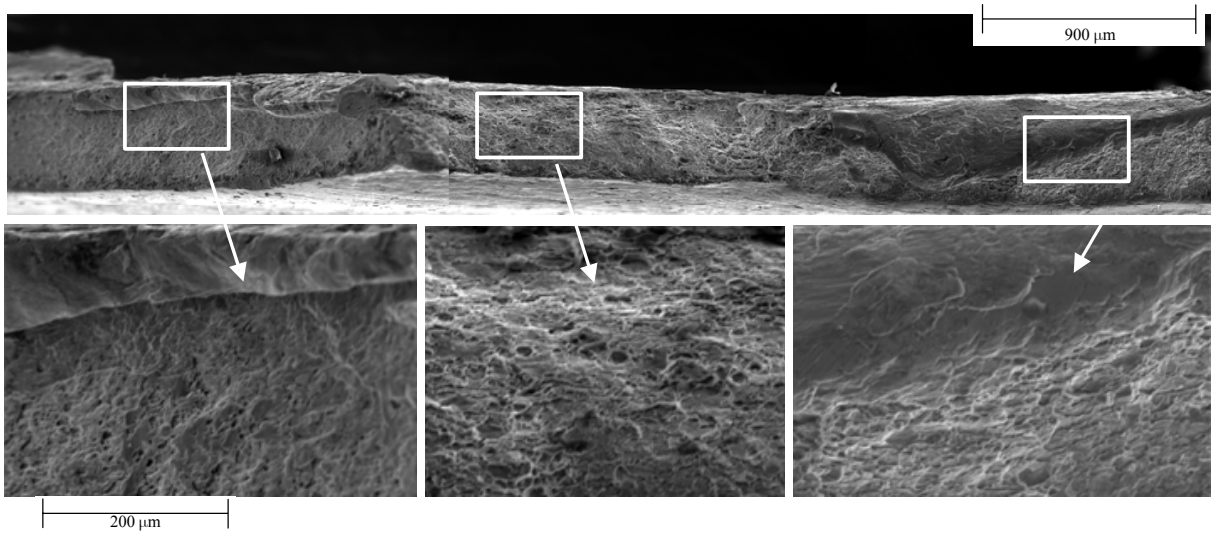

Figure 82: Fracture surface for the "saw tooth" fracture in an AA6111 formed into a 45º cone.

As can be seen in Figure 83, the fractures present at the tips of the failed AA6111 conical samples were different than the saw tooth fractures. Intergranular failure and shear fracture are dominant, with very little evidence of ductile fracture. The fractures start with intergranular failure from the inside and, after a certain amount of material has failed this way, the material fails in shear. This type of failure is very different than the ones observed in the quasi-static and free-formed cases.

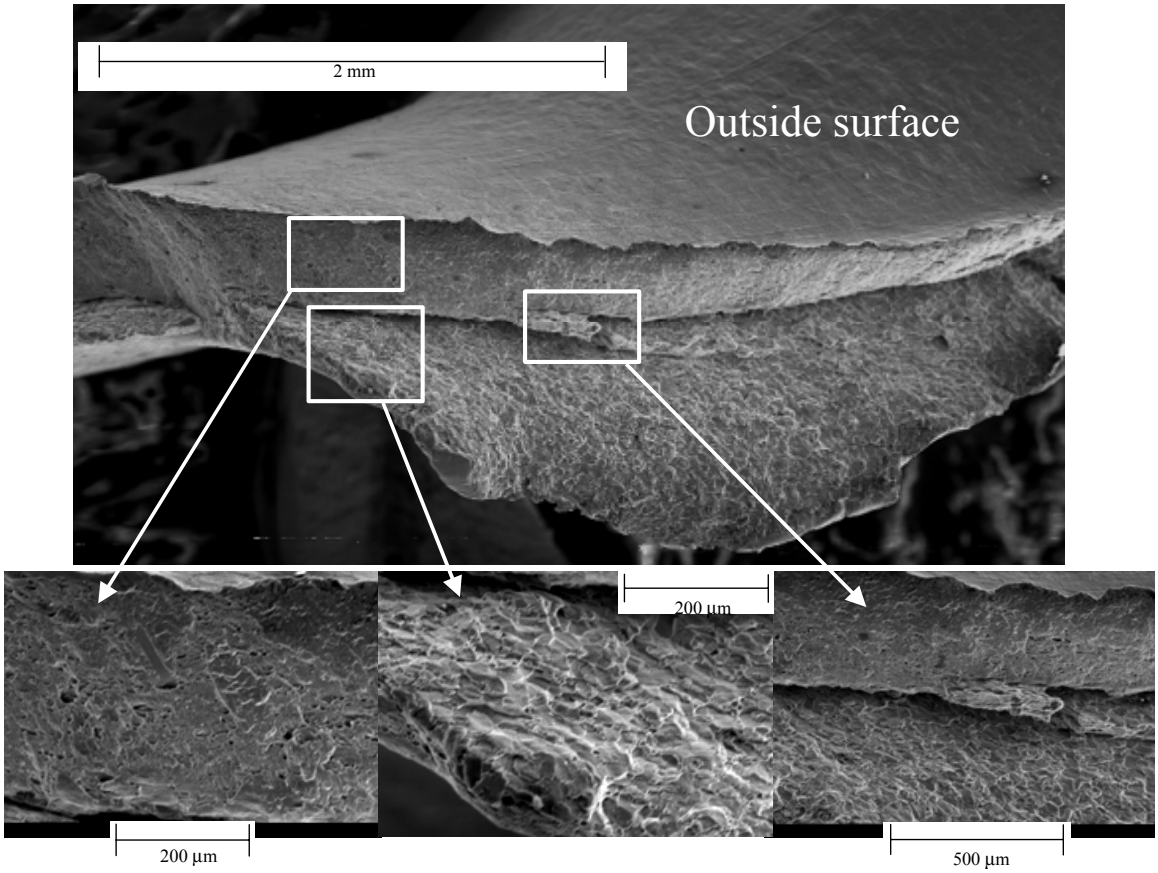

Figure 83: Fracture surface for the tip fracture of AA6111 formed into a 45º cone.

4.5 Summary

The experiments indicate that the tool/sheet interaction has a significant effect on the formability, damage evolution and fracture modes of the alloys studied. Free-formed samples, for which inertial and high strain rate effects would be important, showed only limited formability increases when compared to a quasi-static FLD. This response contrasts that of the samples formed into the conical dies where significant formability increases were recorded. The samples formed into the conical die only showed increases in damage in specific regions and the levels never reached those in the localized regions of the free-formed samples. The fractographic analysis showed that the fracture modes for the materials were significantly different between the free-formed and the conical samples. The free-formed fracture showed evidence of some possible rate or inertial effects, mainly in the AA5754, where there was

evidence of shear fracture, which was not observed in the quasi-static samples. Fractures from the conical samples were significantly different from those of the free-formed and quasi-static samples for both materials. Despite significant differences between the alloys, both exhibited low levels of ductile damage and evidence of shear fracture, plastic collapse and, in the case of the AA6111, inter-granular failure. These changes in fracture modes are consistent with the existence of a damage suppression mechanism. All of the experimental results indicate that the tool/sheet interaction is playing the most important role in the increased formability observed, and that this increase is due, at least in part, to damage suppression. The numerical analysis that will be presented in the next chapter was undertaken to provide more information on this interaction and how it affects the formability of the material.

CHAPTER 5

NUMERICAL RESULTS

The numerical analysis was carried out to gain additional insight into the EMF process. The evidence presented in the previous section clearly shows an increase in formability and evidence of damage suppression. It is also evident that the tool/sheet interaction plays a very important role. The numerical models were used to try to determine the mechanisms by which the tool/sheet interaction affects the formability of the material. Numerical results will be presented for AA5754 necked free-formed and 40º conical samples; only this data will be shown to be concise, since it is representative of the predicted trends. AA5754 was chosen as the focus for the simulations since the models for this material produced good agreement with the experimental results.

5.1 Deformation Histories

The EMF process applies pressure to the workpiece in a unique way that leads to distinctive sheet deformation histories, as can be seen in the predicted deformation history shown in Figure 84. The prominent feature is the lag of the displacement of the centre of the sample, which eventually "catches up" with the sample and snaps through to form the distinctive protrusion that leads to the fracture of the tip. The pressure is only applied from 0.110 to 0.144 ms, thus the majority of the deformation occurs after pressure ceases to be applied.

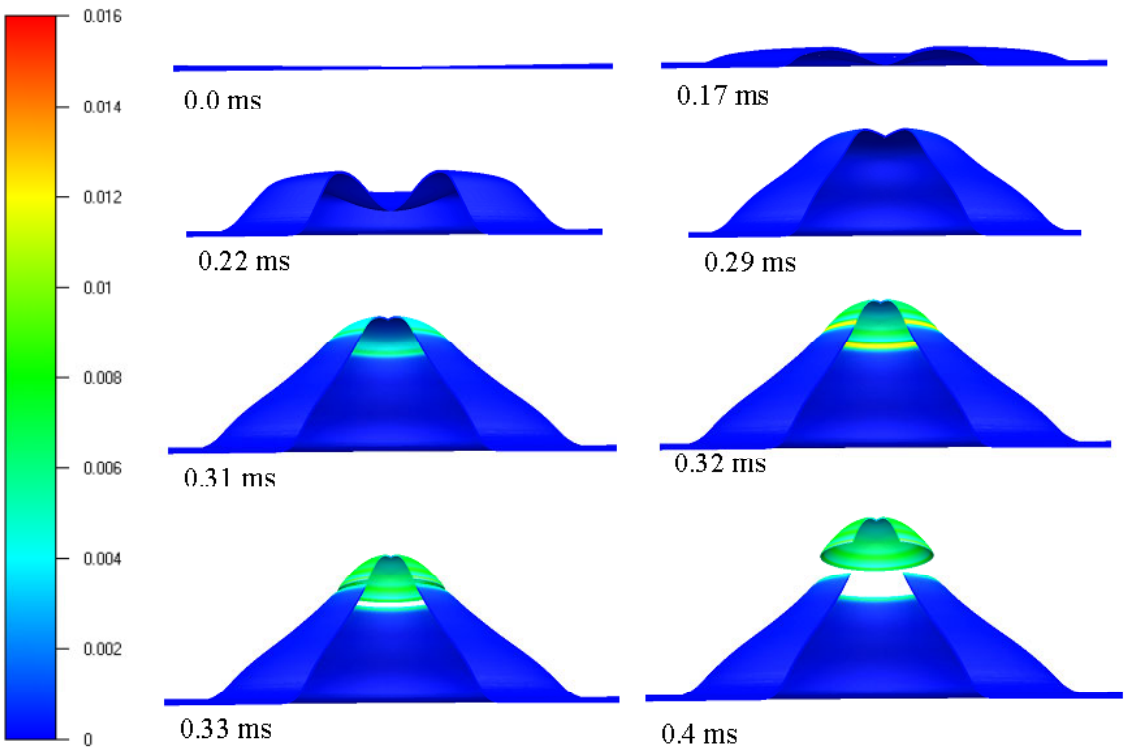

Figure 84: Deformation history of free-formed AA5754 sheet. The image is the result of revolving the 1/8th model for illustration purposes. A 45º section has been removed to observe the inside of the sample. Contours are of void volume fraction (not adjusted for nucleated second phase particle fraction).

When the material is formed into a conical cavity, the displacement of the centre still lags, but the material is constrained by the die. This leads to the deformation history shown in Figure 85. The sheet progressively "rolls up" against the die surface, leading to a circular line contact that moves upwards as the sample is formed. One of the results of this behaviour is the uneven distribution of the predicted strains and damage distributions. Damage is concentrated in the areas of the tip and the step, with the damage on the outside and inside surface of the sample being slightly different. As a result of this forming history, the sheet does not interact with the tool as it would in a conventional sheet forming operation. The sheet goes through bending, impact and straightening, as will be discussed in the next section.

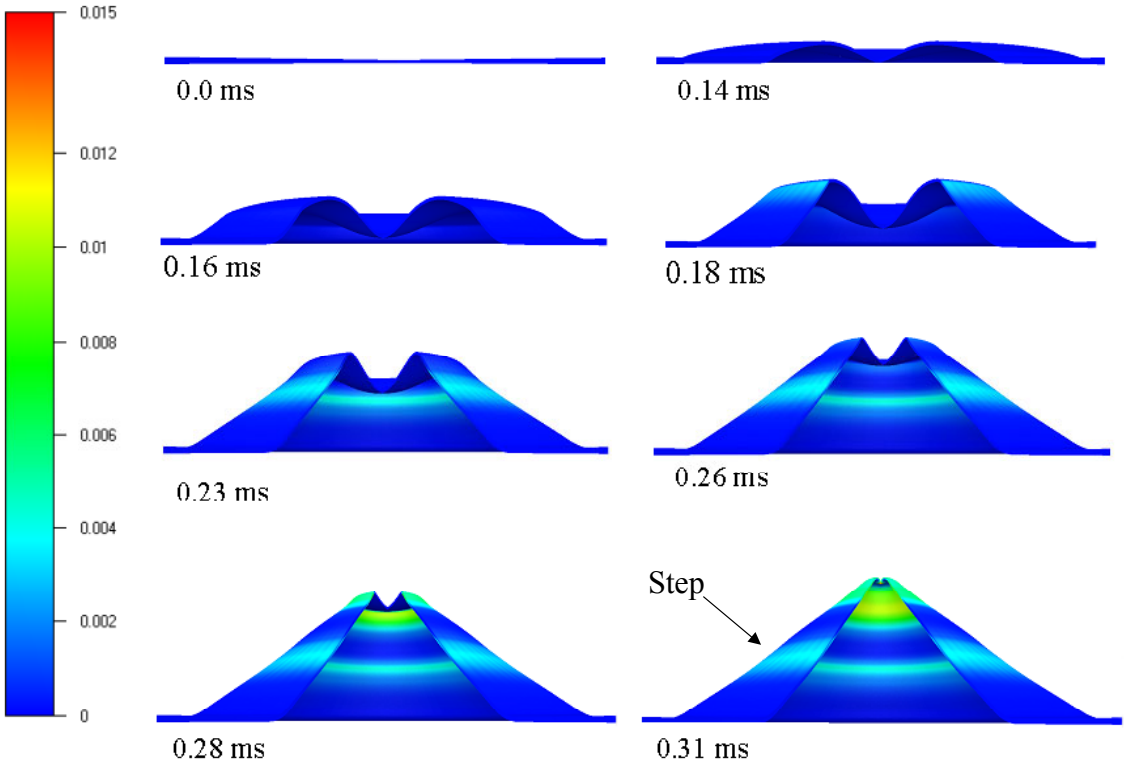

Figure 85: Deformation history for an AA5754 sample formed into a 40º cone. The image is the result of revolving the 1/8th model for illustration purposes. A 45º section has been removed to observe the inside of the sample. Tooling is not shown for clarity. Contours are of void volume fraction (not adjusted for nucleated second phase particle fraction).

5.2 Validation of Model

To validate the model, the results were compared with available published data and with the experimental results. The predicted deformation history of the free form process was compared to published experimental data and results from fully coupled numerical analysis from the literature (see Figure 86). It can be seen that the current model exhibits good qualitative agreement with the published deformation histories for similar processes.

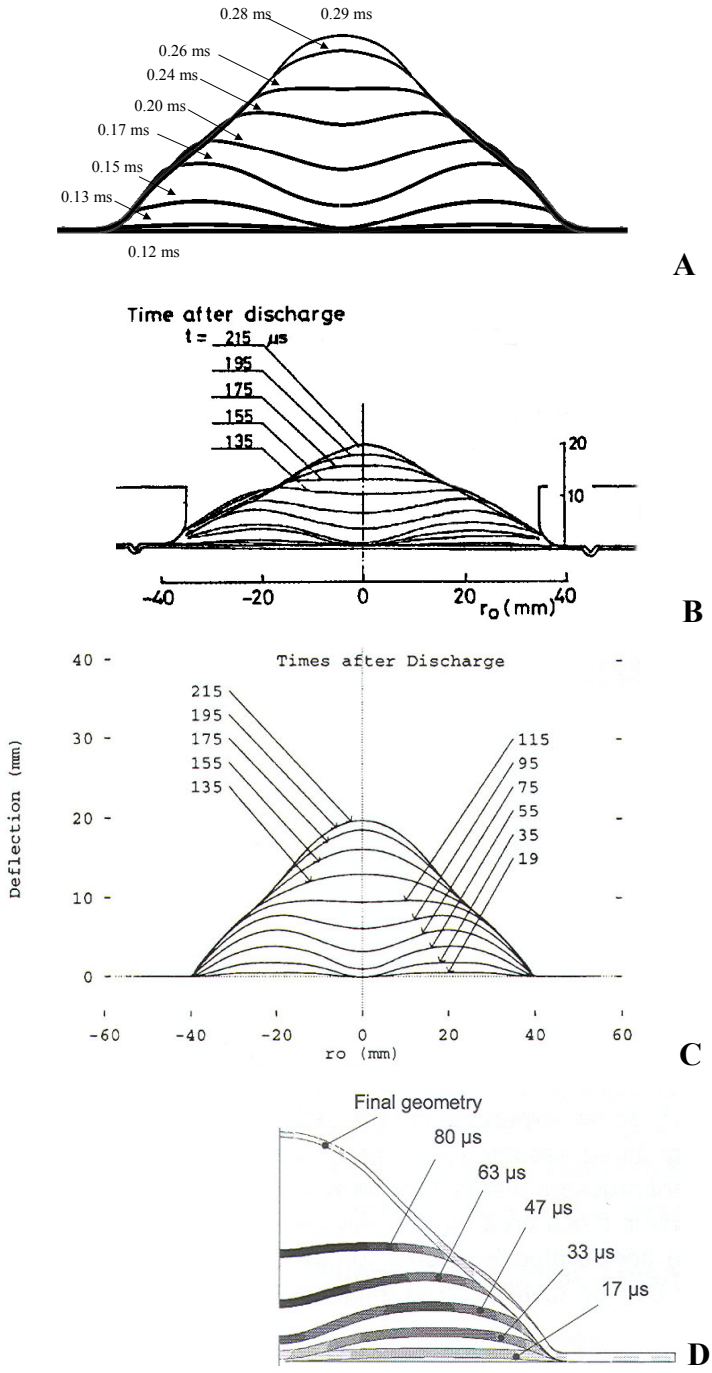

Figure 86: Free form deformation history for a free-formed sample predicted by the model compared with published experimental and coupled numerical histories. Current model is shown in A. Experimental data from Takatsu *et al.* [19] is shown in B. Results from fully coupled models are shown in C taken from Fenton and Daehn [37] and D taken from Risch *et al.* [58].

5.2.1 Predicted Sample Heights

Predicted and measured average height of three samples is compared in Table 8. For both materials, the largest errors occurred in the free-formed cases, with the model consistently over predicting the height. The over predictions were significantly higher for the AA6111 samples, with errors being approximately twice those present in the AA5754 samples. Not surprisingly, the cone height predictions agreed very well with the experimental results. The AA5754 models slightly under predicted the measured heights, while the AA6111 model over predicted the heights. The greatest over prediction was for the AA6111 45º cones. This over prediction is due to the buckling of the samples (see Figure 70), which led to incomplete die fill. The model was unable to predict buckling as will be discussed in Section 5.7.

Table 8: Comparison between numerically predicted and experimental sample heights. For details on individual sample heights and forming conditions see Table 3 and Table 4. * Average of highest point in the samples.

Sample	Average Measured Sample Height (mm)	Predicted Height (mm)	Difference (%)
AA 5754			
Free form	33.5	40.0	20
Necked free form	38.5	44.7	15
34º	38.7	37.6	-3
40º	46.9	46.9	0
45º	54.3	53.9	-0.7
AA 6111			
Free form	29.0	42.58	34
Necked free form	31.9	44.6	29
34º	35.9	37.6	5
40º	44.9	46.7	4
45º	50.1*	53.9	7.6

5.2.2 Predicted Versus Experimental Strains

Predicted strains were compared with experimental values to further validate the model. The measured and predicted radial and hoop strains for the AA5754 samples are shown in Figure 87 through Figure 91. The free-formed safe and necked predictions agree reasonably well with the experimental results. The predicted strains are generally higher than measured, which is consistent with the sample heights comparison in Table 8. Slight

discrepancies exist between the location of maximum strain and the magnitudes. The difference in the location of the peak is not surprising due to the difference between the actual pressure distribution and magnitude, and the assumed distribution used in the numerical model. The oscillations in the radial strain predicted after the maximum were not observed experimentally; however, the multiple necks observed in the necked experimental samples are evidence that other localized areas of high strain are present.

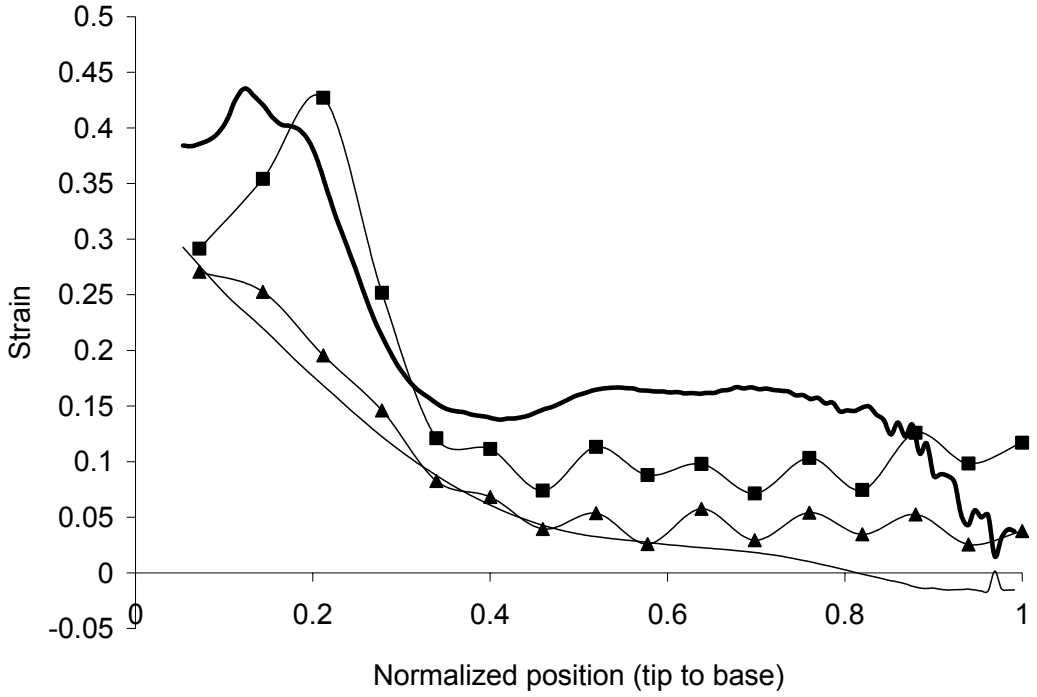

Figure 87: Predicted and measured radial and hoop strains versus radial position for an AA5754 free form sample. Measured radial = ■, measured hoop = ▲, predicted radial = ——— and predicted hoop = ———.

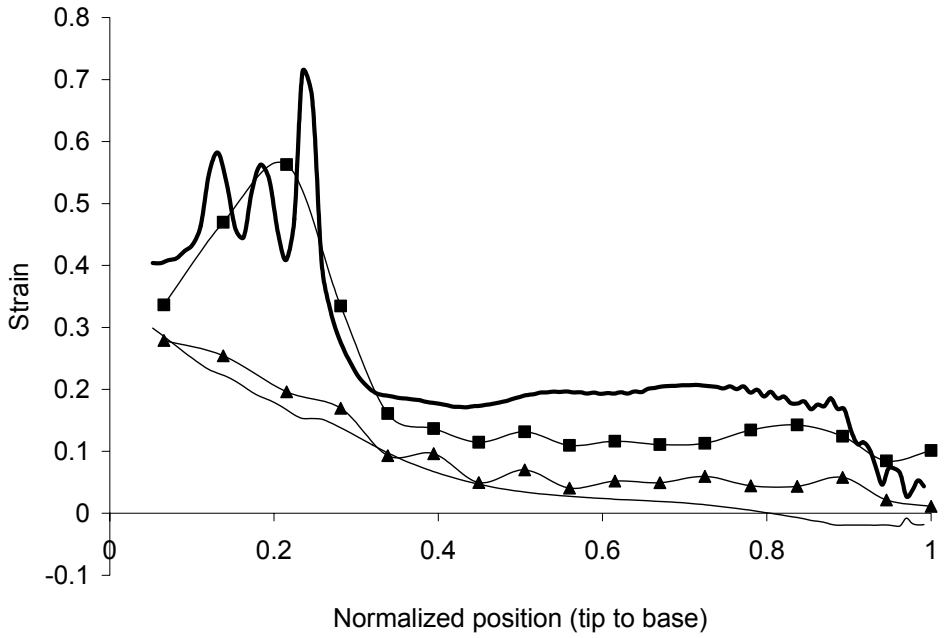

Figure 88: Predicted and measured radial and hoop strains versus radial position for an AA5754 necked free form sample. Measured radial = ■, measured hoop = ▲, predicted radial = ——— and predicted hoop = ———.

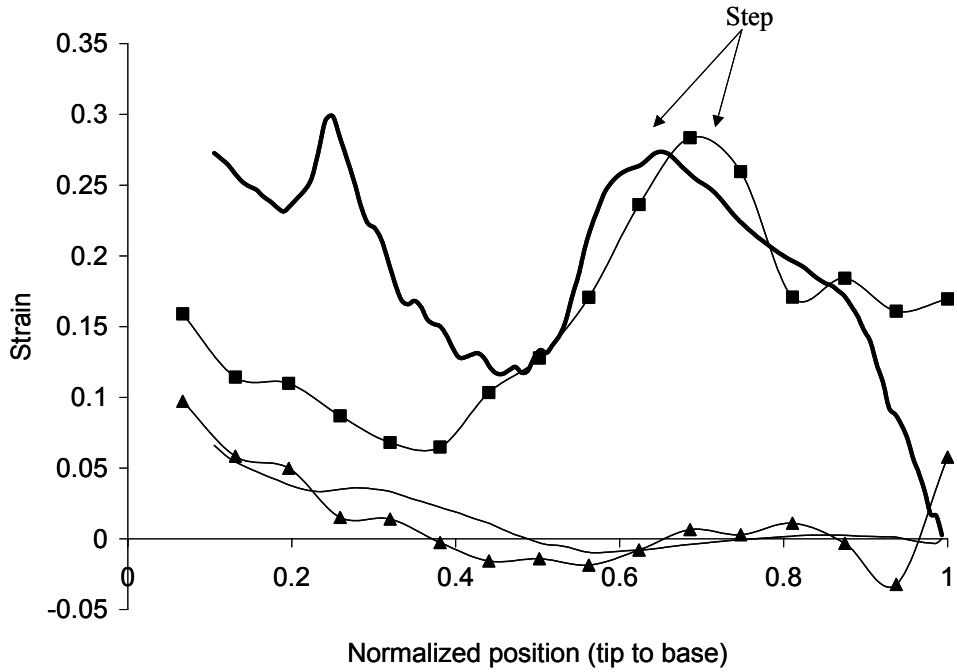

Figure 89: Predicted and measured radial and hoop strains versus radial position for an AA5754 34º conical sample. Measured radial = ■, measured hoop = ▲, predicted radial = ——— and predicted hoop = ———.

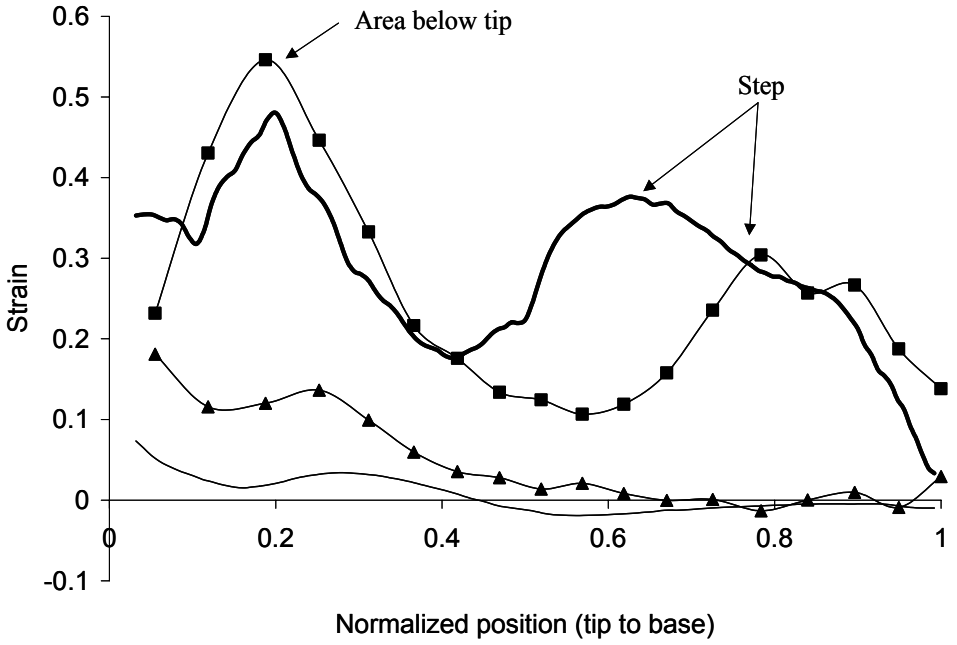

Figure 90: Predicted and measured radial and hoop strains versus radial position for an AA5754 40º conical sample. Measured radial = ■, measured hoop = ▲, predicted radial = ——— and predicted hoop = ———— .

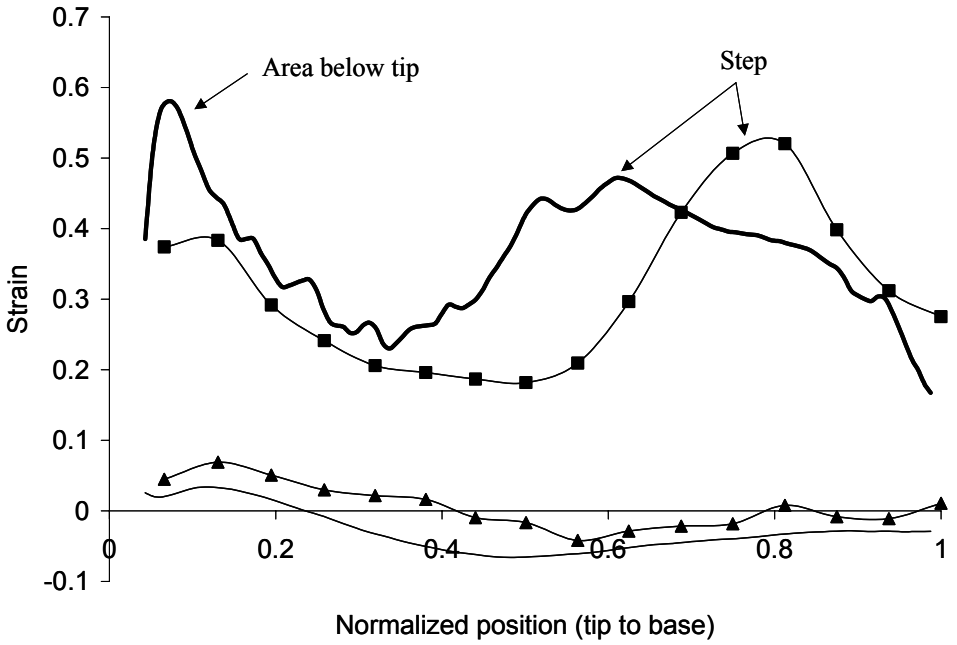

Figure 91: Predicted and measured radial and hoop strains versus radial position for an AA5754 45º conical sample. Measured radial = ■, measured hoop = ▲, predicted radial = ——— and predicted hoop = ———— .

The conical die predictions show the same trends as the experimental data, with the highest strains present in the area of the step and the area below the tip. The location of the step was accurately predicted for the 34º (see Figure 89) cone, but was not for the 40º (see Figure 90) and 45º (see Figure 91) cones. In contrast, the strains in the area of the tip were not accurately predicted for the 34º cones, but were more accurately predicted in the 40 and 45º cones. The discrepancies are largely attributed to the difference between the actual and simulated pressure distributions and point to the need for coupled EM simulations, which would be better able to capture the experimental pressure distributions.

The predictions for the AA6111 samples (see Figure 92 to Figure 95) again show the same trends but significantly over predict the strains in the free form cases. The over predictions in the free form cases are consistent with the over prediction of the dome heights presented previously.

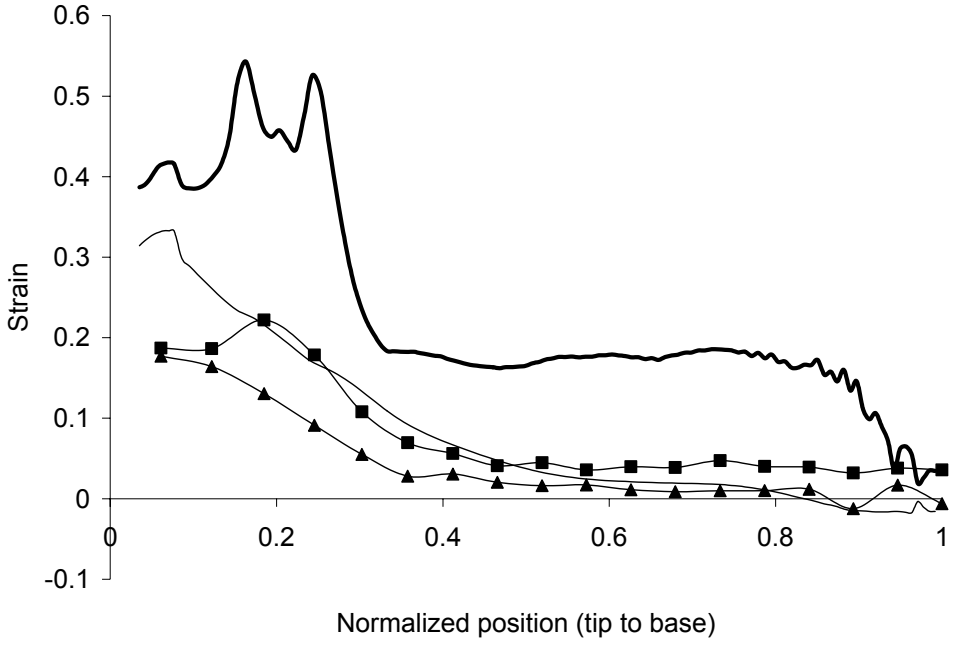

Figure 92: Predicted and measured radial and hoop strains versus radial position for an AA6111 free-formed sample. Measured radial = ■, measured hoop = ▲, predicted radial = ——— and predicted hoop = ———.

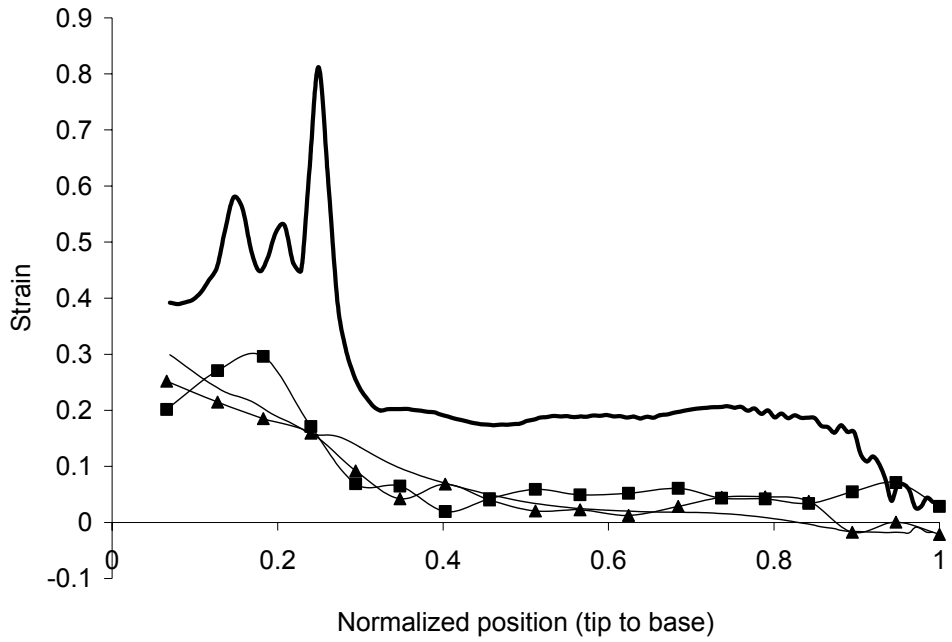

Figure 93: Predicted and measured radial and hoop strains versus radial position for an AA6111 necked free-formed sample. Measured radial = ■, measured hoop = ▲, predicted radial = ——— and predicted hoop = ———.

The predictions for the AA6111 34º (Figure 94) and 40º (Figure 95) cones follow the same trends as seen in the AA5754. The predicted strains are more accurate than in the free-formed cases likely due to the geometric constraint imposed by the dies. The predicted strains in the area of the tip were much higher than the measured values due to the buckling that occurred in these areas, which resulted in lower strains. Due to the damage to the grids for the 45º AA6111 samples, no comparison is made with numerical results.

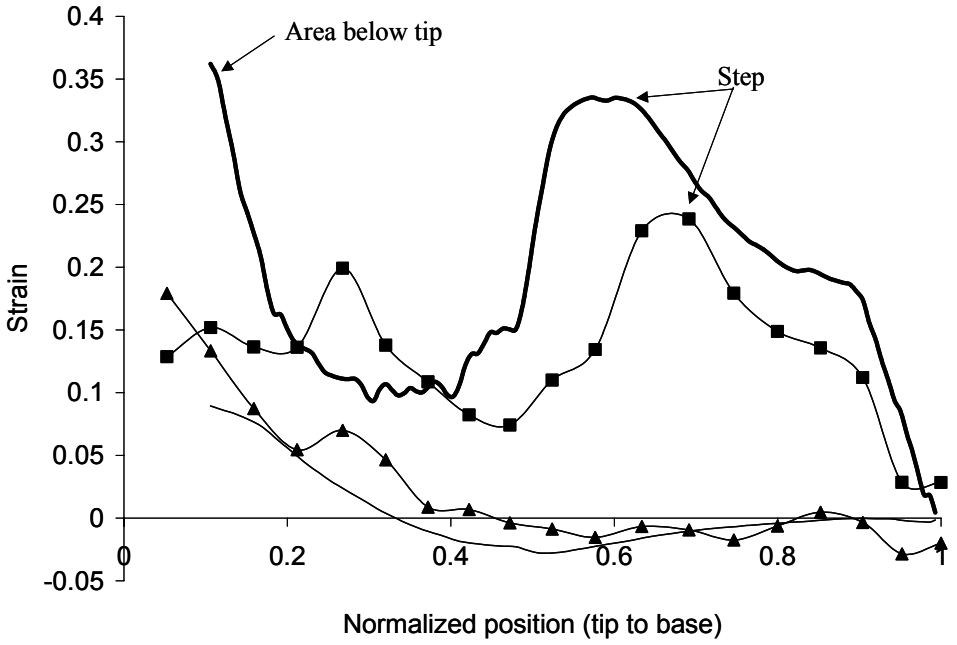

Figure 94: Predicted and measured radial and hoop strains versus radial position for an AA6111 34º conical sample. Measured radial = ■, measured hoop = ▲, predicted radial = ——— and predicted hoop = - - - - - - - .

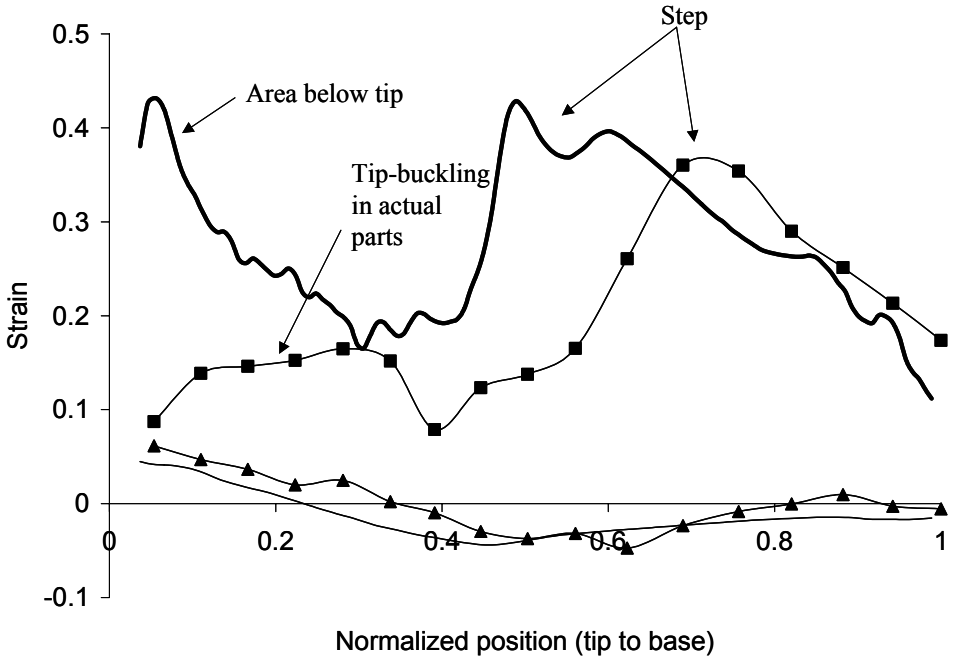

Figure 95: Predicted and measured radial and hoop strains versus radial position for an AA6111 40º conical sample. Measured radial = ■, measured hoop = ▲, predicted radial = ——— and predicted hoop = - - - - - - - .

In general, the predictions of dome height and strain were in greater error for the AA6111 blanks than for the AA7574. The causes of this over prediction are not completely understood. Natural aging of the AA6111 was suspected, due to the time elapsed between the solution heat treatment and the experiments (between 6-9 months). AA6111 becomes stronger as it ages and this could cause a difference between the flow curve that was used in the model and the actual flow curve. Due to material and equipment limitations the material could not be tested in the same conditions used to obtain the flow curves. Thus, to study the possibility of age hardening, models with flow curves scaled by 120, 150, 170 and 200% were made. The 200% flow curve produced results of comparable accuracy to those of the AA5754 (see Figure 96). This is clearly unrealistic, since AA6111 does not show a 200% increase in flow stress after ageing. Thus, the discrepancy between the measured and predicted results cannot simply be attributed to ageing and should be the subject of future study. Possible high strain effects and numerical effects, such as the effect of the mesh density and hardening rule, should also be investigated.

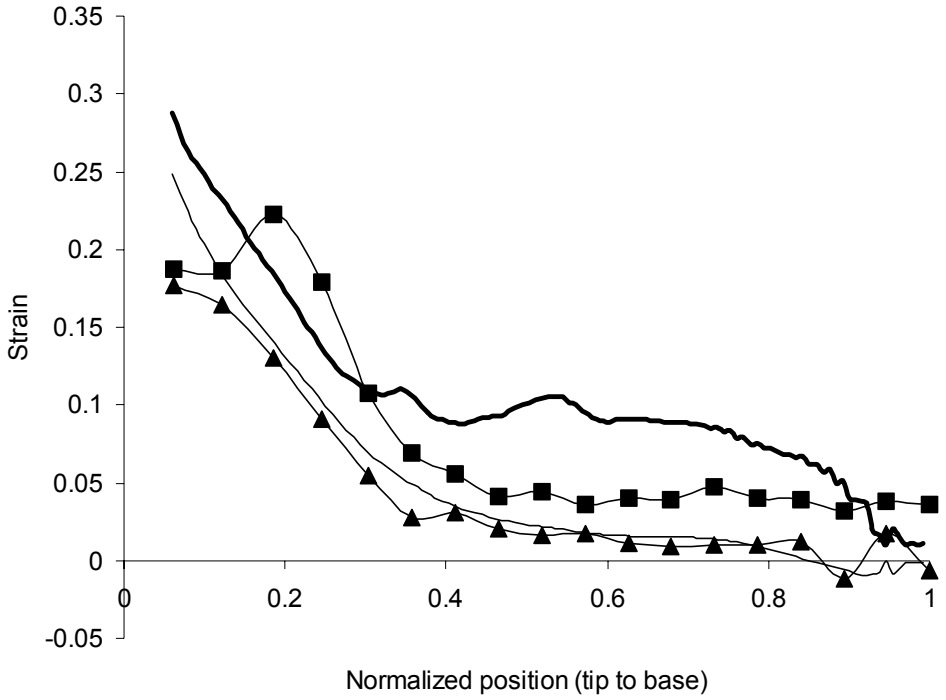

Figure 96: Predicted and measured radial and hoop strains versus radial position for an AA6111 free-formed sample with flow curve scaled by 200%. Measured radial = ■, measured hoop = ▲, predicted radial = ——— and predicted hoop = ———.

5.2.3 Predicted Maximum Pressures

The peak pressures used in the models were compared with the experimental charge voltages to see whether the same trends were followed. Due to the relationship between charging voltage and pressure (see Section 1.7), an increase or decrease in charging voltage between two processes, should be reflected in the model by the same change of numerical peak pressure. Figure 97 and Figure 98 show the pressure histories used for AA5754 and AA6111, respectively, and Figure 99 shows the charge voltages used. For AA5754, the lowest pressure was required for the safe free-formed sample, with the 34º cones requiring only slightly more pressure. As expected, the highest pressure was that required to form the sample into the 45º cone die. The AA6111 pressures increase from the safe free-formed to the sample formed into the 45º cone die. Unlike the AA5754, the peak pressure required to form the AA6111 samples into the 40º cone die was significantly larger than the safe free-form, in fact, it was larger than the pressure used for all of the free-formed models.

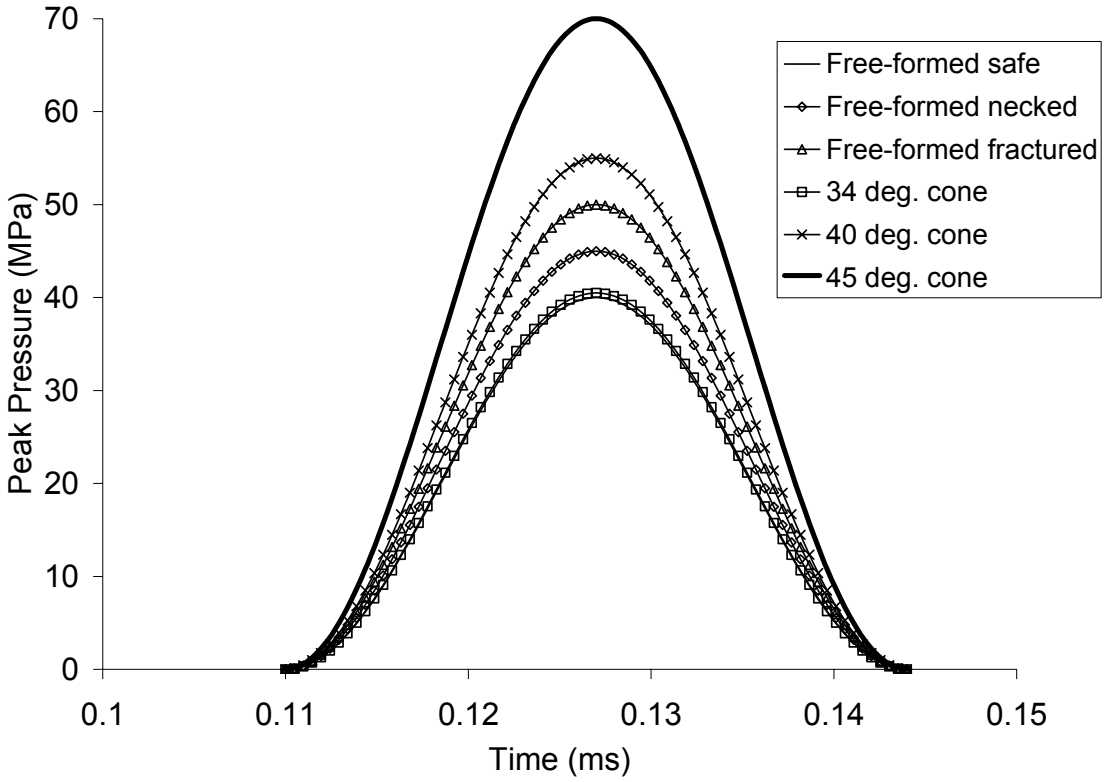

Figure 97: Peak pressure versus time profiles used for the AA5754 models. Note that the safe free form data is nearly identical to the 34º cone data.

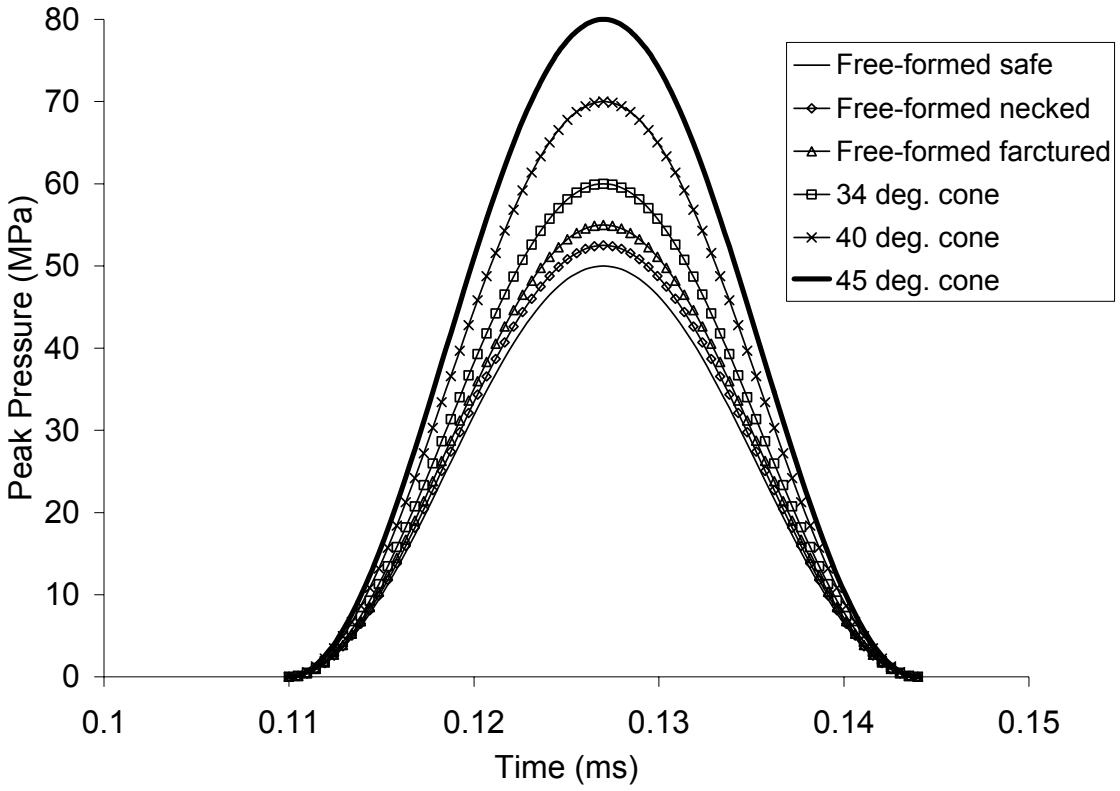

Figure 98: Peak pressure versus time profiles used for the AA6111 models.

The peak pressures used in the model showed similar trends to the experimental charge voltages shown in Figure 99, with two significant differences. The charge voltage for the AA5754 34º cone is larger than that for the safe free-formed sample, and is also larger than the charge voltage used for the same AA6111 cone. One 34º AA5754 cone was formed with a lower voltage (7.0 kV) experimentally, but this was not a representative sample size, and thus the higher voltage samples were used. The high voltage required to form the AA5754 34º cone should be confirmed by further investigations.

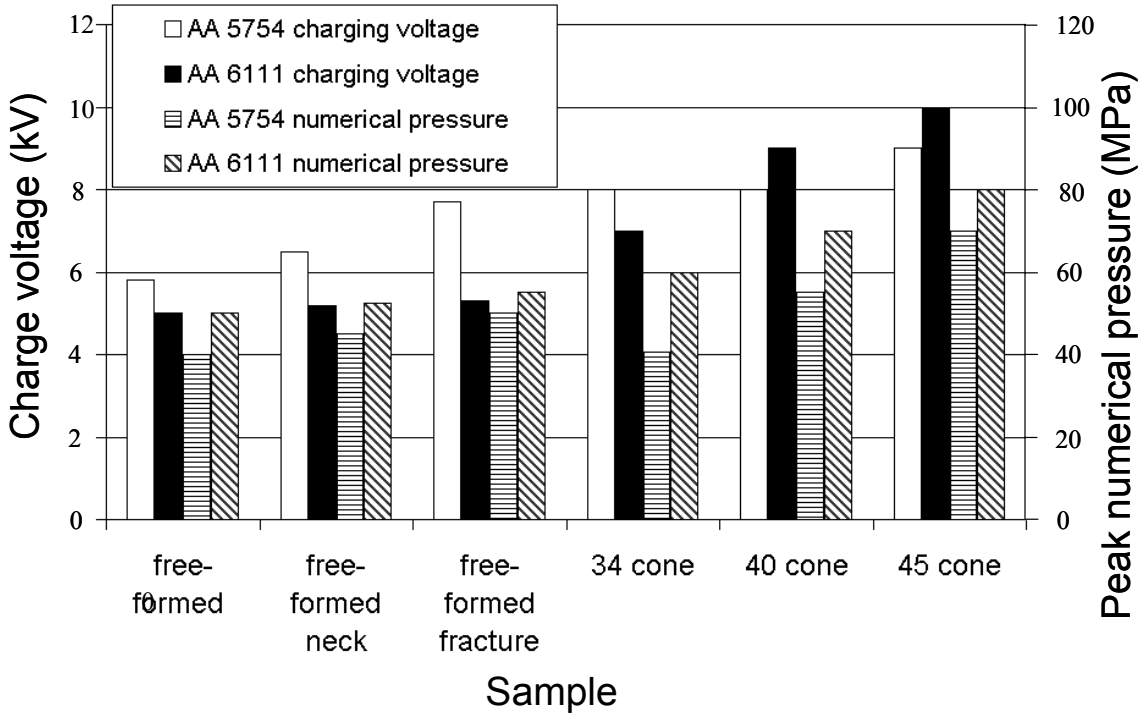

Figure 99: Experimental charge voltages and numerical peak pressures for AA5754 and AA6111.

The second difference is that the voltages for the AA5754 samples were higher than those for AA6111, which is not consistent with the model predictions, but is consistent with the reduced ductility observed experimentally. The predicted trends agree in general with the experimental charge voltages. The inaccuracies of the AA6111 results are consistent with the height and strain over predictions discussed previously.

5.2.4 Summary of Model Validation

The current model captures both the deformation and the strain distribution trends. The predictions for the AA5754 samples were more accurate than those for AA6111. The largest errors are present in the free form predictions, especially for AA6111. There are significant differences between the experimental and predicted AA6111 free-formed height and strains. These differences cannot simply be attributed to ageing effects, and the cause remains an open question. Strain rate and strain path effects could be playing a role, as will be discussed in Sections 5.4 and 5.5.

Overall, the predictions provided good qualitative agreement with the experimental results and it was determined that the model was sufficiently accurate to analyze the tool/sheet interactions that occur in the EMF process in question. To further increase accuracy, the parameters of the damage model were calibrated via a parametric study that compared the predicted time histories of damage with the values obtained from the metallographic analysis.

5.3 Parametric Study for Damage Parameters

Damage parameters were calibrated using the 40º cone experimental results. This approach was chosen because the samples formed using the 40º cone die exhibited more damage than the 34º cone samples but still showed no evidence of necking or fracture. The criteria for the calibration were accurate prediction of the observed trends in material damage, close correspondence with experimental results and prediction of fracture in the free form simulations. This approach was taken since, distinct damage trends were observed in the samples and damage measurements were made that could easily be compared to the numerical results. The fracture of the free-formed samples was chosen for validation purposes, since it was observed to be ductile fracture and thus predicting the onset of this failure was at least qualitatively within the capacity of the model. Since the purpose of the model was to provide insight into the process and not necessarily to provide accurate quantitative agreement, satisfaction of these validation requirements was deemed sufficient. The 45º cone samples were not pursued for calibration due to the complex failure modes observed, that the current model was not able to accurately predict. The challenges involved in predicting the failure of the 45º cones are outlined in Section 5.7.

Unless otherwise noted, the void volume fraction shown is the result of subtracting the predicted fraction of nucleated second phase particles from the void volume fraction provided by the model. This was done to ensure that the predicted and measured quantities being compared were the same, since the numerical model considers void volume fraction as the volume of the void and the second phase particle associated with it, while in the measurements only the voids were quantified as damage.

Figure 100 shows the sensitivity of the models to the nucleation strain for AA5754. As can be seen from the figure, an average nucleation strain, ε_n, of 50% best represented the results. The models used a void volume fraction required for coalescence, $f_{c,}$ of 1.6%. The

high values of porosity predicted for the tip of the cones are a result of the non-optimal mesh geometry used (see Figure 35).

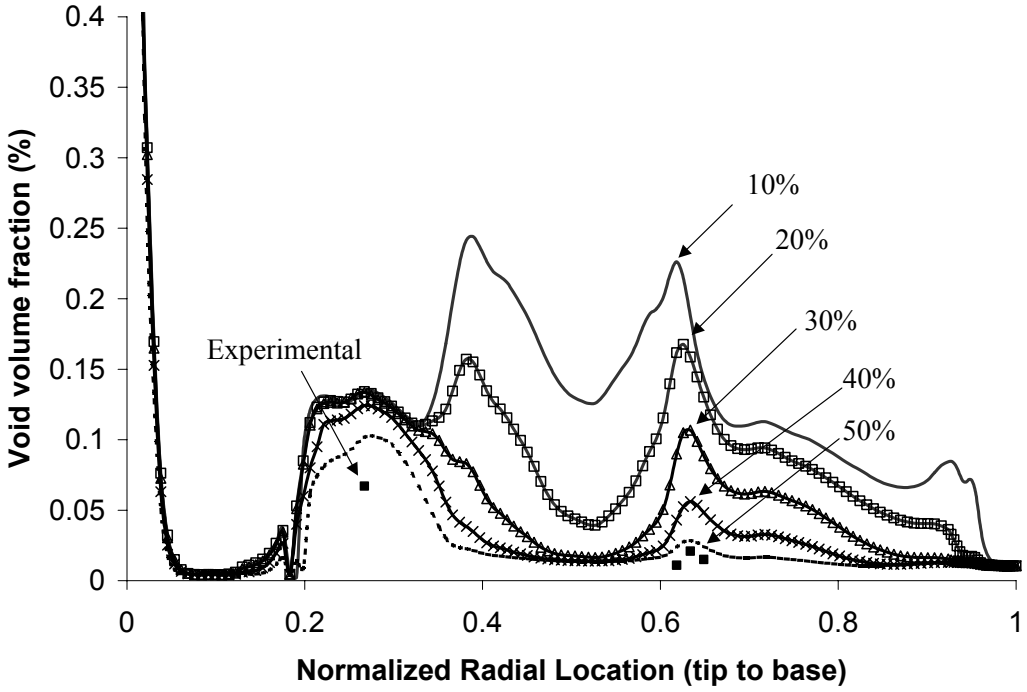

Figure 100: Effect of nucleation strain on predicted void volume fraction. Solid squares represent measured data for AA5754 40º cone samples. Data is presented from tip (0) to base (1).

The void volume fraction required for coalescence, f_c, is the critical factor determining the onset of failure, since after it is reached, the void volume fraction increases at a very rapid rate leading to failure shortly thereafter, as per Equation 3-2. Free form models with f_c values ranging from 1.0 to 5.0 % were tried to determine the effect of this parameter on the prediction of fracture. It was found that the results were virtually identical. This is due to the fact that the free-formed samples fail where the elements localize, and thus the high strains reached were the dominant factor affecting failure. To determine which value of f_c to use, the results of models with f_c values ranging from 1.0 to 2.2 % were examined; these values were chosen since they appeared to be realistic given the experimentally observed damage. Figure 101 shows that f_c has relatively little effect on the predicted porosities, as expected. The value

chosen for the simulations was 1.6%, since it best captured the measured values, as shown in Figure 102.

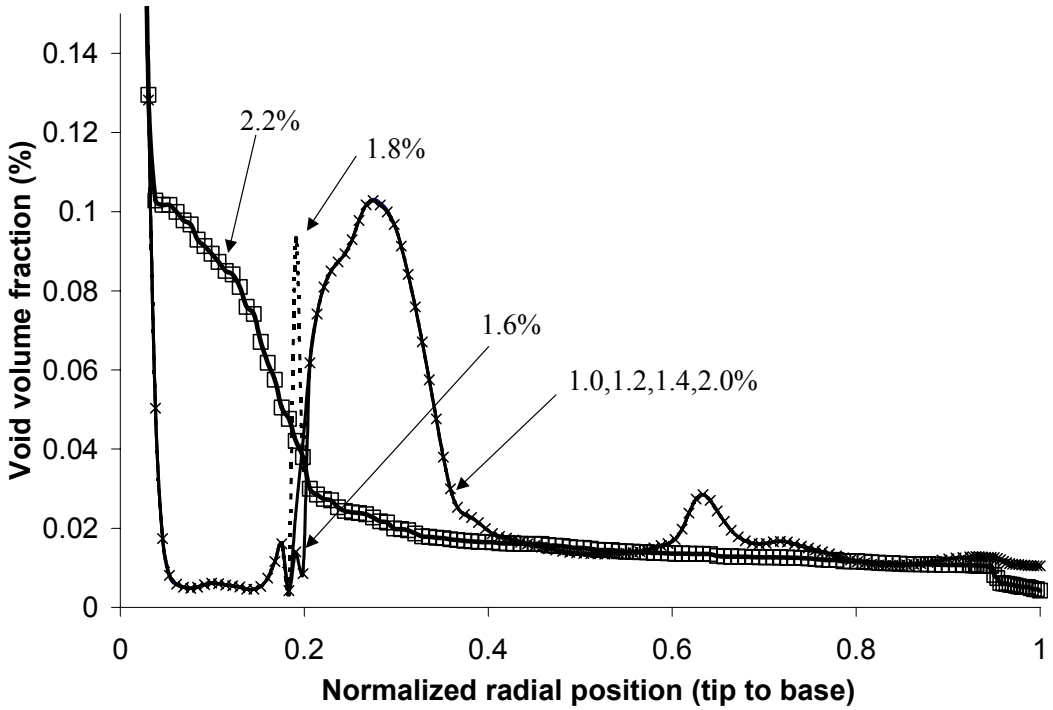

Figure 101: Effect on void volume fraction predictions of changing void volume fraction required for coalescence.

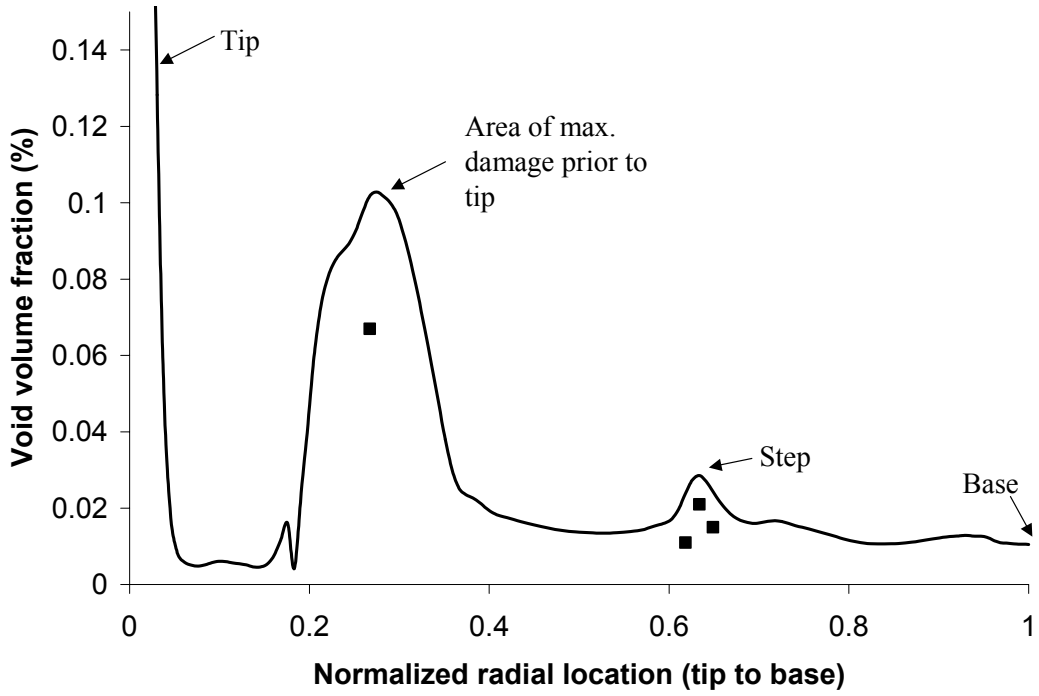

Figure 102: Predicted void volume fraction compared with experimental results for 50% nucleation strain and 1.6% void volume fraction required for coalescence to begin.

A similar calibration procedure was undertaken for AA 6111, the results of which are shown in Figure 103 and Figure 104. It resulted in the same parameters as AA 5754, that is a void nucleation strain of 50% and a void volume fraction required for the onset of coalescence of 1.6%.

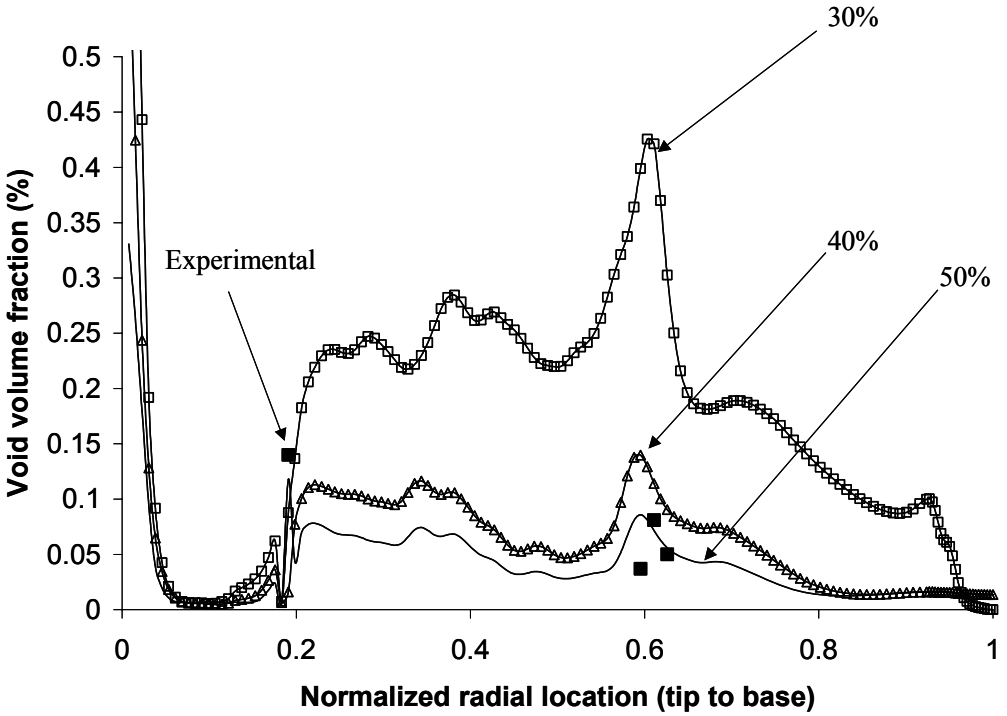

Figure 103: Effect of nucleation strain on predicted void volume fraction. Solid squares represent measured data for AA6111 40º cones.

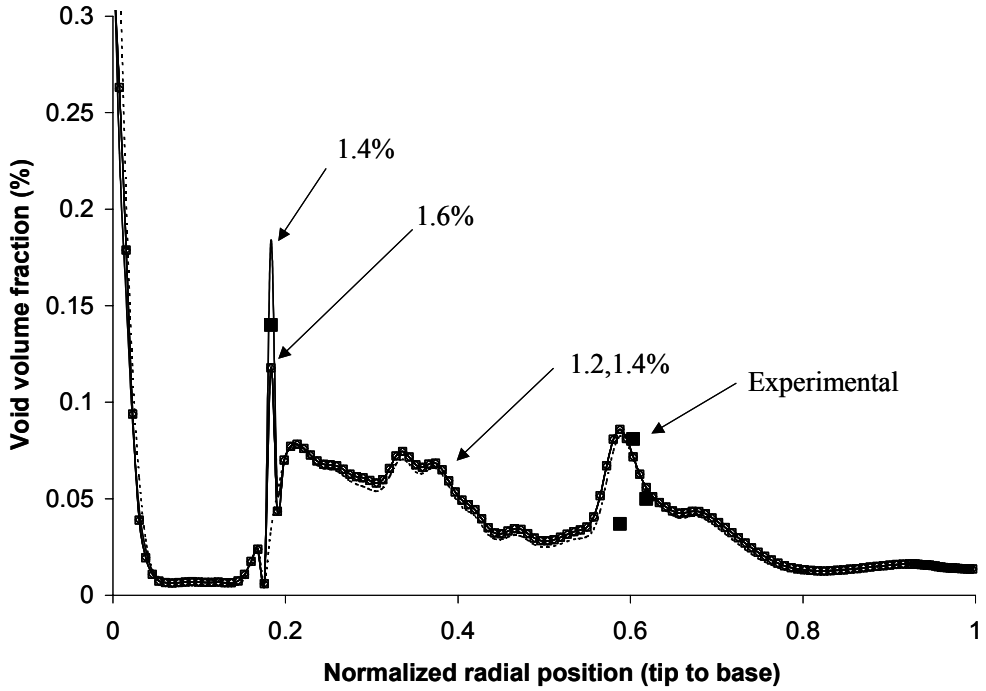

Figure 104: Effect on predicted void volume fraction of changing void volume fraction required for coalescence. Experimental data included for comparison.

The model successfully predicted the general location of the neck and fracture in the free-formed cones with the calibrated parameters (see Figure 84). The parameters found were kept constant for all subsequent models.

5.4 Tool/Sheet Interaction Effects

Numerical simulation of the conical die EM forming process revealed that the sheet undergoes a complex forming process that involves stretching, bending, impact and straightening. Figure 105 presents a detailed view of the interaction for an area close to the tip. The tool/sheet interaction can be divided into regions A, B and C, corresponding to the periods prior to, during and after the impact with the die. Prior to impact (region A), the sheet undergoes near biaxial stretching as the material fills the die. The impact with the die forces the sheet to undergo rapid and severe deformation. Just prior to impact (region B) the material bends, putting the outside of the sheet in tension and the inside in compression. The impact forces the material to straighten, producing the bulk of the deformation. After impact, in region C, the material undergoes secondary bending to its final position. The impact with the sheet produces the majority of the plastic deformation, as can be seen in Figure 105. Note that the figure depicts a time where the cone is almost fully formed, and yet the effective true plastic strains in region A are between 0-20% compared to 50-60% after impact. This is reflected in the damage evolution, as the most of the damage is generated at impact (Figure 106).

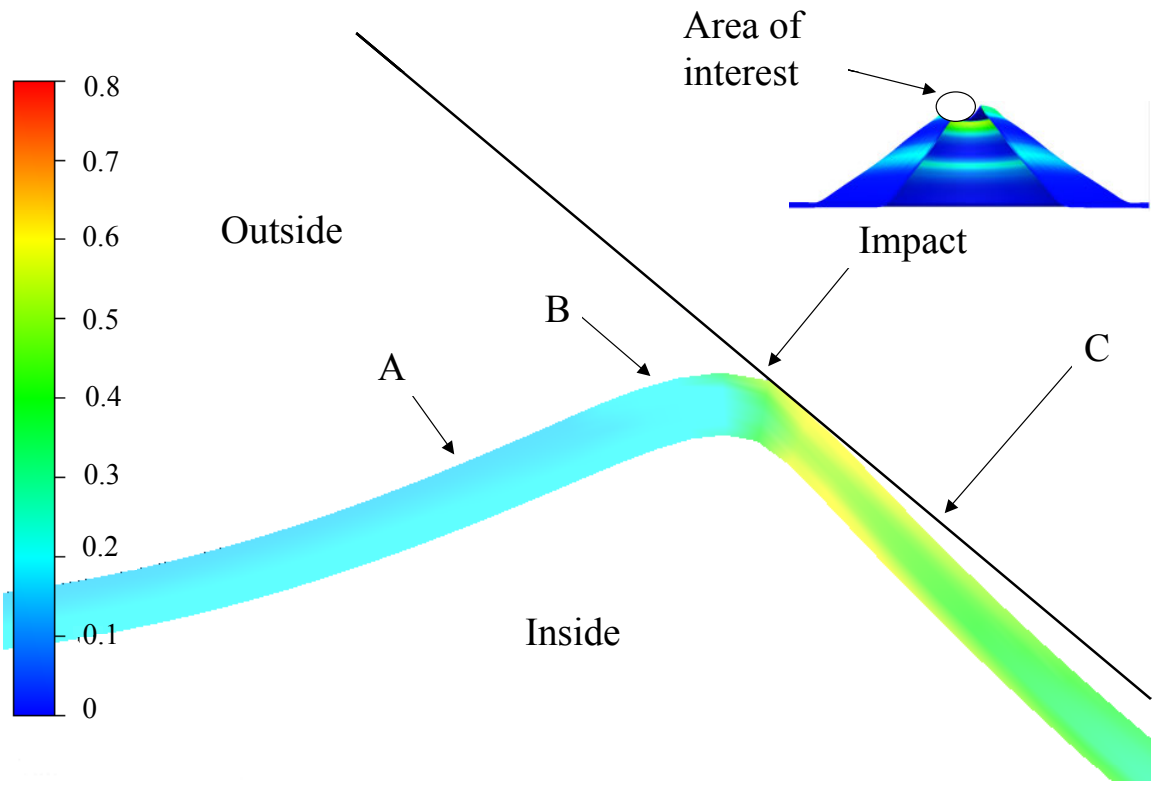

Figure 105: Effective plastic strain distribution as the sheet is formed into the die. Contours are effective plastic strain.

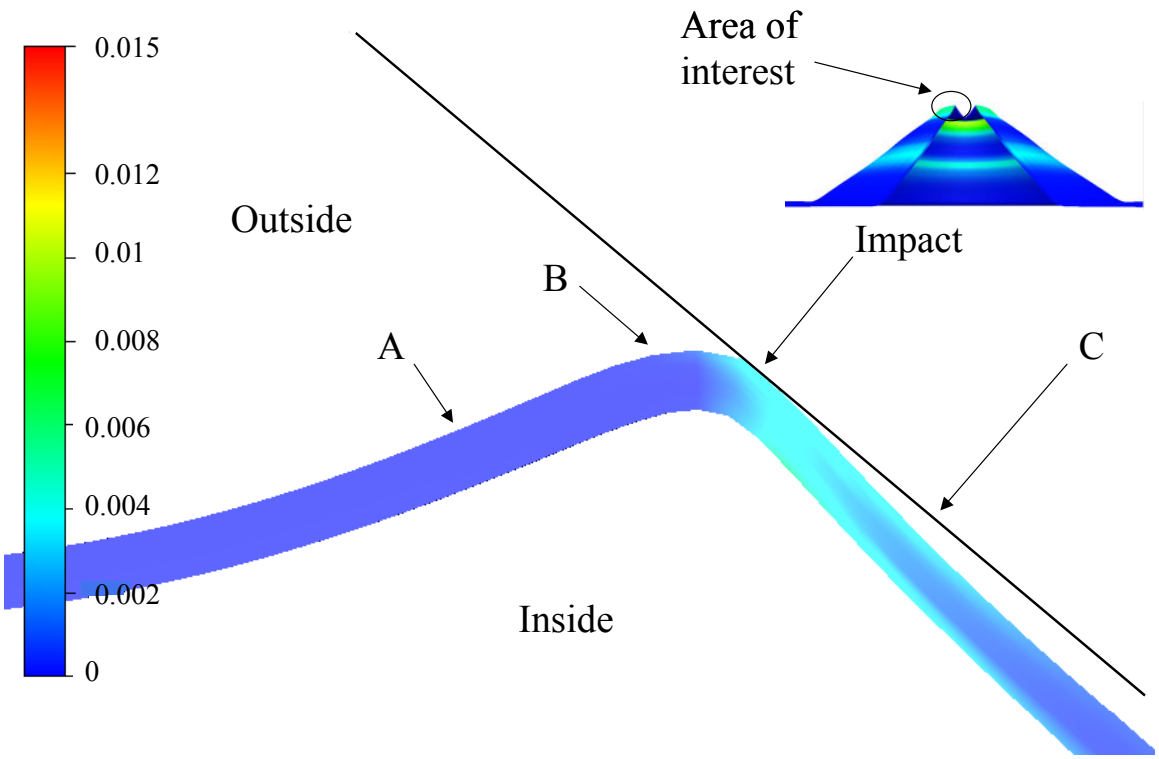

Figure 106: Detailed view of the tool/sheet interaction in the area of the tip of the sample**.** Contours are of void volume fraction (not adjusted for nucleated second phase fraction).

5.4.1 Stress and Strain Histories

Predicted stress and strain histories for the free-formed and conical samples are presented in Figure 107 through Figure 110. Data for localized and safe elements were chosen for detailed analysis for the free-formed samples; while for the cone samples, the elements in the areas of maximum predicted damage (step and area below tip) were chosen. The figures include the radial, hoop, through-thickness and shear stresses and strains for both the outside and inside element (see Figure 106). This was done since the inside and outside values show similar trends, but have significantly different magnitudes. The oscillatory nature of the stress results is due to the explicit dynamic nature of the code. No filtering was used to avoid loosing detail in the area of the impact.

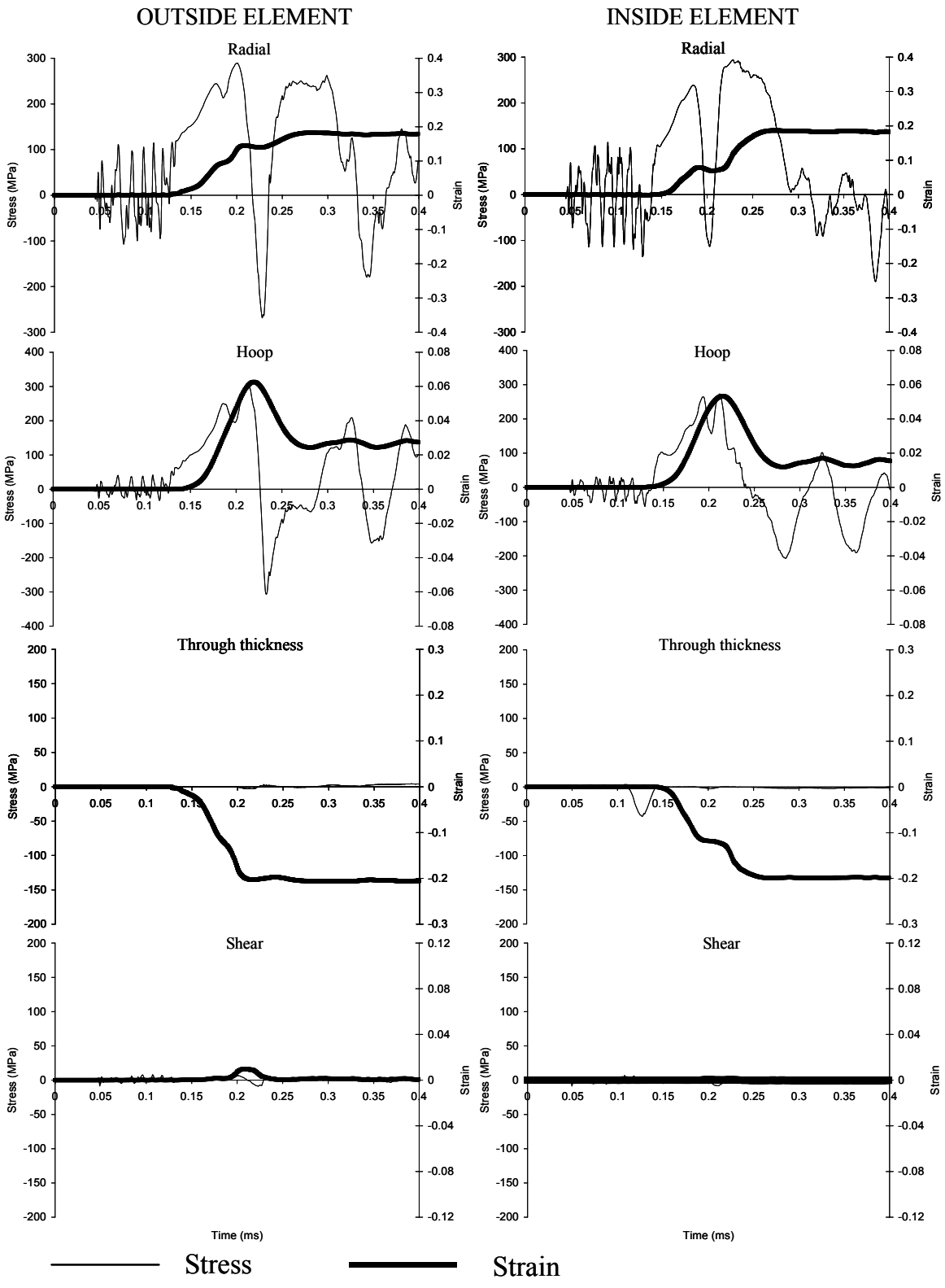

Figure 107: Typical stress and strain histories for a region below the neck of a free-formed sample. Note that final shape is reached at 0.31 ms.

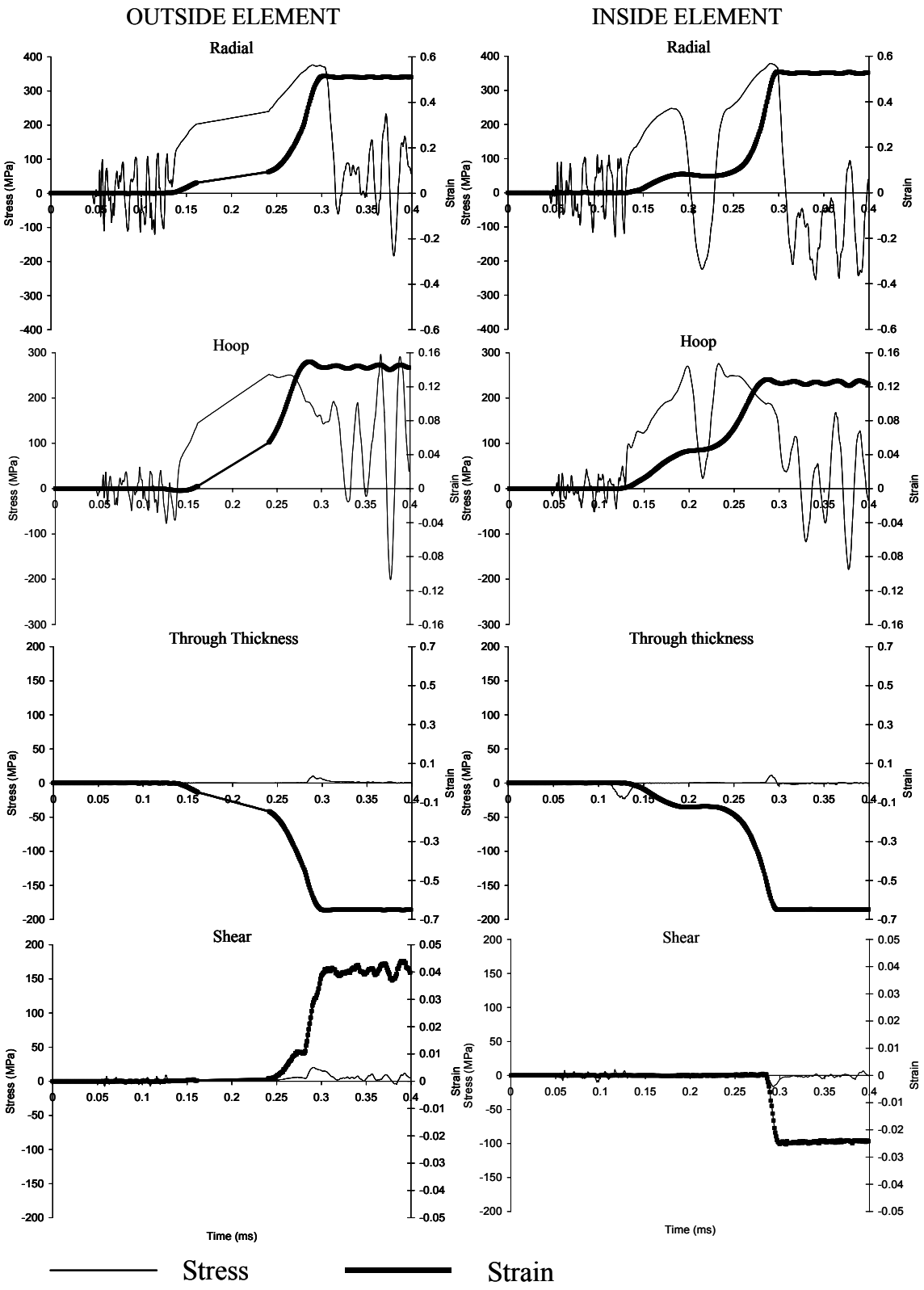

Figure 108: Stress and strain history for the necked region of a free-formed sample. Note that final shape is reached at 0.31 ms.

The free-formed samples undergo essentially plane stress conditions (i.e., no through-thickness or shear stresses) that are typical of conventional sheet forming processes. This response is reflected in the predicted stress and strains histories shown in Figure 107 and Figure 108. Figure 107 shows radial and hoop stresses and no through-thickness or shear stresses. The predicted strains are also typical of normal sheet forming, with radial, hoop and through-thickness strains and no shear strains. The change in sign in the radial and hoop stress at about 0.22 ms occurs as the material snaps through to its final position (see Figure 84). The stress-strain histories at the neck region shows similar trends, but with the expected higher strain values (see Figure 108). Small shear strains are predicted as the material localizes.

The strains rates for the free-formed process are much higher than those observed in conventional sheet forming. The strain rates for the safe area of the sample were 2,800 and 3,500 s^{-1} for the outside and inside elements. The highest strains were predicted for the localized elements, with maximum strains rates of 8,060 and 10,350 s^{-1} for the outside and inside elements. The material is subject to these strain rates for periods between 20 to 50 μs.

The predictions for the 40º cone sample is presented in Figure 109 and Figure 110. Figure 109 shows the data for the step area which impacts the die at 0.19 ms and Figure 110 shows the results for the area below the tip which impacts the die at 0.28 ms. The trends presented are valid for all of the cone except the area of the base, where the die bends the material, as well as the tip of the sample.

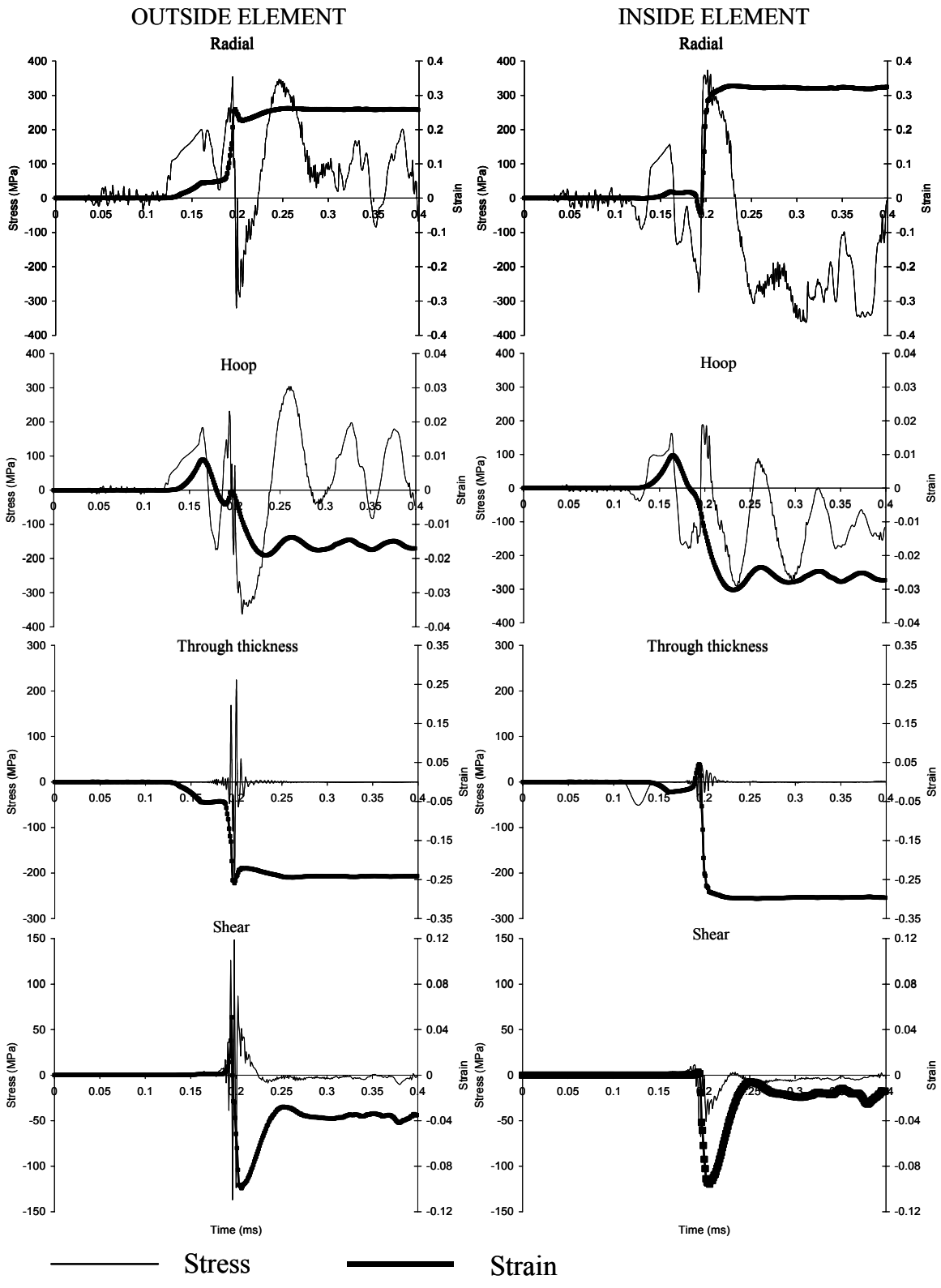

Figure 109: Stress and strain histories for the step area of a 40º conical sample. Time of impact is 0.19 ms. Scales vary for the stresses and strains but are constant for each type.

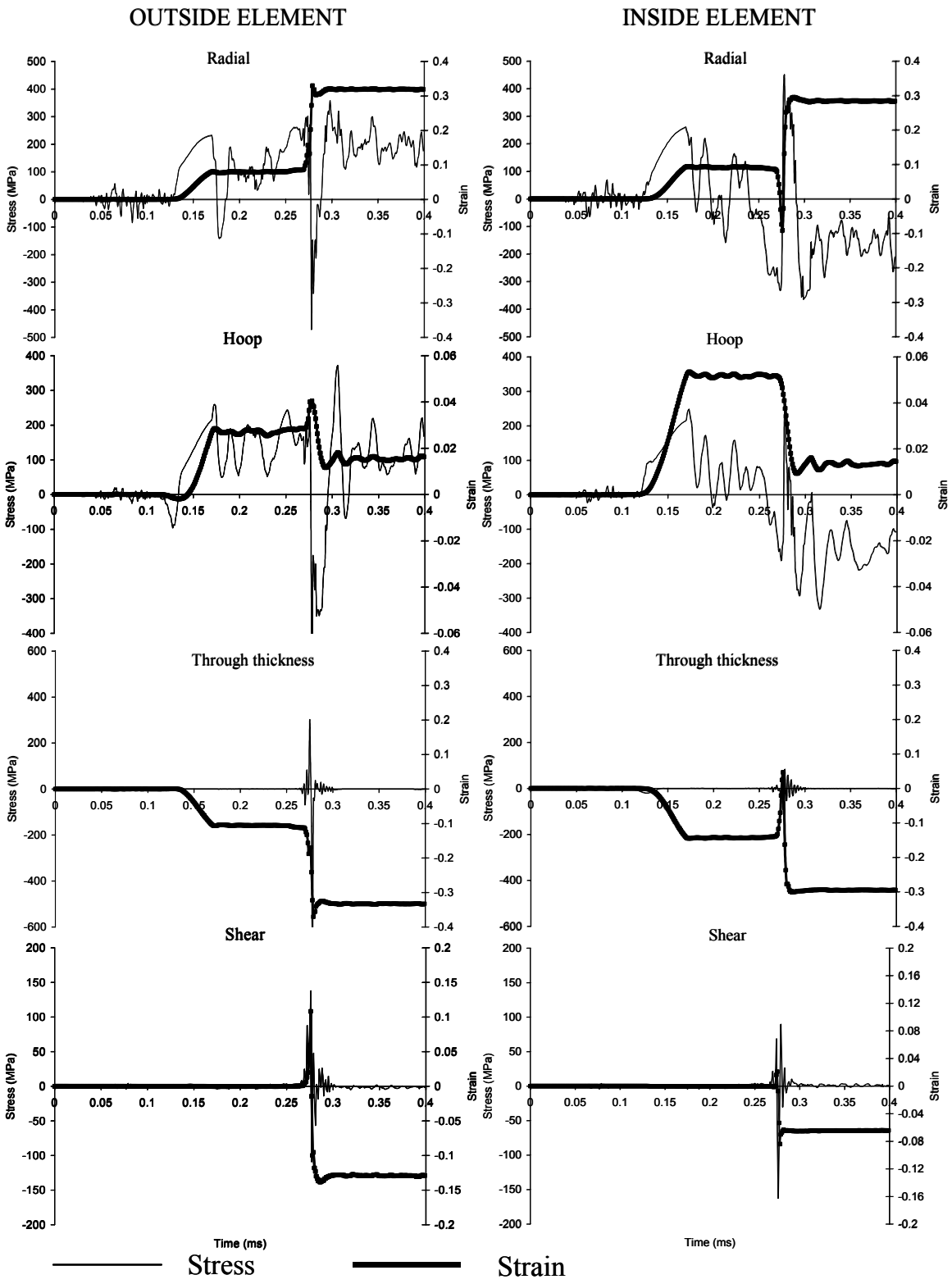

Figure 110: Stress and strain histories for an area below the tip of a 40º conical sample. Time of impact is 0.28 ms. Scales vary for the stresses and strains but are constant for each type.

The predicted radial stresses and strains are consistent with the sheet undergoing biaxial stretching and then bending and straightening at impact. For the inside elements, the stresses and strains become negative at impact, due to compression, and rapidly increase as straightening causes the inside to undergo tension. For the outside element, the strain increases due to the tension imposed by the bending and, as the sheets makes contact, the strains decrease slightly due to the straightening of the sheet. The straightening produces a negative radial stress peak, which is significantly larger in the area below the tip (see Figure 110).

The hoop stresses and strains increase before impact and then decrease. This is the result of the confining effect of the die. As the material reaches the tool, it has stretched biaxially, but is compressed in the hoop direction by the die. This leads to a reduction in the hoop strains and large negative stresses. For the step elements (Figure 109), the hoop stress increases and then decreases quite rapidly compared with the area below the tip (Figure 110) where the strains increase and stabilize before impact. This is the result of the step element impacting before the tip.

Through-thickness strains occur in both the pre-impact deformation and at the point of impact. As with the radial and hoop strains, at impact the through-thickness strains increase rapidly to the final values. Substantial through-thickness stresses are predicted to occur at the time of impact. These large through-thickness stresses are confined to the elements that make contact with the die, with the elements on the inside of the samples experiencing significantly lower stresses. This is consistent with the inertial ironing proposed by Balanethiram and Daehn [14,15]; however, the current predictions indicate that the through-thickness stresses are not uniform throughout the thickness due to the wave character of stress propagation during the impact [36]. The through-thickness stress peak that occurs between 0.10 and 0.15 ms is due to the applied forming pressure.

The tool/sheet interaction also results in through-thickness shear stresses and strains, primarily during the impact event. The shear strains likely contribute to the increased formability, introducing a deformation mode that is not typically encountered in sheet metal forming. However; the exact contribution of the shear stresses and strains to the increased

formability observed is the subject of ongoing research. The presence of large through-thickness and shear stresses makes this process significantly different than conventional sheet forming processes, which occur in near-plane stress conditions.

The majority of the plastic deformation occurs at impact. Since impact occurs in a period less than 10 μs, high rates of strain are generated. For example, considering Figure 109 and Figure 110, the radial strain rates for the step areas are 10,000 and 35,000 s^{-1} for the outside and inside elements, and for the tip elements, the strain rates are 30,000 and 69,400 s^{-1}. These strain rates are far in excess of those observed in conventional sheet metal forming and are an order of magnitude higher than the strain rates predicted for the safe regions of the free-formed samples.

5.4.2 Effect of Impact on Damage Evolution and Hydrostatic Stress

As was shown in the experimental section, relatively little damage is generated by the cone forming process, except at the step and in the region below the tip. Low levels of measured damage and modes of fracture other than ductile failure indicate that the suppression of damage is a factor in the increased formability that was observed. To analyze the effect of the tool/sheet interaction on the generation of damage, histories of void volume fraction and hydrostatic stress were assessed (a description of the relation between damage and hydrostatic stress is given in Section 1.6). The hydrostatic stress histories for free-formed elements can be seen in Figure 111 and Figure 112. Note that the hydrostatic stress is normalized by the yield strength of the material (97.7 MPa). For the free-formed sample, the inside and outside elements had comparable low levels of hydrostatic stress and virtually identical damage histories, consistent with conventional sheet forming operations. The dip in hydrostatic stress occurs when the area of the sheet inverts its shape, as the central region of the sheet snaps-through to take on the final dome profile, which results in compressive stresses. Damage in the free-formed samples only increases substantially in the localized region. Relatively little damage is generated in the safe areas. These trends are confirmed by the experimental measurements.

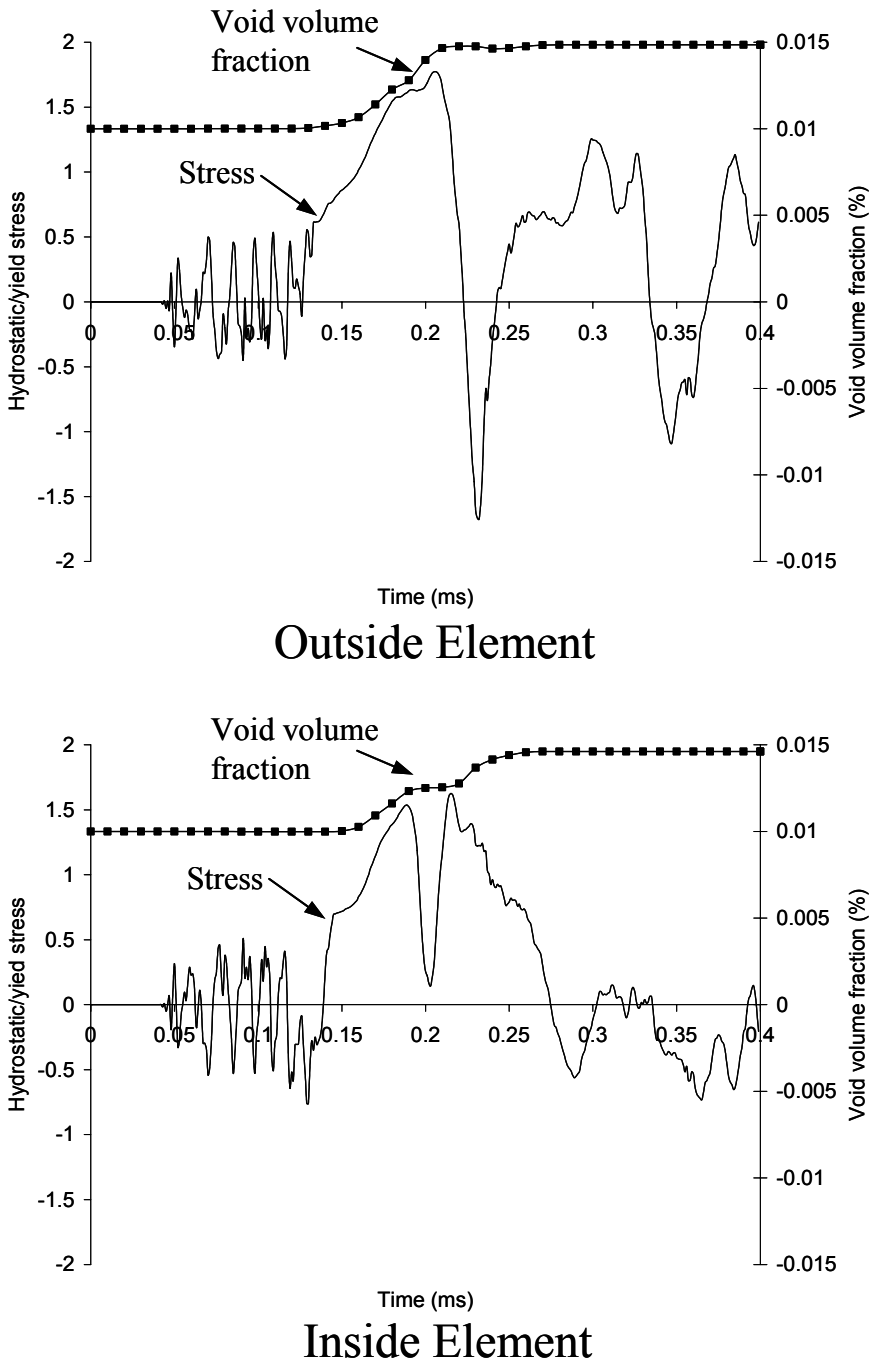

Figure 111: Normalized hydrostatic stress and void volume percentage histories for a region below the neck of a free-formed sample. Hydrostatic stress is normalized by the yield stress of 97.7 MPa.

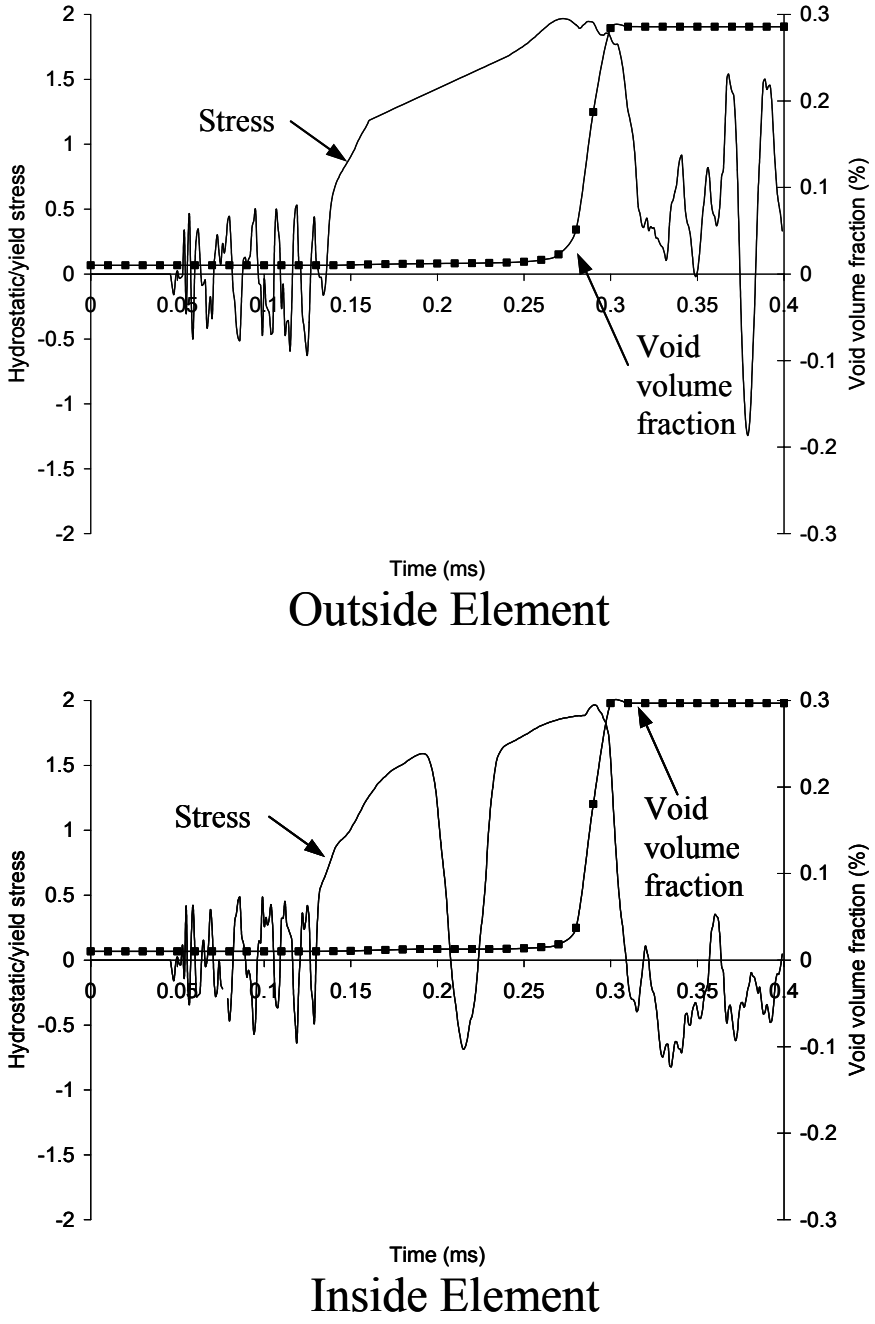

Figure 112: Normalized hydrostatic stress and void volume percentage histories for the neck of a free-formed sample. Hydrostatic stress is normalized by the yield stress of 97.7 MPa.

Figure 113 and Figure 114 show the data for the inside and outside of the step and tip area elements, respectively. Note that significantly less voids are predicted for the outside elements which leads to the void volume fraction scale being different than that for the inside element. In contrast to the free form cases, the hydrostatic stress and the void volume fractions are significantly different for the outside and inside elements. The predictions for the conical samples indicate that comparable positive hydrostatic stresses are produced when compared to the free-formed samples; however, in the conical samples the stresses oscillate and do not remain at large positive values for long after impact. The stresses for the free-formed sample are positive for longer, which is a more favourable condition for damage development.

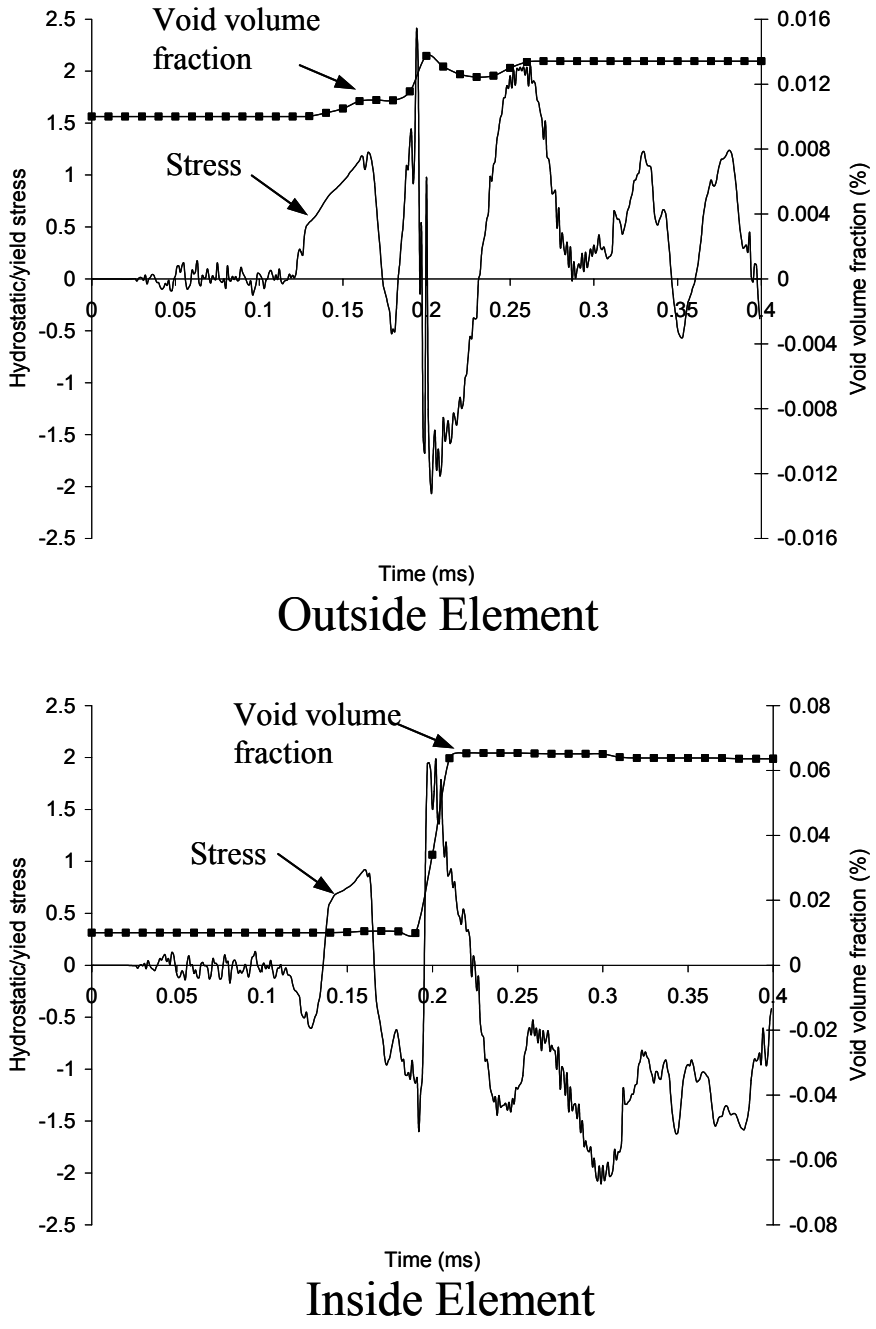

Figure 113: Normalized hydrostatic stress and void volume percentage histories for the step area. Hydrostatic stress is normalized by the yield stress of 97.7 MPa. Time of impact is 0.19 ms.

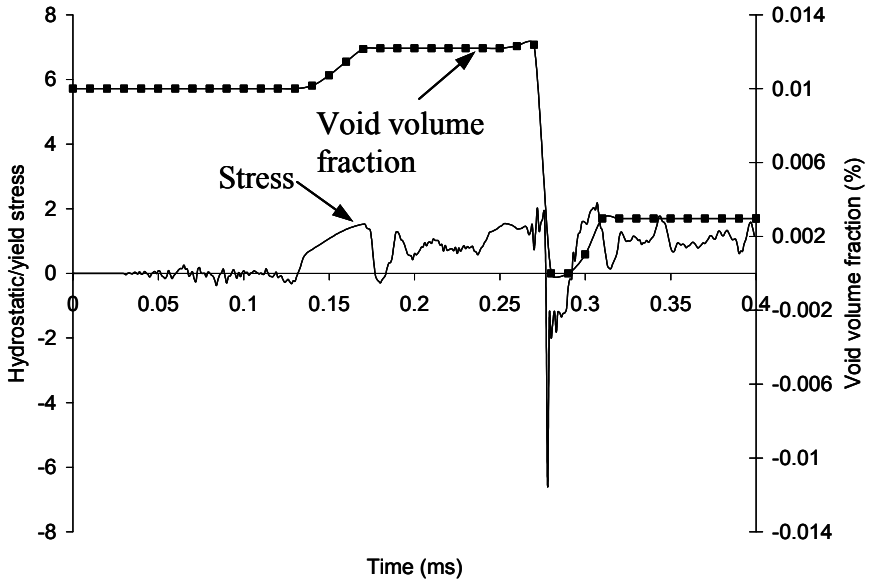

Outside element

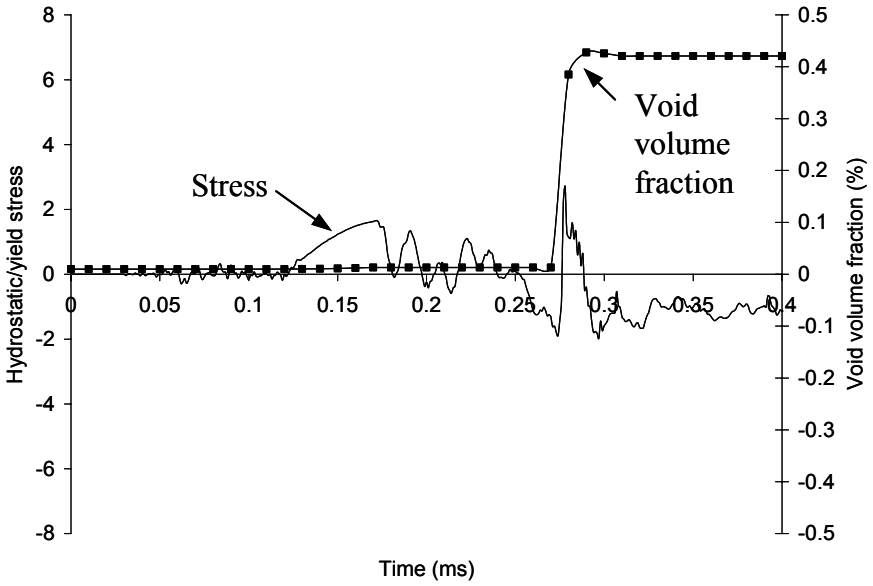

Inside element

Figure 114: Normalized hydrostatic stress and void volume percentage histories for the area below the tip. Hydrostatic stress is normalized by the yield stress of 97.7 MPa. Time of impact is 0.28 ms.

At impact, the hydrostatic stress increases rapidly followed by a sharp decrease. The outside element is subjected to a large negative hydrostatic stress at the time of impact, due to

the large through-thickness compressive stress that is generated. Negative stresses are generated for the inside element after impact as well, but are of significantly lower magnitudes. Thus on the surface of the sheet that is in contact with the die, impact creates a stress state favourable to damage suppression.

5.5 Strain Path Effects

Strain paths are very important when dealing with sheet formability [83,84,85]. The conventional FLD approach assumes that deformation occurs in a linear path in strain space. If the strain path varies during forming, the formability of the material will be affected [83]. For both the conical and free-formed samples, the predicted strain paths were non-linear, as can be seen in Figure 115 and Figure 116. The inside and outside elements in the safe areas of the free–formed samples followed two distinct strain paths, which are separated by the effects of the snap-through of the sample. In the necked region, the strain increased exponentially as the material localizes, as expected.

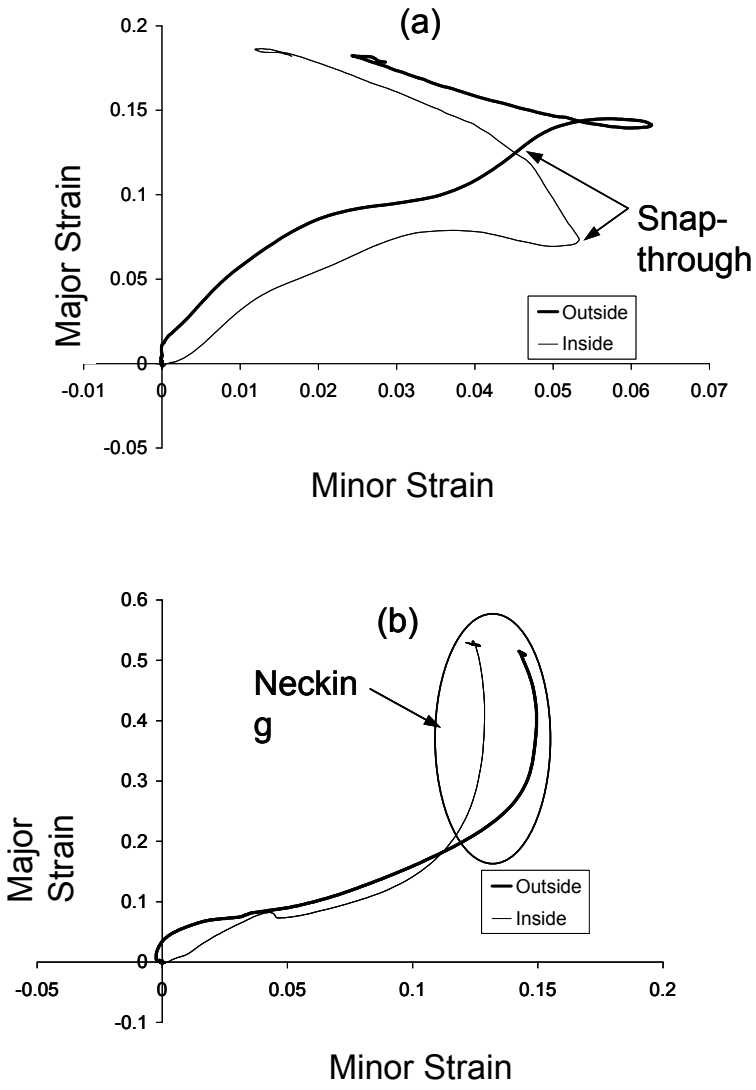

Figure 115: Strain path history for elements of a) the step and b) the tip area of a free-formed sample.

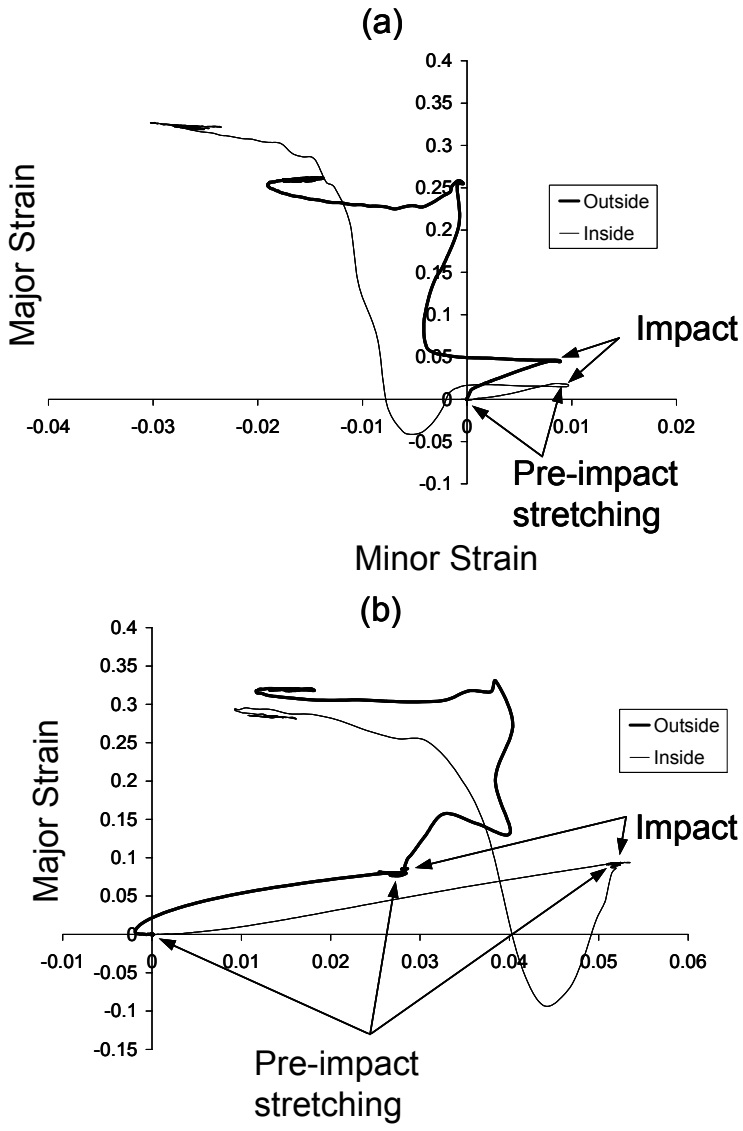

Figure 116: Strain path history for elements of the step and tip area of a 40º conical sample.

The conical samples followed a more complex strain path history (see Figure 116). The material was first subjected to some biaxial stretching before the strain path changes abruptly due to the impact. Some forms of pre-straining can improve formability; however, biaxial pre-strain has been shown to decrease formability in AA6111 [83], thus it cannot be considered a positive contributing factor in this process. No data was found for pre-straining effects on AA5754, but work on AA5052 showed that biaxial tensile deformation followed by uniaxial deformation increased formability in the area of plane strain [85]. Experimental work

is required to determine what effect, if any, the strain path has on the formability increase observed.

The non-linear nature of the strain paths makes direct comparisons with conventional FLD's difficult; however, no other widespread standard formability measure exists. Stress based FLD's [86] could be used in the future for comparison, but at present the data is not readily available.

5.6 Effect of Cone Angle on Damage Distribution

The predicted radial distributions of void volume fraction for the three cones studied are shown in Figure 117 and Figure 118 for the AA5754 and AA6111, respectively. As expected, the greater the angle, the greater the deformation of the sheet and thus more damage is evolved. The artificially large values at the tip of the cones are a numerical result caused by the poor element geometry in this region.

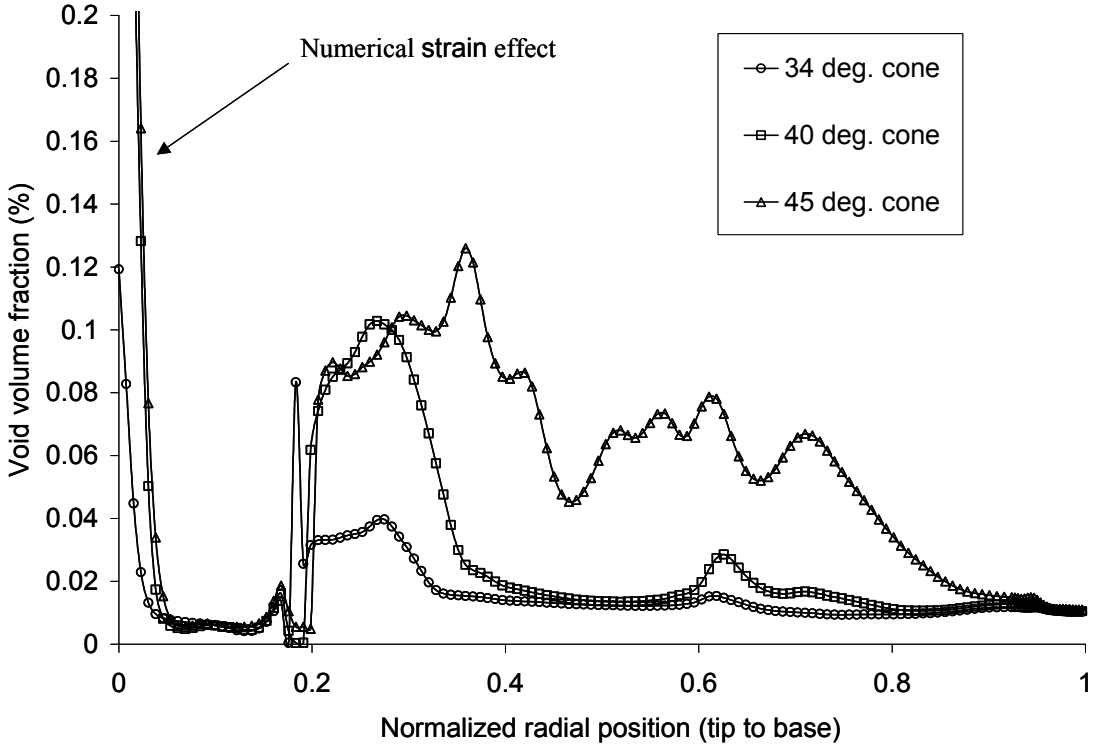

Figure 117: Effect of cone angle on damage distribution for AA5754.

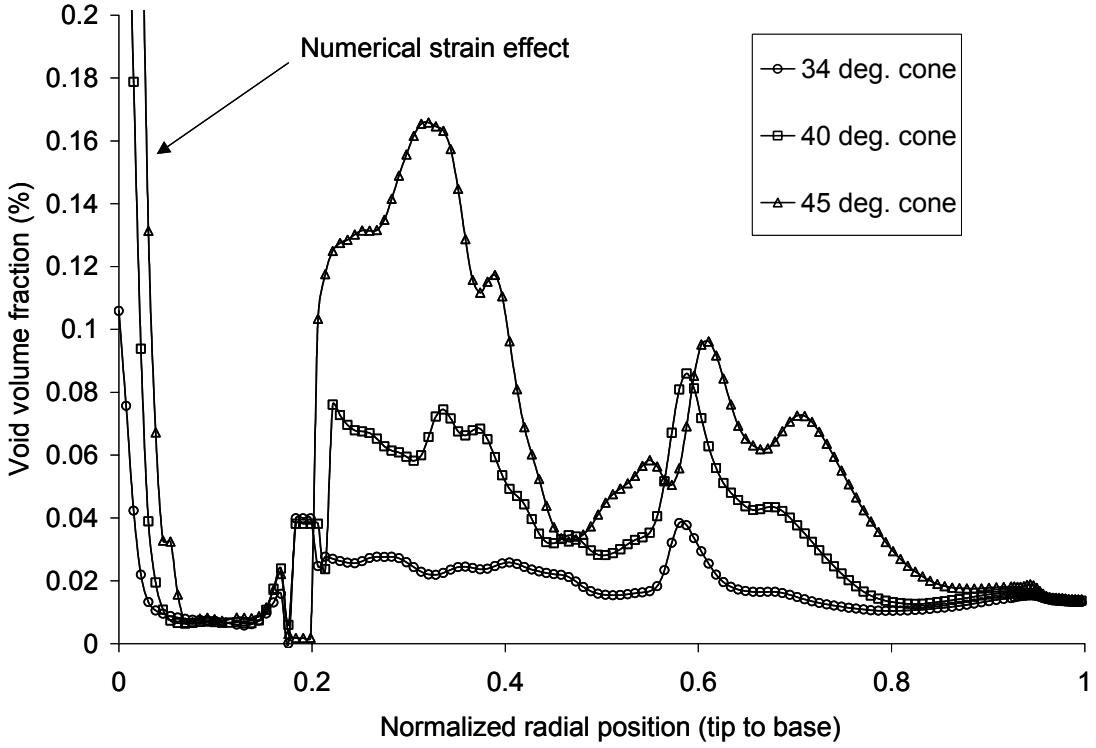

Figure 118: Effect of cone angle on damage distribution for AA6111.

5.7 Fracture and Buckling Predictions

The numerical models were able to accurately predict failure for the free-formed sample (see Figure 84); however, the failure of the 45º cones was not predicted accurately. Using the calibrated damage parameters, failure was not predicted for the 45º cones made of either material. A parametric study was carried out to determine if the model could predict failure. The numerical model was able to predict the tip fracture and some bottom element failure when a void nucleation strain of 10% was used; however, this is five times lower than the calibrated value. The failure predicted was not caused by localization as in the experimental samples; rather, the inside elements reached the critical void volume fraction after impact leading to their deletion from the simulation. In the case of the region below the tip, a chain reaction that started with the elimination of the bottom element that led to fracture. In the area of the tip a through-thickness fracture occurs, while in the area below the step, only

the inside elements failed Figure 119 shows the predicted failure pattern compared to an actual sample for a 45º sample.

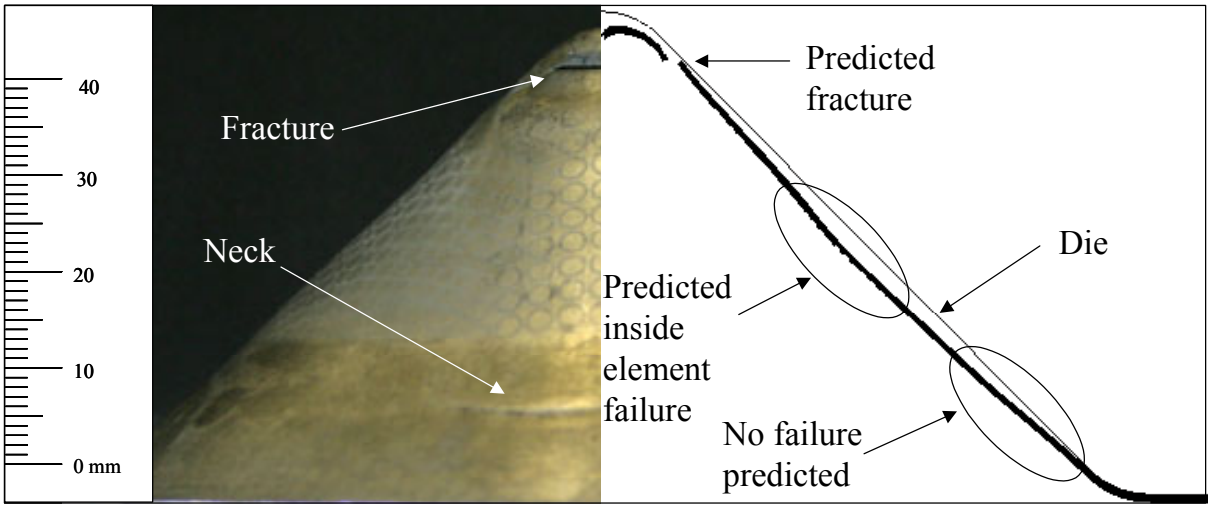

Figure 119: Failed AA5754 45º sample compared to numerical prediction. A nucleation strain of 10% was required to produce failure.

The inability to predict failure for the 45º cones is consistent with the observed fracture modes. The GTN material model used can predict ductile failure, which allows it to predict the failure of the free-formed samples with reasonable accuracy. The observations of the conical samples show that ductile failure is not the dominant failure mode for these samples, with plastic collapse, shear fracture and inter-granular failure observed. Thus it is reasonable that the GTN model did not predict failure since alternative failure criteria are required. However, the model does accurately predict damage trends, which makes it a valuable tool. Shear localization and failure could possibly be captured by increasing the mesh density and implementing kinematic hardening [87] for example, and will be the focus of future work. Capturing plastic collapse and inter-granular failure would require a model other than the GTN yield function.

Buckling was not predicted by any of the models. In the case of the AA5754 samples the lack of predicted buckling was due to the absence of the vacuum hole in the model geometry. The buckling present in the AA6111 samples is attributed to anisotropy effects due to the symmetrical nature or the buckling observed, although future work is required to

confirm this. An anisotropy model is not included in the material model used. Inclusion of the vacuum hole and anisotropy effects would likely result in buckling being captured by the model. Also, to capture typical buckling modes half symmetry or full geometry models are required, making the one-eight symmetry model used for this work unable to capture buckling.

CHAPTER 6

DISCUSSION

The experimental results clearly shown an increase in formability for both the AA5754 and AA6111 samples, when they were formed into the conical cavity dies using EMF. The free-formed samples did not exhibit any significant increase in formability, with the AA6111 showing limit strains below the conventional FLD. This difference in behaviour between free forming and in-die forming is a clear indication that the tool/sheet interaction is the main cause of the increase in formability. How exactly this interaction affects formability is not yet completely understood; however, but the present experimental and numerical work has provided valuable insight into the contributing factors.

Damage measurements from safe conical samples showed little or no damage increase, except for the tip and the step regions where significant increases were recorded. The largest damage increases occurred in the localized regions of failed samples, be it the neck in AA5754 or the shear zones in the AA6111 samples. The lack of generalized damage increases indicates that damage is suppressed by the tool/sheet interaction during in-die EM forming. This conclusion is supported by the fractographic analysis, which shows significant differences between quasi-static, free-formed and conical fracture surfaces.

The fracture surfaces of the samples formed into the 45º conical die show evidence of plastic collapse (AA5754 only), ductile failure and shear fracture, with the tip area of the AA6111 samples presenting evidence of inter-granular failure. In contrast, the fracture surfaces from quasi-static samples of both materials show evidence that ductile fracture is the dominant mode, with the AA5754 thinning significantly more than the AA 6111. The fracture surfaces of the free-formed AA5754 show some evidence of shear fracture, while there is virtually no difference between the free formed and quasi-static AA6111 fractures.

The conical samples show significant differences in fracture modes when compared to quasi-static and free-formed samples, with significant differences existing between the alloys. The AA5754 samples show evidence of plastic collapse and shear fracture, which was not observed in the quasi-static and free-formed cases. Ductile failure occurred only after significant thinning. Samples formed with AA6111 exhibited two distinct modes of fracture

with shear fracture dominating in the "saw tooth" fracture and inter-granular and shear fracture at the tip. Ductile fracture was not evident in either location. The shift from ductile fracture to plastic collapse, shear and inter-granular failure is a clear indication of damage suppression.

The evidence indicates that the tool/sheet interaction is the principal cause of the formability increase and that the interaction is acting to suppress damage. How this is happening is not clear from the experimental results. The numerical analysis presented provides insight into the forming process and how it affects the formability of the materials, despite the simplifying assumptions used. Predictions indicate that the tool/sheet interaction results in a complex deformation state where impact, bending and unbending play significant roles.

The models showed that two important consequences result from the tool/sheet interaction; it transforms the forming into a non-plane stress process with large through-thickness and shear stresses, and it confines the bulk of the plastic deformation to very short periods of time, leading to extremely high, localized strain rates. The stress state generated is characterized by high through-thickness stresses that occur at impact as the sample makes contact with the die. Significant shear stresses and strains are also generated at impact, which result in additional shear deformation that is not produced in conventional sheet forming.

One consequence of the generation of these stresses is a negative hydrostatic stress at the point of impact, whose magnitude varies depending on the location on the sample. This occurs at the point were the majority of the deformation and damage generation takes place and may be one of the causes of the damage suppression.

The models show that the majority of the plastic deformation in the conical samples occurs at the time of impact, with the rest occurring before as the material stretches to fill the die. At impact, the material bends and then unbends, while subjected to the impact stresses. This deformation takes place in approximately 10μs, which leads to strain rates in the 10,000-69,000 s^{-1} range. These rates are substantially higher than those observed in conventional sheet forming process and in the non-localized areas of the free-formed samples. The likelihood that these strain rates are affecting the formability of the material is very high. Unfortunately, to the authors' knowledge, no constitutive data is available for AA5754 sheet at these strain rates. Recent work on AA5754 at strain rates on the order of 1000 s^{-1} by Smerd *et al.* [22] has shown that the stress exhibits very low rate sensitivity, while the elongation

increases with strain rate. If these trends continue to hold for the strain rates predicted for the EMF process, this could be a significant contributing factor to the increased formability. Research into the high strain rate behaviour of AA5754 in the 10,000 s^{-1} range is required.

One clear conclusion that can be reached about EMF into a die, is that it is not a conventional sheet forming process. At impact, the material is subjected to a complex non-plane stress state that locally violates the plane stress assumption usually used in sheet metal forming analysis. This stress state is the main cause of the increased formability, as evidenced by the lack of significant increases in formability in free forming, which is essentially a plane stress process.

The analytical pressure distribution used in the numerical models provided good qualitative data despite the many assumptions used. Many of the discrepancies between the measured and predicted results are attributed to the use of the un-coupled modeling approach. The reduced accuracy was compensated by the savings in computational costs that allowed the study of the many different combinations of materials, tools and process parameters. Coupled EM simulations have the potential of significantly increasing accuracy and must be the subject of future work.

A limitation of the current implementation of the GTN model that must be addressed in the future is the inability to predict failure in the cone simulations. Implementing kinematic hardening in the material model and increasing mesh density should allow the model to capture shear fracture and thus improve the failure predictions. This would be computationally expensive but could potentially significantly improve the predictions.

Due to the through-thickness stresses present at impact, plane stress elements should not be used to model the EM forming process where the sheet interacts with a tool. Elements that can account for through-thickness stresses should be used. This will result in higher computational cost when compared to the models that use plane stress shell elements, which are the element of choice for metal forming application, and could lead to a lack of acceptance in industry.

The experimental and numerical investigations carried out provided very good insight into the EMF process, despite the many simplifying assumptions used. A similar approach could be employed in conjunction with fully coupled models to make the design of EM forming processes more efficient.

CHAPTER 7

CONCLUSIONS AND FUTURE WORK

7.1 Conclusions

The following conclusions were reached:

- The formability of AA5754 and AA6111 increases relative to conventional stamping processes in the step and burnished area of the samples when formed by EMF into conical cavity dies;
- No significant increase in formability was observed in the free-formed samples;
- Forming sheet into a die using EMF is not a conventional plane stress sheet forming process due to the complex stress state created by the tool/sheet interaction that includes significant radial, hoop, through-thickness and shear stresses;
- The analytical pressure distribution used to model the magnetic pressure provided good qualitative predictions of the deformation histories and the stresses and strains generated by the tool/sheet interaction;
- The complex stress state caused by the tool/sheet interaction is the dominant factor in the increased formability;
- Ductile fracture is not the dominant mode of failure for the conical samples; plastic collapse, ductile failure and shear fracture are all present in AA5754 and shear fracture and inter-granular failure are the dominant modes in AA 6111;
- Microvoid damage appears to be suppressed by the tool/sheet interaction that is produced when the sheet is formed into a die using EM forming;
- In cone forming, the majority of the deformation occurs at impact leading to strain rates well in excess of 10,000 s^{-1};
- Plane stress elements should not be used to model the EMF process. Solid elements that can capture through thickness and shear stresses should be used.

7.2 Future Work

This research has provided new insight on EMF, but a significant amount of work is still required to completely understand the process. Progress in process design is also required before EMF can enter widespread commercial use. It is recommended that the following work be done in the future:

- Investigations into EMF of sheet metal should be continued to gain further knowledge of how the tool/sheet interaction contributes to the increased formability;
- A coupled numerical model with non-rigid tooling should be developed to improve the accuracy of the EMF predictions;
- The predicted speed and deformation history produced by the tool/sheet interaction should be experimentally confirmed;
- Failure and buckling criteria that are able to predict the observed failure and buckling modes should be incorporated into the model;
- The mechanical properties of the AA5754 and AA6111 alloys should be characterized at the strain rates encountered in EMF and the material properties should be incorporated in to the material constitutive models;
- The causes of the discrepancy between the experimental and numerical AA6111 results should be further investigated to determine whether aging of high strain rate effects were behind the discrepancies;
- Research should be expanded to study corner fill operations that better represent parts that are encountered in industry.

REFERENCES

1 Wilson, D.V., "Aluminium versus steel in the family car-The formability factor", *Journal of Mechanical. Working Technology*, v.16, 1988, pp. 257-277.

2 Miller, W.S., *et al,* "Recent development in aluminium alloys for the automotive industry", *Materials Science and Engineering A,* v.A280, 2000, pp. 37-49.

3 Mori, T.; Hino, M,; Iwaya, J. and Miyahara, M., "Press formability of aluminum alloy sheets for automobile parts", *KOBELCO Technology Review*, n.14, July 1992, 49-53.

4 Wagner, H.J. and Boulger, F.W. "High velocity metalworking processes based on the sudden release of electrical of electrical energy" memorandum prepared by the Battle Memorial Institute for the Defense Metals Information Center, 1960.

5 *High Velocity Forming of Metals- Revised Edition* edited by Bruno E.J. American Society of Tool and Manufacturing Engineers, Dearborn, MI 1968.

6 Oliveira, D.A. *Electromagnetic Forming of Aluminum Alloy Sheet: Experiment and Model*. Masters of Applied Science thesis, University of Waterloo, 2002.

7 Lal, G.K. *The Plastomagnetodynamics of Electromagnetic Metal Forming*. PhD thesis, University of Waterloo, 1969.

8 "Electromagnetic Forming", Edited by Plum, M.M. Part of Forming Processes for Sheet, Strip and Plate. ASM, Materials Park OH, 1995.

9 Al-Hassani, S.T.S.; Duncan, J.L. and Johnson, W. "On the parameters of the magnetic forming process" *Journal. of Mechanical. and Engineering Science*, v.16, n.1, 1974, pp 1-9.

10 Jablonski, J. and Winkler, R. " Analysis of the electromagnetic forming process", *International Journal of Mechanical Sciences*, v. 20, 1978, pp. 315-325.

11 Al-Hassani "The plastic buckling of thin-walled tubes subject to magnetomotive forces" *Journal. of Mechanical and Engineering Science*, v.16, n.2, 1974, pp 59-70.

12 Al-Hassani, S.T.S. " Magnetic Pressure Distributions in Sheet Metal Forming". Electrical Methods of Machining, Forming and Coating. Institute of Electrical Engineers Conference Publication No. 1975, pp. 1-10.

13 Yudaev, V.B. "Manufacture of large sheet-metal parts by incremental electromagnetic forming" *kuznechno-Shtampovochnoe Proizvodstvo*, n. 7, 1989, pp. 1-2.

14 Balanethiram, V.S and Daehn, G.S. "Hyperplasticity: Increased forming limits at high workpiece velocity" *Scripta Metal.lurgica at Materialia*, v. 30, 1994, pp. 515-520.

15 Balanethiram, V.S. Hyperplasticity: Enhanced Formability of Sheet Metals at High Workpiece Velocities. Ph.D. Thesis, Ohio State University, 1996.

16 Golovashchenko, S.F.; Mamutov, V.S.; Dmitriev, V.V. and Sherman, A.M., "Formability of sheet metal with pulsed electromagnetic and electrohydraulic technologies", Proceedings of the *al.uminum 2003, Proceedings of the TMS annual meeting*, edited by S.K. Das, San Diego, Ca., TMS, 2003, pp. 99-110.

17 Tobe, T.; Kata, M. and Obara, H. " Metal forming by underwater wire explosion 1. An analysis of plastic deformation of circular membranes under impulsive loading" *Bulletin of the JSME* , v. 22, n. 164, February 1979, pp. 271-278.

18 Vohnout, V.J. and Daehn, G.S., "Effect of quasi-static prestrain and eddy currents on limit strains in electromagnetic pulse forming of two aluminum alloys", Proceedings of the *al.uminum 2002, Proceedings of the TMS 2002 annual meeting*, edited by S.K. Das and M.H. Skillingberg, TMS, 2002, pp. 19-25.

19 Takatsu, N.; Kato, M.; Sato, K. and Tobe, T., "High-Speed Forming of Metal Sheets by Electromagnetic Force", *JSME International Journal-Series III*, v. 31, n.1, 1988, pp. 142-148.

20 Personal comunictaion with D. Lloyd, ALCAN Internatinal, Kingston, ON, Canada, 2004.

21 Dieter, G., "Mechanical Metallurgy", 2nd edition, Mcgraw-Hill, Toronto, 1976, pp. 350-353.

22 Smerd, R.; Winkler, S; Salisbury, C; Worswick, M.; Lloyd, D; and Finn, M., "High Strain Rate Tensile Testing Of Automotive Aluminum Alloy Sheet", submitted for publication to the *International Journal of Impact Engineering*, November 2004.

23 Lindholm, U.S., Bessey, R.L and Smith, G.V., "Effect of strain rate on yield strength, tensile strength, and elongation of three aluminum alloys", *Journal of Materials*, JMLAS, v.6, n.1, 1971, pp. 119-133.

24 Gray III, G.T., "Classic split-Hopkinson pressure bar testing", ASM Handbook V. 8: Mechanical Testing and Evaluation, edited by H. Kuhn and D. Medlin, ASM Internationa, Materials Park, OH, 2000, pp. 462-476.

25 Tanaka, K and Nojima, T "Strain rate tests of aluminium alloys under high strain rate" The 19th Japan congress of Materials Research-Metallic Materials, March 1976, pp. 48-52.

26 Mukai, T; Masataka, K; and Kenji, H., "Strain-rate dependence of mechanical properties in AA 5056 Al-Mg alloy processed by equal-channel-angular-extrusion", *Materials Science and Engineering: A*, v.247, 1998, pp 270-274.

27 Higashi, K. *et al.*, "Strain rate dependence on mechanical properties in some commercial aluminum alloys", *Journal de Physique IV, Colloque C3, supplement au Journal de Physique III,* v. 1, oct. 1991, pp. 341-346.

28 Oosterkamp, L.; Ivankovic, A. and Venizelos, G., "High strain rate properties of selected aluminium alloys", *Materials Science and Engineering: A*, v.278, 2000, pp 225-235.

29 Rajendran, A.M. and Fyfe, I.M. "Inertia effects on the ductile failure of thin rings" *Transactions of the ASME - Journal of Applied Mechanics*, v. 49, 1982, pp. 31-36

30 Fressengeas, C. and Molinari, A. "Inertia and thermal effects on the localization of plastic flow", *Acta Metallurgica,* v. 33, n.3, 1985, pp. 387-396.

31 Regazzoni, G, Johnson, J.N. and Follansbee, P.S. "Theoretical Study of the Dynamic Tensile Test" *Transactions of the ASME - Journal of Applied Mechanics*, v. 53, 1986, pp. 519-528

32 Hu, X.; Wagoner, H.; Daehn, G.S. and Gosh, S., "The effect of inertia on tensile ductility" *Metallurgical and Material Transactions A,* v. 25A, December 1994, pp. 2723-2735.

33 Balanethiram, V.S *et al.*. "Hyperplasticity: Enhanced formability at high rates" *Journal of Materials Processing Technology*, v. 45, 1994, pp. 595-600.

34 Hu, X. and Daehn, G.S. "Effect of velocity on Flow localization in tension", *Acta Materialia,* v. 44, n. 3, 1996, pp. 1021-1033.

35 Altynova, M; Hu, X and Daehn, G.S., "Increased ductility in high velocity electromagnetic ring expansion", *Metallurgical and Materials Transactions A*, v. 27A, July 1996, pp 1837-1844.

36 Golovashchenko, S., "Numerical and experimental results on pulsed tube calibration," Proceedings of the *TMS annual meeting: Sheet metal forming technology-1999*, M. Demeri ed., San Diego, Ca., TMS, 1999, pp. 117-127.

37 Fenton, G.K. and Daehn, G.S., "Modeling of electromagnetically formed sheet metal", *Journal of Materials Processing Technology*, v.75, 1998, pp. 6-16.

38 Skripnichenko, A I; Yaskovich, A.G. and Meleshenko, B.A,. "Strength of metals under exposure to a pulsed magnetic field" *Vestsi akademii navuk Belaruskai ssr. Serya fizika-tekhnichnykh navuk.* 1956-1991, n.4 1985, pp. 12-16. Translated by O.Oorlov.

39 Ashby, M.F.; Embury, J.D.; Coksley, S.H. and Teirlinck, D., "Fracture maps with pressure as a variable", *Scripta Metallurgica*, v.19, 1985, pp. 385-390.

40 Dieter, G.E., *Mechanical Metallurgy,* SI metric edition adapted by David Bacon, MaGraw-Hill Book Company, London, 1988.

41 Goods, S.H. and Brown, L.M., "The nucleation of cavities by plastic deformation", *Acta Metallurgica*, v.27, 1979, pp.1-15.

42 Thomson, R.D. and Hancock, J.W., "Ductile failure by void nucleation, growth and coalescence", *International Journal of Fracture*, v.26, 1984, 99-112.

43 Bridgman, P.F., *Studies in Large Plastic Flow and Fracture*, McGraw Hill, Toronto, 1952.

44 Worswick, M.J.; Pilkey, A.; Lloyd D. and Court, S., "Damage Characterization and Damage Percolation Modelling in Aluminum Alloy Sheet", *SAE Technical Paper Series*, Paper 2000-01-0773, 2000.

45 Lewandowski, J.J. and Lowhaphandu, P., "Effects of hydrostatic pressure on mechanical behaviour and deformation processing of materials", *International Materials Reviews*, v.43, n.4, 1998, pp.145-187.

46 Spitzig, W.A., "Effect of hydrostatic pressure on deformation, damage evolution, and fracture of iron with various initial porosities", *Acta Metallurgica et Materialia*, v.38, n.8, 1990, pp. 1445-1453.

47 Zok, F. and Embury, J.D., "Forming of low-ductility materials under hydrostatic pressure", *Journal of Material. Shaping Technology*, v.8, 1990, pp. 77-81.

48 Brownrigg, A.; Spitzig, W.A.; Richmond, O.; Teirlinck, D. and Embury, J.D., "The influence of hydrostatic pressure on the flow stress and ductility of a spherodized 1045 steel", *Acta Metal.lurgica*, v.31, n.8, 1983, pp.1141-1150.

49 French, I.E. and Weinrich, P.F., "The effects of hydrostatic pressure on the mechanism of tensile fracture of aluminum", *Metallurgical Transactions A*, v.6A, 1975, pp. 1165-1169.

50 Belyy, I.V.; S.M. Fertik and Khimenko, L.T., "Electromagnetic Metal Forming Handbook". Translation by Altynova, M.M. Available from the Hyperplastic Forming Consortium at the Ohio State University. Original published in 1977, translated in 1996

51 Magneform, San Diego, CA, USA, www.magneform.com.

52 Zhang, H.; Murata, M. and Suzuki, H. "Effects of various working conditions on tube bulging by electromagnetic forming". *Journal of Materials Processing Technology*, v. 48, 1995, pp 113-121.

53 Lee, S.H. and Lee, D.N., "A finite element analysis of electromagnetic forming for tube expansion", *Journal of Engineering Materials Technology*, v.116, 1994, pp. 250-254.

54 Mahanian, S. and Blackwell, D., ”Finite element analysis of electromagnetic forming of tubes with fittings”, *Manufacturing Science and Engineering*, MED-V. 4, 1996, pp. 323-329.

55 Shangyu, H.; Zhihua, C.; Zhongren, W.; Lifeng, W. and Mei, Y., “A finite-element analysis of electromagnetic sheet metal-expansion process” (sic), *Transactions of the Nonferrous Metals Society of China*, v.8, n.3, 1998, pp. 490-495.

56 Oliveira, D.A.; Worswick, M.J. and Finn, M., “Finite Element Modeling of the Electromagnetic Forming of Aluminum Alloy Sheet,” Proceedings of The 4th International ESAFORM Conference on Material Forming V. II, Liege, Belgium, 2001, pp. 773-776.

57 Oliveira, D.A. and Worswick, M.J., “Electromagnetic forming of aluminum alloy sheet”, *Journal de Physique IV France*, v.110, 293-298 (2003).

58 Risch, D.; Beerwald, C.; Brosius, A. and Kleiner, M., “On the significance of the die design for electromagnetic sheet metal forming” Proceedings of the *1st International Conference on High Speed Forming*, Lerhstuhl fur Umformtechnik, University of Dortmund, M. Kleiner ed., March 31-April 2004, Dortmund, Germany, pp. 191-200.

59 Oliveira, D.A. and Worswick, M.J., “Electromagnetic forming of aluminum alloy sheet”, *Journal. de Physique IV France*, v.110, EDP Sciences, Les Ulis, DOI: 10.1051/jp4:20030709, 293-298 (2003).

60 Oliveira, D.A.; Worswick, M.J. and Finn, M., “Finite Element Modeling of the Electromagnetic Forming of Aluminum Alloy Sheet,” Proceedings of The 4th International ESAFORM Conference on Material Forming V. II, Liege, Belgium, 2001, pp. 773-776.

61 El-Azab, A.; Garnich, M. and Kapoor, A., “Modeling of the electromagnetic forming of sheet metals: state-of-the-art and future needs”, *Journal of Materials Processing Technology*, v.142, 2003, pp. 744-754.

62 Bendjima, B. and Féliachi, M.; "Finite element analysis of transient phenomena in electromagnetic forming system", Proceedings of the *IEE 3rd International Conference on Computation in Electromagnetics*, 10-12 April 1996, Bath, UK, pp.113-116.

63 Bendjima, B.; Srairi, K. and Féliachi, M., "A coupling model for analysing dynamical behaviours of an electromagnetic forming system", IEEE Transactions on Magnetics, v. 33, n. 2, March 1997, pp.1638-1641.

64 Bessonov, N. and Golovashschnenko, S., "Numerical simulation f pulsed electromagnetic stamping processes", Proceedings of the *1st International Conference on High Speed Forming*, Lerhstuhl fur Umformtechnik, University of Dortmund, M. Kleiner ed., March 31-April 2004, Dortmund, Germany, pp. 83-91.

65 Stiemer, M.; Svendsen, B.; Unger, J.; Suttmeier, F.T. and Blum, H., "Development of multi field software solutions and their applications for the optimization of electromagnetic high speed forming processes" Proceedings of the *International Conference on High Speed Forming*, Lerhstuhl fur Umformtechnik, University of Dortmund, M. Kleiner ed., March 31-April 2004, Dortmund, Germany, pp. 93-104.

66 Stiemer, M.; Klocke, M.; Suttmeier, F.T.; Blum, H.; Joswig, A. and Kulig, S., "Validation of different approaches to coupled electrodynamic-structural mechanical simulation of electromagnetic forming", Proceedings of the *1st International Conference on High Speed Forming*, Lerhstuhl fur Umformtechnik, University of Dortmund, M. Kleiner ed., March 31-April 2004, Dortmund, Germany, pp. 105-118.

67 www.matweb.com.

68 The Lectroetch company, www.lectroetch.com.

69 IAP Research Inc. product information, Dayton, OH, USA, www.iap.com.

70 Roper Scientific Incorporated, www.roperscientific.com.

71 MediCybernetics, Newburyport, MA, USA, www.mediacy.com.

72 JEOL USA, Peabody, MA, USA, www.jeol.com.

73 Oxford Instruments, www.oxinst.com.

74 J. Hallquist, *LS-DYNA Theoretical Manual*, Livermore Software Technology Corporation, 1998.

75 Gurson, A.L., "Continuum Theory of Ductile Rupture by Void Nucleation and Growth: Part 1 – Yield Criteria and Flow Rules for Porous Ductile Media," *Journal of Engineering Materials Technology*, v. 99, 1977, pp. 2-15

76 Tvergaard, V., "Influence of Voids on Shear Band Instabilities Under Plane Strain Conditions," *International Journal of Fracture*, v.37, n.4, 1981, pp. 389-407.

77 Tvergaard, V. and Needleman, A., "Analysis of the Cup-one Fracture in a Round Tensile Bar", *Acta. Metallurgica*, v. 32**,** 1984, pp. 157.

78 Worswick, M.J. and Pick, R.J., "Void growth and coalescence during high velocity impact", *Mechanics of Materials*, v. 19, pp. 293-309, 1995.

79 Worswick, M.J. and Pelletier, P.," Numerical simulation of ductile fracture during high strain rate deformation", *Euorpean Physical Journal, Applied Physics*, v. 4, 1998, pp. 257-267.

80 Personal communication with Dr. S. Winkler, Assistant Research Professor, Mechanical Engineering Department, University of Waterloo, Waterloo,ON, Canada, 2004.

81 *Forming Limit Diagrams: concepts, methods and applications*, edited by Waganoer, R.; Chan, K. and Keeler, S., TMS Publications, Warrendale PA, 1989.

82 Takeshima, M.; Sugamata, M. and Kaneko, J., "Stretch formability and forming limits of age-hardened aluminum alloy sheet", Abridged English version of article published in the *Journal of the Japan Institute of Light Metals*, v. 33, n. 10, 1984, pp. 610-617.

83 Graf, A. and Hosford, W., "The Influence of strain-path changes on forming limit diagrams of AA6111 T4", *International Journal of Mechanical Sciences*, v. 36, n. 10, 1994, pp. 897-910.

84 Sang, H. and Lloyd, D.J., "The influence of biaxial prestrain on the tensile properties of three aluminum alloys", *Metallurgical Transactions A*, v. 10A, 1979, pp. 1771-1776.

85 Kohara, S., “Forming-limit curves of aluminum and aluminum alloy sheets and effects of strain path on the curves”, *Journal of Materials Processing Technology*, v.38, 1993, pp. 723-735.

86 Stoughton, T., “Stress-based forming limits in sheet-metal forming”, *Journal of Engineering Materials and Technology*, v.123, 2001, pp. 417-422.

87 Lievers, W.B.; Pilkey, A.K. and Worswick, M.J., “The co-operative role of voids and shear bands in strain localization during bending”, *Mechanics of Materials*, v. 35, 2003, pp. 661-674.